UNIVERSITÀ DI TRENTO
Department of Industrial Engineering

XXXIV cycle

Doctoral School in Materials, Mechatronics and System Engineering

Particulate Matter Emission Issues in Brake Systems

Ana Paula Gomes Nogueira

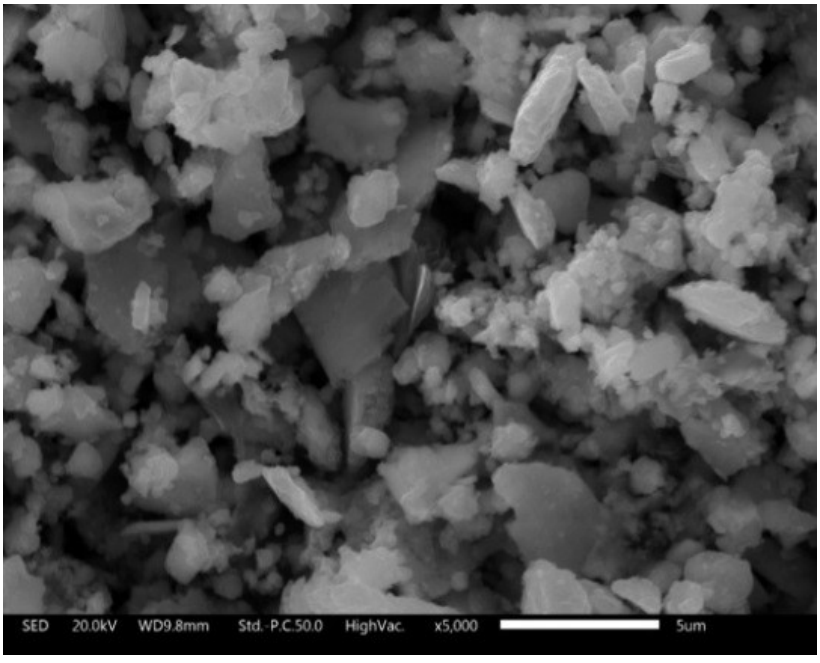

July 1st, 2022

Particulate Matter Emission Issues in Brake Systems

Ana Paula Gomes Nogueira

Email: ana.gomesnogueira@unitn.it

Approved by:

Prof. Stefano Gialanella, Supervisor
Dept. of Industrial Engg.
University of Trento, Italy

Prof. Giovanni Straffelini, co-supervisor
Dept. of Industrial Engg.
University of Trento, Italy

Ph.D. Commission:

Prof. Cinzia Menapace
University of Trento, Italy

Prof. Roberta Vecchi
University of Milan

Prof. Vlastimil Matějka
Technical University of Ostrava

University of Trento

Department of Industrial Engineering

July 1st, 2022

University of Trento - Department of
Industrial Engineering

Doctoral Thesis

Ana Paula Gomes Nogueira – 2022

Published in Trento (Italy) – by University of Trento

To Maria & Antonio

and João

OSS!

Abstract

Automotive brake systems are source of particulate matter (PM) emissions, particularly in the urban areas. Several human ill-health are related with this kind of pollution. Along tire wear, road wear and dust from resuspension, the brake wear comprises the most relevant non-exhaust source of road traffic related emissions.

Aiming at studying the PM brake emissions, this thesis is composed of an introductory part containing the main concepts and the state of art of the main subjects; and the experimental part, which comprehends three investigations.

Chapters 2, 3, 4 and 5 are dedicated to the introduction part. Chapter 2 provides a brief description of the friction and wear, as well as the fundamental principles of braking by contact. Chapter 3 discuss the disc braking system, with particular attention to the pad friction materials. Chapter 4 is dedicated to friction layer: the layer usually developing at the disc/pad interface, affecting the performances of the tribological system. Finally, Chapter 5 provides an extensive discussion of the issues related to the particulate matter originated from disc brake systems.

The experimental part is presented in the Chapters 6, 7, 8 and 9. Chapter 6 describes the methodology applied in all the investigations. Chapter 7 investigates the PM emissions behavior and its interaction with the friction and wear, aiming to identify the mechanism of generation the PM emissions. A copper-containing and a copper-free commercial friction materials were used, with particular emphasis on the effect of the *scorching treatment*. The Chapter 8 is dedicated at investigating the tribological behavior and the corresponding PM emissions in two Cu-free commercial friction materials, aiming to a better understanding the effect of abrasive ingredients on the emissions generation. Finally, the Chapter 9 investigated the addition of natural ingredient rice husk in a new eco-friendly Cu-free brake friction material composition, focusing the attention on the tribological and emissions behavior. All tests were carried out using a pin-on-disc tribometer equipped with an enclosure, especially designed for investigating the tribological properties, as well as the airborne particles generated by contact. Low-metallic friction materials, both commercial and laboratory-produced, were tested against cast iron discs. The tests parameters used correspond to mild sliding conditions resembling those faced in real braking. Such conditions are characteristic of driving in urban areas, where the expose to traffic PM is concentrated.

A specific methodology of analysis was developed, based on SEM/EDXS techniques. Using this methodology, comparative investigations between the elemental composition of the virgin friction materials, the worn surfaces of the friction materials and the airborne particles collected during the tribological tests were carried out. The results point out the triboxidative wear as the main mechanism of the PM brake emissions generation. Moreover, particles produced by abrasive wear can be also directly emitted to the environment.

Contents

List of Figures

List of Tables

Chapter 1
Introduction

Particulate matter (PM) is composed of liquids and solids particles dispersed in the air, many of them harmful for the human health and for the environment. The three main sources of these kind of emissions are: industry, domestic activities and road traffic. Towards traffic pollution, the attention has been mostly paid to the emissions from the engine combustion process. However, these emissions are just a fraction of the total amount released into the atmosphere. In fact, traffic related emissions comprise exhaust and non-exhaust emissions, indicating respectively: emissions originated from the combustion of fossil fuels and emissions from other traffic and vehicle sources, such as tires and brakes. The relative amount of non-exhaust emissions from each source can significantly change accordingly to different real-world driving conditions and vehicle types. However, it is estimated that between 15-55% of the total mass emitted from non-exhaust sources came from the brakes of the vehicles.

Exposure to PM emissions is associated with several adverse health side-effects and premature mortality. In recent years, health concerns related to the PM released from brakes have attracted a significant attention, mostly due to their relatively small size and the presence of toxic elements. As smaller as the PM are, deeper they can penetrate on the human body. Moreover, its inflammatory capacity increases with the content of toxic elements. The health risks associated with these kinds of particles involve increasing tendency of lung cancer, respiratory systems inflammations and oxidative stress, with possible damage of the DNA.

Since aplenty of regulations have been imposed to reduce the exhaust emissions over the last decades, PM from non-exhaust sources are comparatively becoming more prominent than the exhaust. Nowadays, the discussion concerning new regulations of PM from brakes systems is growing up and the demand for systems producing low polluting emissions and keeping high performance is required. However, this topic starts to be extensively studied on last few years only; the current knowledge on the PM brake emissions under realistic driving conditions is very limited. Furthermore, most of studies concentrate

its attention in measure the amount of emitted particles and a lack of comprehension on the mechanisms involving on the emissions particles formation and still remains.

This thesis aims at understanding the generation of coarse and fine PM brake emissions, i.e., particles from 10 to 1 μm. The studies were concentrated in pairs of low-metallic pad friction materials and cast iron discs. Most of the tested friction materials are result of the European projects LOWBRASYS and EcoPads; projects dedicated to reducing the PM brake emissions and eliminate the copper of the pad materials, respectively. The tests parameters applied correspond to mild sliding conditions resembling those faced in real braking. Such conditions are characteristic of driving in urban areas, where the expose to traffic PM is concentrated. Particular efforts were made in developing a methodology of analysis capable to identify the mechanisms involved in the PM brake generation.

Chapter 2

General concepts

This chapter provides a brief description of the main concepts supporting this thesis. Friction and wear are discussed: forces involved, the real contact area and wear mechanisms. The fundamental principles of braking by mechanical friction are also stated.

2.1 Friction

When two bodies are in contact and pressed against each other by a normal force (F_N), a tangential force (F_T) is necessary to initiate a relative motion between them. In opposite direction of the motion is generated a friction force (F_f), caused by interactions between the mating surfaces. Those are the main forces involved in a sliding contact, as shown in Figure 2.1.

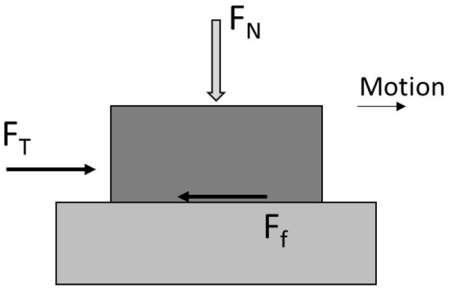

Figure 2.1: Representation of the forces involved in a sliding contact.

The magnitude of the tangential force (F_T) is directly proportional to the applied normal force (F_N) through the friction coefficient (μ), as given in Equation 2.1. Thus, the friction coefficient is the ration of frictional force between two bodies and the force pressing them together. The values of friction coefficient range from near 0 to greater than 1.

$$F_T = \mu F_N \tag{2.1}$$

When two bodies are in contact without movement, the tangential force is no greater than the friction force acting in opposite direction. In this case, the relation between normal

and tangential forces is described by the static friction coefficient (μ_s). However, as soon as the relative motion starts, a lower tangential force is necessary to keep the two bodies in reciprocal movement. In this case, the dynamic friction coefficient (μ_d) plays its role [1-3]. The scheme of the Figure 2.2 shows both situations.

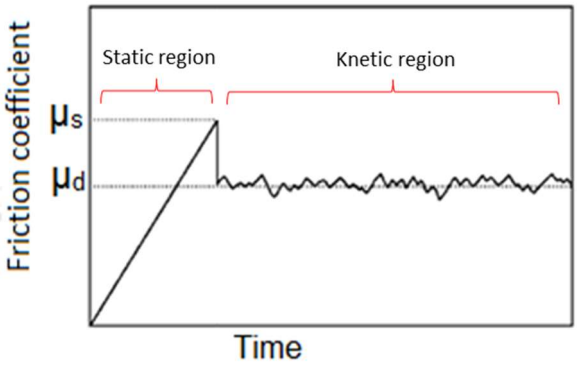

Figure 2.2: Schematic of a typical friction coefficient showing static (μ_s) and dynamic (μ_d) friction coefficients.

In general, the nominal contact area does not affect the friction coefficient; however, as the real contact area increases, the friction coefficient may also increase. In fact, the real contact between two surfaces occurs only at discrete joints. Figure 2.3 shows a schematic example of the real contact area between two mating surfaces. The protrusions and depressions on both rough surfaces determine the points in which the real contact is actually happening.

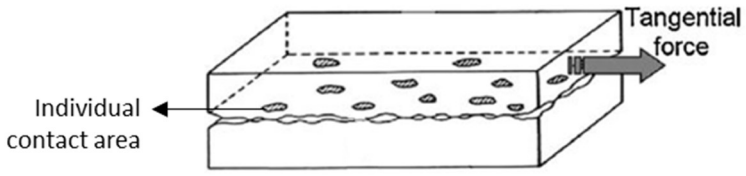

Figure 2.3: Schematic example of the real contact area between two matting surfaces (adapted from ref.[6]).

Depending on the magnitude of the forces and the characteristics of the materials involved, the joints are elastically or inelastically deformed, resulting in several individual contact areas. The sum of the individual contact areas defines the real contact area [1-6].

Friction is a rather complex phenomenon and beyond the real contact area, several aspects can also affect the friction coefficient. Adhesion is one of the most dominant and occurring as a result of the chemical interactions between the mating surfaces. Bonds across the interface are generated in each individual contact area. Weak bonds, for example Van der Waals and hydrogen bonds, easily form between in contact surfaces. High affinity of the materials can lead to stronger bonds, such as covalent or metallic. The magnitude of these interactions is calculated by the work of adhesion, corresponding to the energy necessary to separate two adjacent surfaces. As the chemical affinity of the materials increases, the magnitude of the adhesive forces also increases. Table 2.1 displays values of the work of adhesion for different materials in contact. A clear effect from the chemical affinity between the materials is noticed. In case of sliding contact, bonds are continuously broken and reformed at discrete points of the real contact area [1, 6].

Table 2.1: Values of work of adhesion for different materials in contact [1].

Materials in contact	**Work of adhesion (J/m^2)**
Fe-Fe	3.00
Cu-Cu	2.20
Fe-Cu	0.83
Fe-Ag	0.29
Fe-Pb	0.23
Fe-polymer	<0.2

The friction coefficient, particularly the dynamic one, can also be affected by abrasive interactions, occurring when materials with different hardness are in relative motion and the harder material scratches the softer. In general, abrasion determines an increase in the friction coefficient. At the same time, abrasive interactions can generate loss of material, i.e., wear. This matter will be better discussed on the next section.

Other phenomena occurring when materials with different hardness are in sliding contact is the material transfer. In this case, part of the softer material, mostly plastically

deformed, stick on the harder material creating a layer on the adjacent surface. Transfer material phenomena usually lead to increasing of the friction coefficient.

2.2 Wear

The surfaces in sliding contact usually wear out, characterized by the loss of material. The action of the forces discussed in section 2.1, submits the two bodies to a compressive and shear stresses, often accompanied by an increment of the contact temperature. When the solicitations are greater than the forces which maintain the integrity of the surfaces, wear occurs. Abrasive particles usually induce wear as well. In fact, different wear mechanisms should be acting during the sliding. Typically, one mechanism will be predominant in a tribological system, and its characteristics guide the wear behavior of the couples. Four wear mechanisms, highly present on sliding contact systems, are identified as follows [1, 7-10]:

• **adhesive wear**: related to the adhesive interactions discussed in section 2.1, it occurs when the adhesion forces in the contact areas are stronger than the cohesive bonds of one the materials, causing the breakage of the weaker material.

• **abrasive wear:** occurs by the ploughing action of hard particles in a soft material, typical situation when the difference in the hardness between the bodies exceeds 20-30 %. There are two types of abrasive wear due to: two-body interactions, when the abrasive particles are strongly bonded to the hardest body; and three-body interactions, when some hard particle is trapped in between the mating surfaces, forming an intermediate layer. In both cases, material is removed from the softer surface by the action of the hard particles.

• **wear by contact fatigue**: occurs by repeated loading and unloading cycles on the bodies, which may induce the formation of cracks on the mating surfaces. Cycle loading during friction, with non-conformal contacts and high local stress, is the typical situation involving the wear by contact fatigue.

• **tribo-oxidative wear**: occurs by the brakeage of the, mostly, oxide layers which may form onto the mating surfaces for the chemical reactions with the outer atmosphere. The formation of the oxide layer is favored by the increasing temperature in the contact areas and tribomechanical conditions at the contact areas.

Figure 2.4 shows a representation of the four wear mechanisms discussed above.

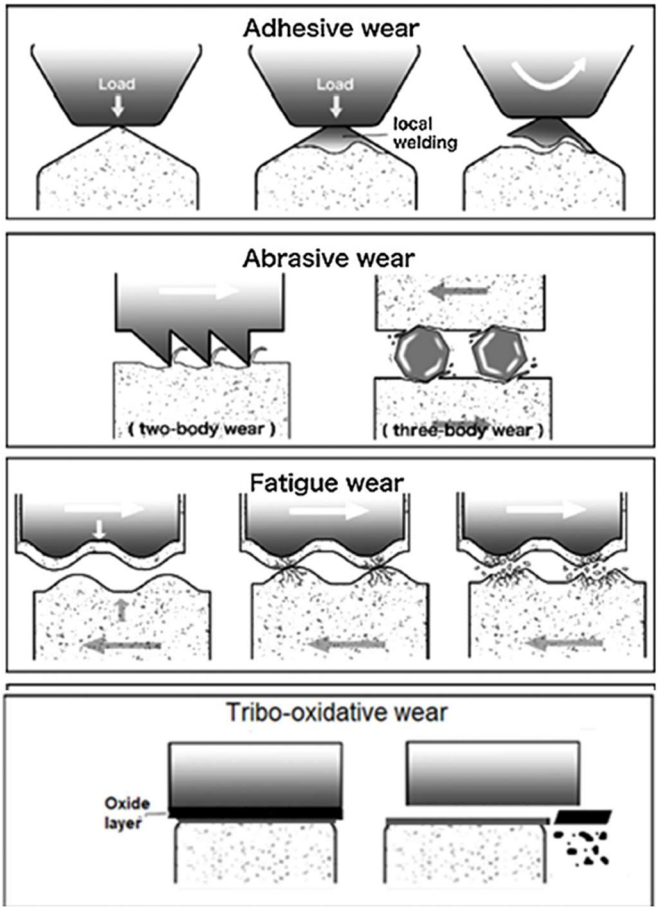

Figure 2.4: Wear mechanisms (adapted from ref.[10]).

2.3 Braking by contact

The law of conservation of energy states that: energy cannot be created or destroyed, just transformed. Therefore, to slow down a vehicle it is necessary to remove its kinetic energy. In case of braking by contact, the friction force between two surfaces enables the system to transform the kinetic into thermal energy.

The kinetic energy present in a vehicle in motion is given by the Equation 2.2.

$$E_{kinect} = \frac{mv^2}{2} \tag{2.2}$$

where m (in kg) is the mass of the vehicle and v (in m/s) is its linear velocity.

The variation of kinetic energy to reduce the velocity v_1 to v_2 is given by Equation 2.3:

$$\Delta E_{kinect} = \frac{m({v_1}^2 - v_2^2)}{2} \quad (2.3)$$

where v_1 and v_2 are the initial and final velocities, respectively.

In summary, to reduce motion the amount of energy to be transformed is dependent on the mass, and the difference of squared initial and final velocities of the vehicle.

In a braking by contact, the system must be able to dissipate all the generated heat.

Chapter 3

Disc Brake System

Nowadays, the disc brake system is the most widespread configuration on the automotive market. Its specific design provides a very efficient heat dissipation.

Since this thesis deals with the disc systems, this chapter is dedicated to discussing its specificities. Particular attention is given to the pad materials in their Cu-free formulations.

3.1 Overview

The first approach of disc braking system was presented by Frederick W. Lanchester in 1902. Afterwards, further developments and wide improvements were achieved, however its betterment continues being applied. In this kind of tribological system, friction occurs between two pads and a disc in a dry sliding condition.

Figure 3.1 shows the three main parts of the brake disc system: calliper, disc and pads. By a hydraulic system connected to the calliper, once the driver presses the brake pedal, the calliper moves and pushes the pads against the rotating disc. The friction force acts in opposite direction to the angular velocity of the disc and, thereby, heat is generated.

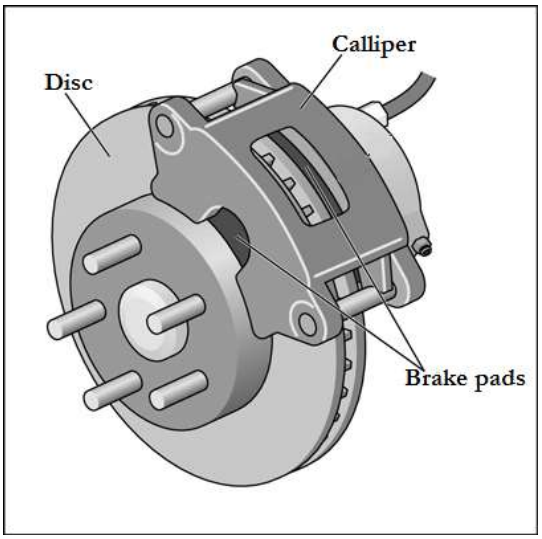

Figure 3.1: Simplified layout of a generic disc brake system.

The generated heat must be dissipated through exchange with the environment. Otherwise, the temperature in the real contact area may rise tremendously [1, 2, 5].

In summary, an automotive disc brake system must comply with the following performance requirements:

• **Relatively high friction coefficient**: a stable friction coefficient featuring values between 0.3 to 0.7 is required. The friction coefficient translates the brake efficiency of the braking system.

• **High heat dissipation capacity:** since the kinetic energy needs to be converted into thermal energy, the system must be capable to dissipate all the generated heat. It is estimated that around 90% of total heat is dissipated by the disc.

• **High compression strength:** the system must resist the pressure exerted by the pads during the braking. Braking pressure usually oscillates between 1 to 4 MPa, when switching from a normal braking to an emergency one.

• **High wear resistance:** since wear can damage the parts of the brake system, it must be as low as possible.

3.2 Wear on disc brake systems

In a dry sliding contact, wear is always present. However, a high wear of the braking system can result in a short lifespan of the components and must be minimized. Typically, the wear mechanisms involved in those systems are adhesive, abrasive and tribo-oxidative. The predominance of each wear mechanism depends on the characteristics of the mating surfaces and on the sliding conditions which the components are submitted to.

Regarding the sliding conditions, the wear of disc and pads occurs in both normal and heavy braking conditions, resulting in mild and severe wear, respectively. The effect of the combining pv braking parameters (contact pressure “p” and sliding velocity “v”) on wear is shown in Figure 3.2. High temperature, mostly resulted of a high speed, is described as the most important parameter in case of a severe wear.

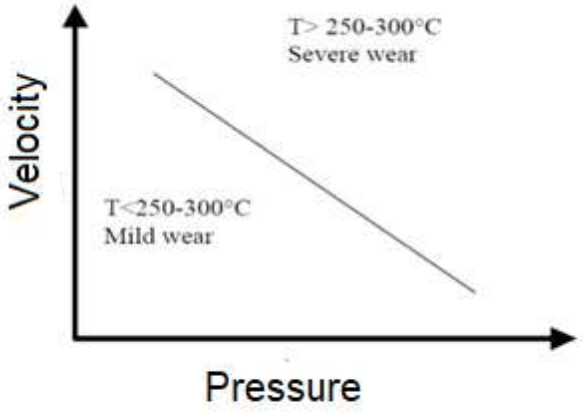

Figure 3.2: Schematization of the influence of braking parameters on the braking conditions. [11].

Before discussing how the temperature can affect wear, it is important to keep in mind the existence of an inward temperature gradient at the contacting surfaces. A schematic diagram of the temperature distribution in the contact region is given in Figure 3.3. The frictional heating is concentrated within the real contact area, featuring the contact temperature (Tc), also called flash temperature. In these regions, the temperature can rise enough to cause changes in the structure and properties of the sliding materials, such as oxidation of the surface and melting of the contact materials. The average temperature on the surface (T_{nom}) is lower than the contact temperature; however it may affect the materials in contact as well. Moving away from contact zone, the temperature decreases gradually until achieves the bulk temperature (T_b) [12, 13].

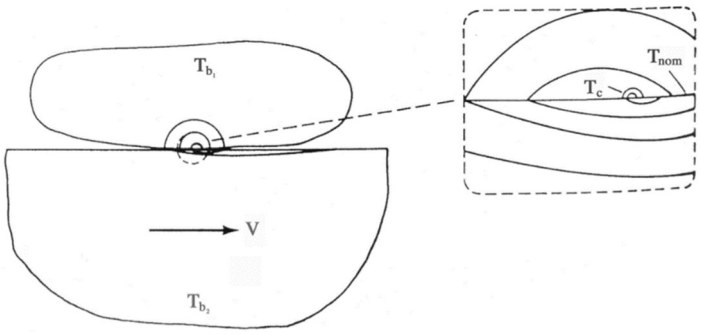

Figure 3.3: Schematic representation of the frictional heating and contact temperatures [12].

The temperature reached on the disc/pad interface depends on several factors, such as the system's geometry, the braking conditions and the composition of the brake materials. The disc, commonly made of grey cast iron, displays high thermal conductivity. The pads, instead, are made of composite mixtures of different constituents, such as ceramic particles, minerals, metallic particles and fibers, all bonded together by an organic binder. The pads usually feature low thermal conductivity. Nevertheless, owing to the presence of the organic matrix, the pads have an intrinsic tendency to thermal degradation. As a consequence, the relevant wear behavior may change from mild to severe when the temperature rises above the critical temperatures (above 250-350 ºC) [14, 15]. By the degradation of the organic constituents, the ceramic particles, iron fibers and all the inorganic constituents are more easily removed from the surface of the friction material during the sliding action, increasing the wear. The wear behavior of a friction material at different temperatures is given in Figure 3.4, showing an exponential increase of wear rate above the critical temperature.

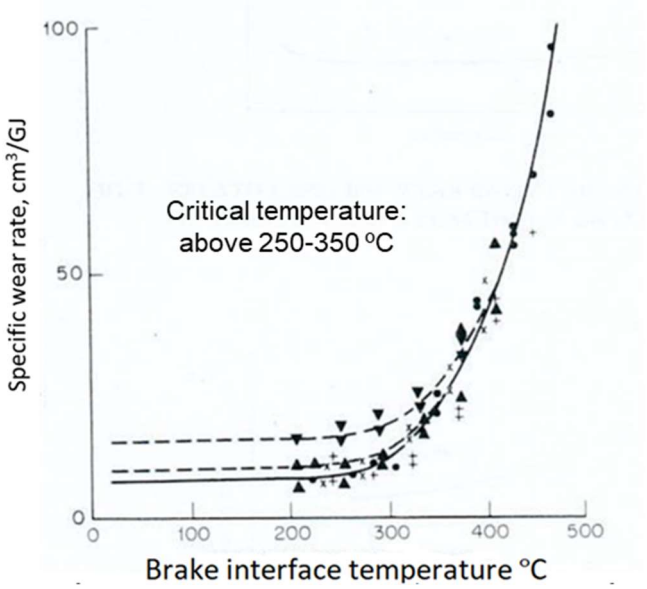

Figure 3.4: Specific wear rate of a friction material in different temperatures [15].

The wear behavior of both disc and friction material as a function of the temperature was further investigated by Verma et al. [16], through pin-on-disc (PoD) tests with a low-metallic friction material against a cast iron disc. They observed a transition from mild to severe wear of the friction material when the temperature increases above to 170 °C, with a major increase above 250°C approx., as shown in Figure 3.5. No significant changes in the disc's wear were noticed. The phenomenon was ascribed to the thermomechanical decomposition of the organic matrix present in the friction material.

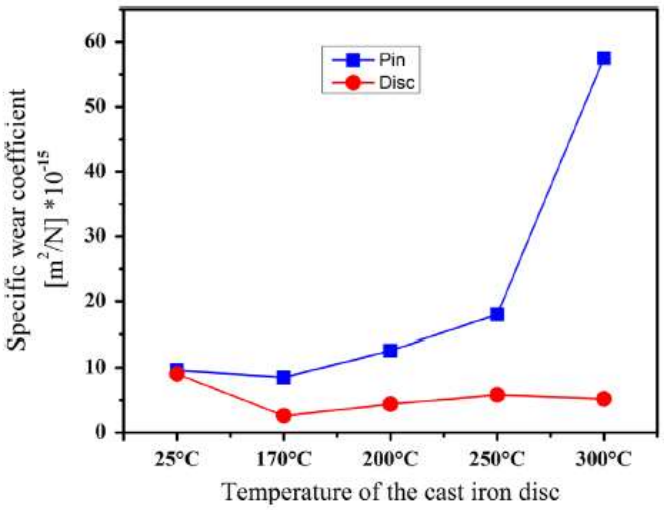

Figure 3.5: Specific wear coefficient of both friction material and disc in function of the temperature [16].

According to Barros et al. [17], transition in wear regimes can also take place at low temperatures, under the effect of changing contact pressure. The Figure 3.6 shows the wear values for two specimens of friction materials (B.1 and B.2), PoD tested under different pressures. A transition from mild to severe wear passing through 80 bar of pressure to 90 bar was observed for both materials.

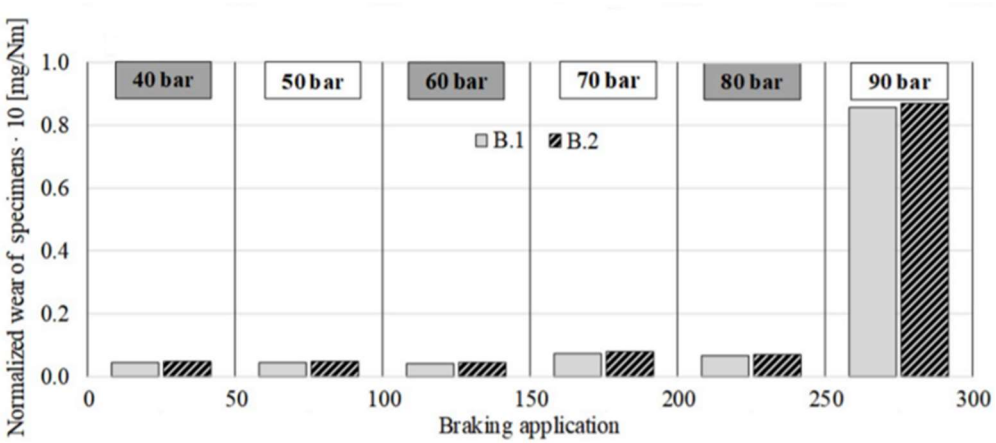

Figure 3.6: Normalized wear of two friction materials (B.1 and B.2) for different pressures [17].

Table 3.1 specifies the typical automotive braking conditions and the usual response in terms of both friction coefficient and wear.

Table 3.1: Typical automotive brake conditions [1].

	Normal braking	**Heavy braking**
Typical decelerations during braking (m/s^2)	<2	>5
Nominal contact pressure (MPa)	0.2 - 1.5	1.1 - 4
Average surface temperature (ºC)	<300	>300
Pad wear, ka (m^2/N)	$5*10^{-15}$ - $4*10^{-14}$	Increases with the temperature
Friction coefficient	0.4 - 0.6	Decreases with the temperature

3.3 Disc

The brake discs are connected to the vehicle wheel, and both rotate at the same angular velocity. In a vehicle, the front axle is submitted to a higher stress due to the transferred load during the braking. In this case, the ventilated brake discs are more appropriate, since more effective in dissipating heat as compared to solid brake discs. The heat exchange in ventilated discs is more efficiently thanks to the inner channels and the design involving two annular discs separated by vanes. Solid discs are typically used in the rear axle since relatively lower temperatures are involved during the braking. Both disc configurations are given in Figure 3.7.

Figure 3.7: Typical ventilated and solid brake discs.

The brake discs are usually made of the pearlitic grey cast iron with 3-4 wt.% of carbon. Their typical microstructure can be appreciated in Figure 3.8, showing graphite flakes in a pearlitic matrix. Such microstructure confers to the disc good thermal conductivity, good wear resistance and machinability. The low cost of the grey cast iron is also another characteristic which makes this material a good choice for the brake discs.

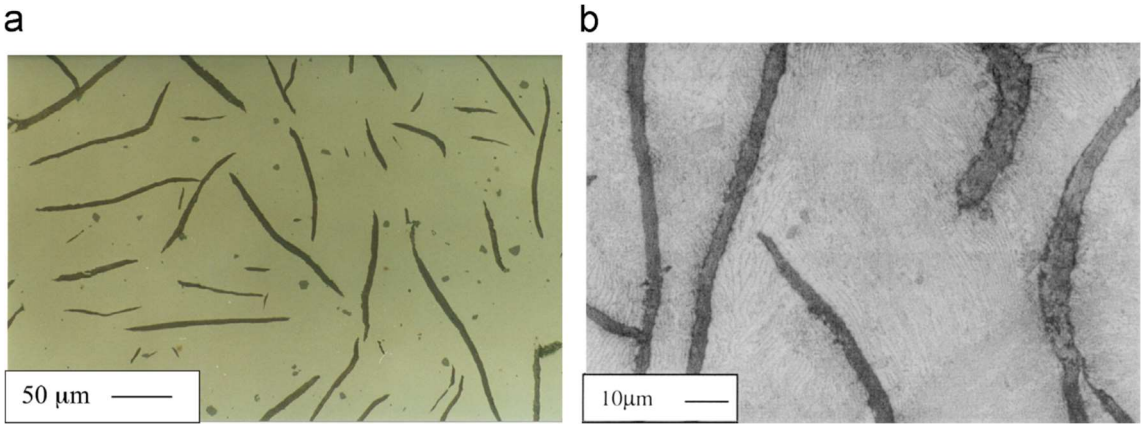

Figure 3.8: Micrograph of a typical microstructure of the pearlitic cast iron disc: (a) graphite flakes, (b) pearlitic matrix (2% Nital etching) [18].

Ceramic matrix composites and aluminum-based metal matrix composites are alternative materials for the brake discs, exhibiting a good wear resistance, although more expensive as compared to the grey cast iron [19].

3.4 Pads

It is required that pad materials maintain a sufficiently high and stable friction coefficient, even in extreme brake conditions. Good wear resistance and good compatibility with the disc are further expected performances of the pads [20, 21]. Figure 3.9 shows the schematic of a brake pad, composed by four main layers:

- **Backplate:** usually made by iron, is the base of the pad and provides the mechanical strength required for the applying pressure during the braking.
- **Underlayer**: made by organic materials, it is responsible for thermal insulation. In addition, it improves the comfort during the braking by its damping properties.
- **Adhesive:** used to attach the underlayer on the backplate.

- **Friction material:** made by many different ingredients held together by a polymeric binder, e.g., a phenolic resin, is the material in contact with the disc during the braking.

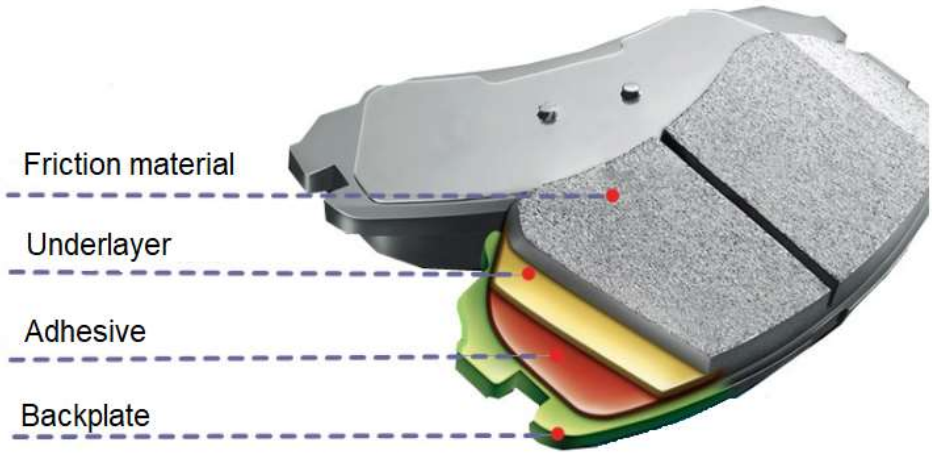

Figure 3.9: Schematic representation of a brake pad (adapted from ref.[22]).

3.4.1 Pads friction materials

The friction materials for brake pads are composites, which may contain up to more than 20 ingredients. The number of the ingredients is already high enough to make this a rather complex material. However, the complexity is even higher considering that the pads are made by compounds from all three main classes of materials, i.e., metals, ceramics and polymers. Such diversity of chemical-physical properties of the different ingredients in brake pads makes the selection of the right composition a challenging task. Of course, the amount and the size/shape of the compounds affect the performance of the pads and must be defined. In view of such complexity, the tribological response of the friction materials are very tricky to be fully predicted and understood. Considering their composite character, the behavior of the resulting material is not just the linear combination of the properties of each individual ingredient. Figure 3.10 shows a typical microstructure of a commercial friction material with the indication of some of the main ingredients. A very heterogeneous microstructure can be appreciated, featuring components in different compositions, shapes and sizes.

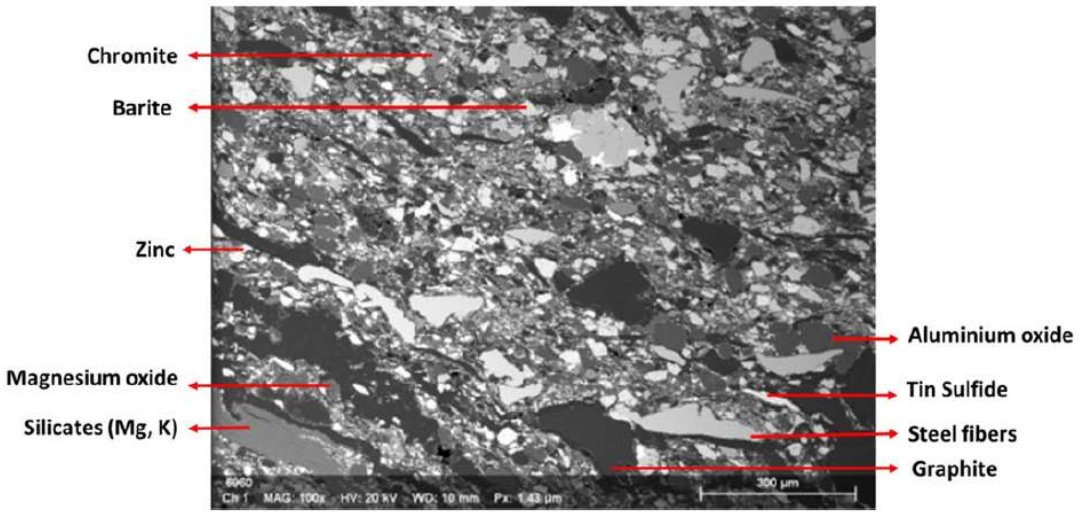

Figure 3.10: Micrograph of a typical microstructure of a pad material [26].

All the ingredients need to be bound together and this specific role is played by the matrix. Friction materials based on organic matrix are typically used for lightweight vehicles and they are commonly classified according to its metallic content [27]. The classes, as well as their main characteristics, are specified in Table 3.2.

Table 3.2: Organic matrix friction materials: classification and main characteristics [27, 28].

Class	Metallic content	Friction coefficient	Advantages	Disadvantages
Semi-metallic	> 50%	0.35-0.55	- Improved performance at high temperature - Good durability	- Corrosion at humid conditions - High disc wear
Low-metallic	> 30% < 50%	0.35-0.55	- Stable for high speeds and high temperatures - Better overall performance	- High noise
NAO (non-asbestos organic)	> 10%	0.3-0.4	- Low wear - Low noise	- High pad wear at high temperatures - Lower performance

The metallic content really affects the characteristics of the brake pads. Nevertheless, the advantages and disadvantages displayed in Table 3 are not exclusively due to the amount of metallic components added to the friction materials. For example, the NAO are materials with high content of binder (polymeric material), which is the reason of the low resistance at high temperature displayed by these materials [27, 29].

Semi-metallic (SM), low-metallic (LM) and a NAO friction materials where pin-on-disc tested by Wei et al. [30], at room temperature. As shown in Figure 3.11, the brake pad temperature increases as both pressures and velocities (represented by “mode number”) increase. In all tested conditions, it is noticed a higher temperature achieved by semi-metallics materials, which is line with the higher metal content in this kind of pad material.

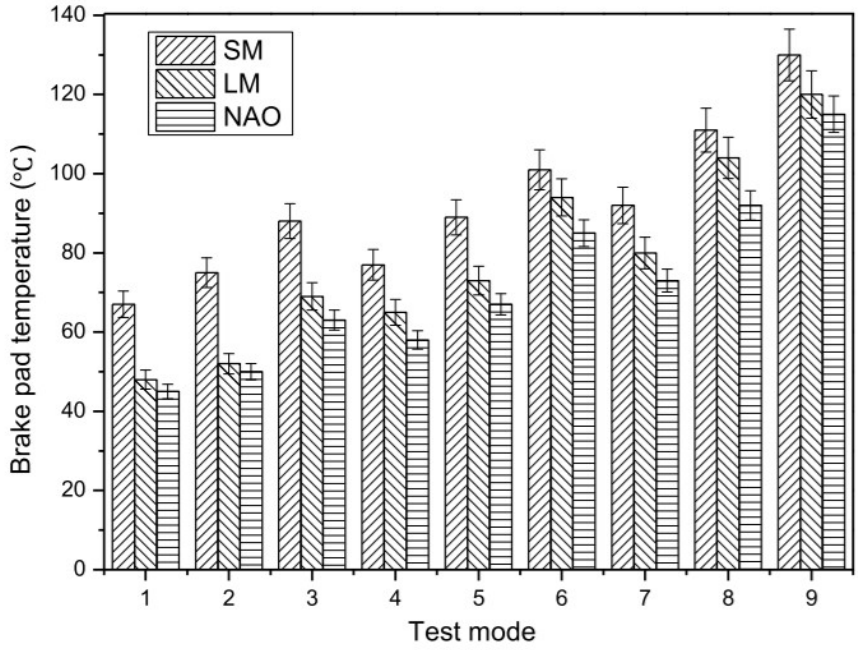

Figure 3.11: Brake pads temperatures displayed by SM, LM and NAO brake pads [30].

Due to the complex pad compositions, the manufactures of friction materials do not use to publish their exact formulation. In any case, each ingredient added to the pads plays a specific role, some of them may also comply with more than one simultaneously [27, 29]. Based on their function, the ingredients of a pad friction material are divided into four main classes, as described in the follow.

Binder: has the function of holding together all ingredients, maintaining the structural integrity of the pads and ensuring proper performances to all of the components in the friction material.. The phenolic resin is typically chosen as a binder for brake friction materials [31, 32]. The main properties which make the phenolic resin a good binder are: good mechanical

stability, mechanical strength, good wetting capability with most of ingredients and relatively high friction coefficient and low wear with respect to other polymers. Furthermore, the phenolic resin increases the damping capacity of the friction materials with positive consequences on the noise [33, 34]. As discussed in section 3.2, the thermal degradation tendency displayed by most of polymers is an important issue concerning the integrity of pad materials at high temperatures. In fact, during the braking, the contact temperatures can exceed 300°C, inducing the degradation of the matrix and consequently decreasing of mechanical stability of the composite [35, 36]. This phenomenon can lead to the so called “fade”, when a drastic reduction of the friction coefficient compromises the proper operation of the brake system. Several studies [33, 37-39] suggest that additives in the phenolic resin, such as hydroxyl compounds or methylene linking groups, can improve the heat resistance of the pad matrix. Figure 3.12 shows the molecular structure of two modified phenolic resins tested by Hong et al. [37], in comparison to the structure of straight phenolic resin. In this investigation, the resin containing both additives displayed better heat resistance than the resin without any additive, which can be attributed to the more reticulated structure and strong bonds exhibited by these materials.

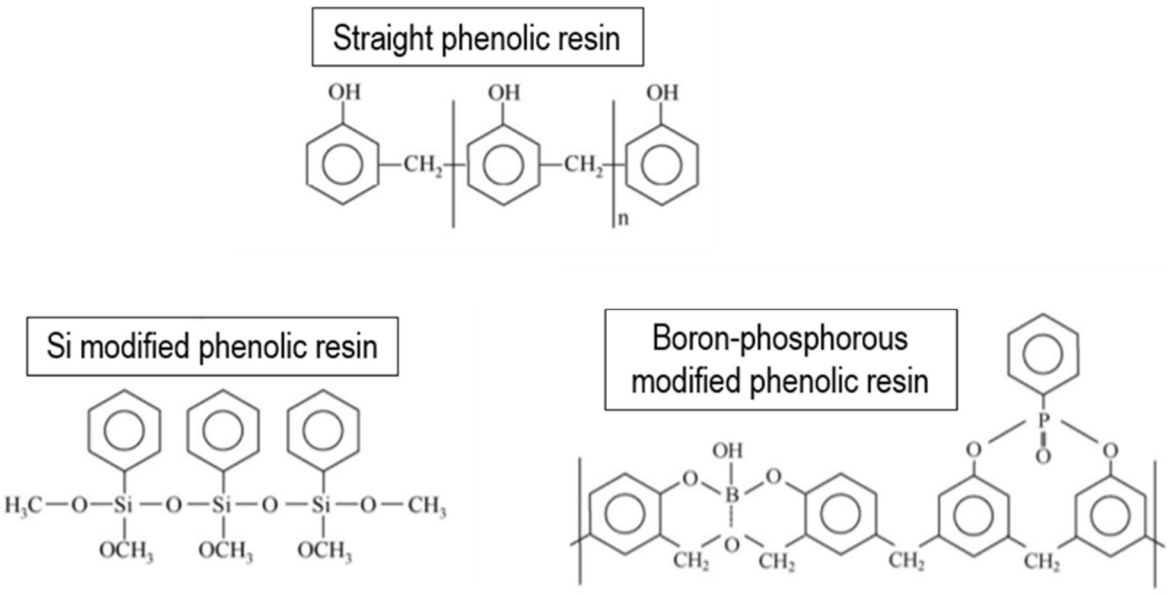

Figure 3.12: Molecular structure of straight phenolic resin in comparison to two modifieds additives added to phenolic resin [37].

Besides the phenolic resin, other possible binders for brake pad are: polyimide resin, cyanate ester resin and polyurethane rubber [20].

Reinforcements: responsible to provide mechanical strength, the reinforcements are mainly fibers and hard particles. They typically work as primary plateaus, playing an important role in the formation of an appropriate friction layer between the mating surfaces. The reinforcements should also provide a suitable friction properties and thermal stability to the friction materials. Different types of reinforcing fibers can be used in a friction material, such as mineral fibers, metal fibers and natural (derived from vegetable source) fibers. Due its dimensional, one critical aspect is the good adhesion to the matrix [23, 40-41].

Friction modifiers: added to the pad friction materials in order to modify the friction coefficient as well as the wear rates. They are divided between abrasives and solid lubricants. Abrasives comprise all materials with a hardness greater than the gray cast iron disc, i.e., around 5 in Mohs scale. In general, they increase the friction coefficient and improve the overall wear resistance. However, a high content of abrasives in a friction material can lead to an instability of the friction coefficient and an excessive wear of the counterface disc. Oxide powders, carbides and silicates are examples of abrasives used in pad materials. Solid lubricants, such as MoS_2, coke and graphite, are used to control and stabilize the friction coefficient and the wear, thanks to their ability of forming a lubricant layer between the surfaces [25, 42-44].

Fillers: the main role of these ingredients is decreasing the material cost without changing the performance of the pads. They may also help the dimensional stability during the pad production and minimize the noise during braking. The main characteristics of an appropriate filler are: low cost, high thermal stability and good adhesion to the matrix. Barium sulphate, calcium carbonate and clays are typically used, although the right filler to be used depends on the other ingredients that compose the pad [23, 25, 45].

Usually, even in case when a commercial formulation is published, some information are still not very precise. An example is given in Table 3.3.

Table 3.3: Nominal composition of Volvo 850 commercial brake pad material [46].

Structural component	Ingredient	Amount (wt.%)
Fibers	Steel-aramid and glass	30
Matrix	Binder	8
	Other	11
Friction modifiers	Brass and bronze	15
	Graphite	15
	Metal sulphides	8
Abrasives	Quartz	5
Fillers	Clay and iron oxide	8

3.4.2 Copper and the Cu-free friction material formulations

Over the last decades copper has been widely used in brake pads, featuring concentrations between 5 up to 20 % [23]. This element can be added either as pure copper or as an alloy (e.g., brass), in both fiber and powder forms. Due its good thermal conductivity, displays beneficial effects on the removal of heating and thereby on the contact temperature distribution. When used as fiber, copper behaves as a reinforcement and forms primary plateaus [26, 46]. Several studies [47-49] report that copper contributes to the formation of a well compacted friction layer, thus improving the wear resistance and friction coefficient stabilization. Moreover, copper would enter the friction layer and induce the clustering of wear debris in coarser particles, which tend to fall down on the ground avoiding health respiratory issues [48-50].

On the other hand, copper has been reported as a hazardous pad constituent once several studies demonstrated that, when released as an airborne particle (lower than 10 μm), it can penetrate in the human body and cause oxidative stress into tissues [51, 52]. Moreover, it is reported that the coarse wear fragments containing copper can achieve rivers and lakes by the rainfall and intoxicate the aquatic species [53]. Due to these detrimental characteristics, the reduction of copper in brake pad formulations starts to be imposed by

some governments, particularly in United States, and the manufacturers are facing with the huge challenge of developing the so-called Cu-free formulations.

Since the copper plays several roles on the friction materials, different strategies have been proposed in order to reduce/replace the copper without compromises the performance of the pads. The optimization of the ingredients already added to the formulations of the friction material is one of them. In this regard, more optimized concentrations, size and shapes of the constituents are studied [54-56]. In terms of substitute ingredients, graphite particles seem to be a good alternative due to their contribution to the formation of the secondary plateaus in the friction layer. A similar beneficial effect has been demonstrated by the addition of barite in sufficiently high concentrations [55, 56].

Some investigations reported good performances of a commercial Cu-free friction materials [57, 58]. The friction coefficient and wear of two Cu-free friction materials were compared to a Cu-containing Lyu et al. [57], by PoD tests. The main results are shown in Figure 3.13, when both Cu-free materials display comparable friction coefficient and disc's wear compared to Cu-containing. Moreover, one Cu-free features better wear resistance of the friction material.

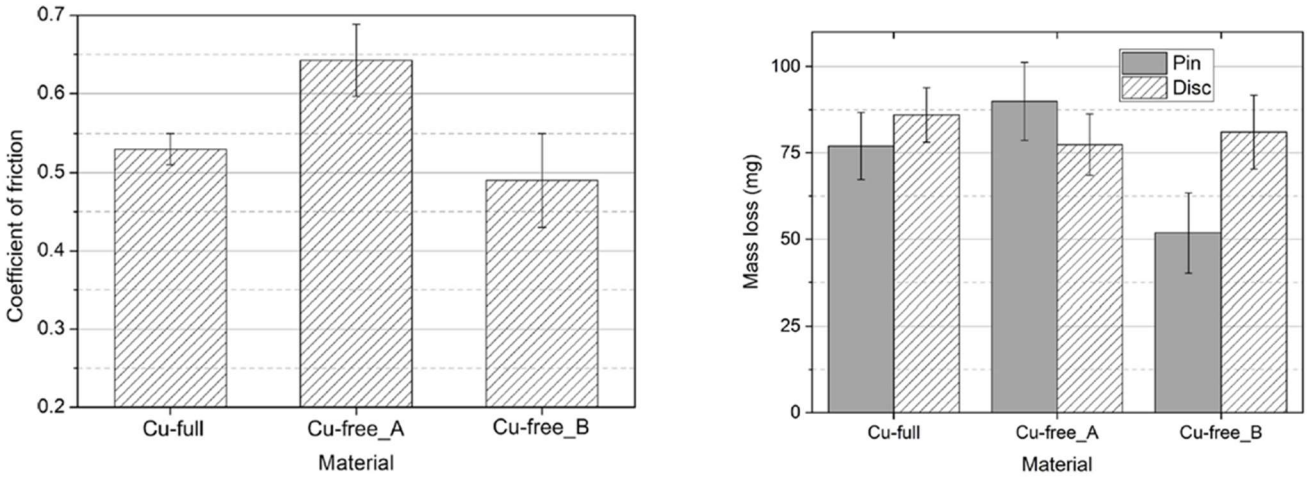

Figure 3.13: Friction coefficient and wear of a Cu-containing and two Cu-free friction materials [57].

A good performance displayed by a Cu-free friction material is also reported by Barros et al. [58]. As shown in Figure 3.14, even at high temperatures, the Cu-free (V0) features higher friction coefficient than both Cu-containing materials (V10 and V30). However, the absence of copper appears to be detrimental for the wear resistance, mostly at high temperatures.

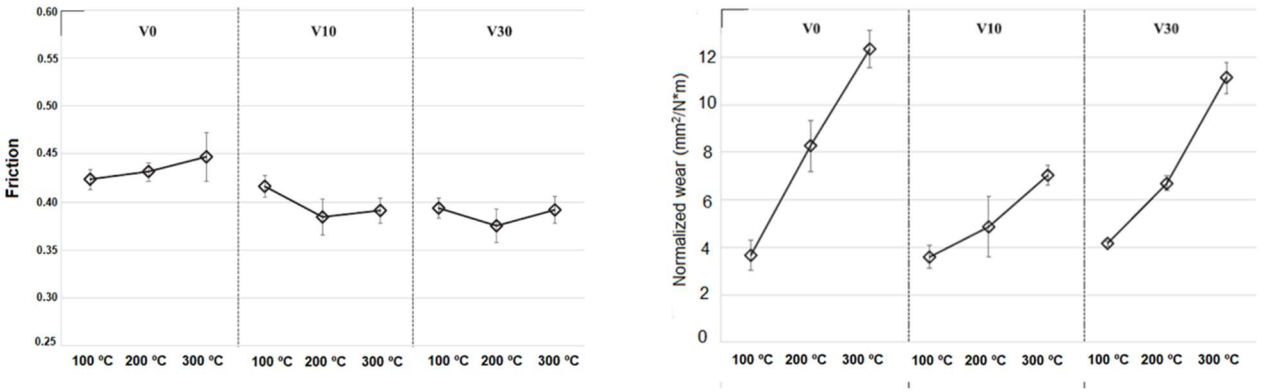

Figure 3.14: Friction coefficient and wear for Cu-free (V0) and Cu-containing (V10 and V30) friction materials [58].

Chapter 4
Friction layer

This chapter is dedicated to discussing the layer usually developing at the disc/pad interface, thus affecting the performances of the tribological system.

The role played by the friction layer on brake systems and its characteristics for different type of pad materials are explored. Nevertheless, particular attention is given to the friction layer formed on low-metallic materials, since this is the material used on the investigations present on this thesis.

4.1 Definition and relevance

In disc brake systems, as in most friction systems, a third body usually forms between the mating surfaces under sliding conditions. This new interface material is called friction layer and has been extensively studied since its characteristics are paramount for the tribological response of the system [59-61] Wirth et al. [60] reported that friction behavior of a pad/disc couple depends on the composition of the friction layer. However, according to the Authors, the thickness and morphology of the layer seems not affect the friction performance. Österle et al. [59] observed a correspondence between the stability of the friction coefficient and a friction layer well formed on the mating surfaces. As discussed in section 3.1, a stable friction coefficient is a main requirement for brake systems. In addition, Verma et al. [61] reported the formation of the friction layer on the friction material as essential for a mild wear regime, bellow 170 °C.

A wear-protective action is also attributed to the development of oxide layers between the sliding surfaces. However, this layer cannot form without the wear debris. Suh et al. [62] observed an increasing of the wear when loose wear debris are removed from the friction material surface. Leheup et al. [63] reported the absence of an oxide layer covering the surface when the wear particles were removed, leading an increase of the wear. Oxide particles artificially supplied to the rubbing surfaces in the investigation conducted by Iwabuchi et al. [64] improved the wear resistance due to the easily formation of compacted

oxide layers. On the other hand, when the wear particles are not well compacted into solid layers, they may act as abrasive, accelerating the wear rates [65].

4.2 Friction layer on low-metallic and semi-metallic friction materials

In low-metallic (LM) and semi-metallic (SM) friction materials, the friction layer is constituted by primary and secondary plateaus. The primary plateaus are fibers and hard particles added to the pad friction material. Thanks to their great wear resistance, these constituents remain on the surface acting as a support and nucleation sites for growing secondary plateaus. Instead, the secondary plateaus are a combination of wear debris from both friction material and disc, compacted together due to the braking conditions.

The debris originated from the wear of both friction material and disc may are directly released out of the system or may remain trapped between the mating surfaces. Those stay in the interface are continuously milled and flowing through the maze created by the non-contact regions, called lowlands [64, 67]. Figure 4.1 shows a SEM micrograph of contact plateaus formed on a pad surface, when regions of no contact can be also appreciated. The lowlands usually comprise the pad constituents with less wear resistance, such as fillers and polymeric resin.

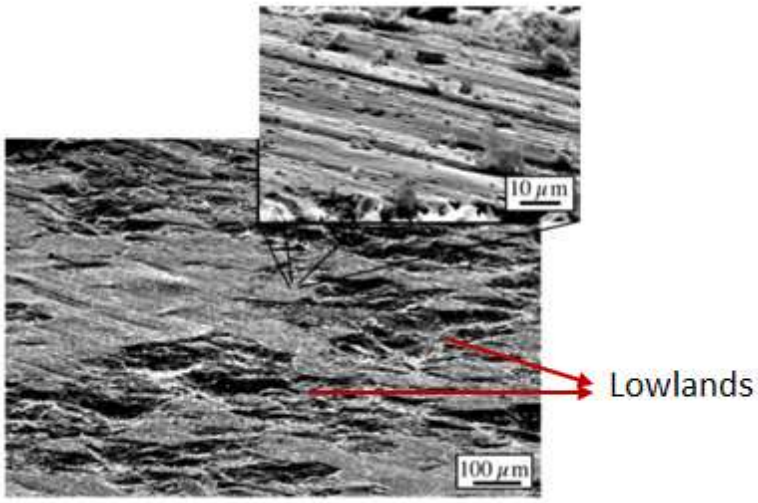

Figure 4.1: Micrograph of a pad surface showing the contact plateaus and the lowlands [66].

Once the debris flowing through the lowlands are faced by the barrier created by the primary plateaus (fibers and hard particles), they pile up and starts to be compacted by simultaneous action of contact pressure, sliding shear stress and frictional heat. According

to Österle et al. [59], fine particles easily remain in the surface while coarse particles are preferentially ejected from the contact region. Both primary and secondary plateaus are well defined in Figure 4.2, a micrograph of a pad surface after a sliding test.

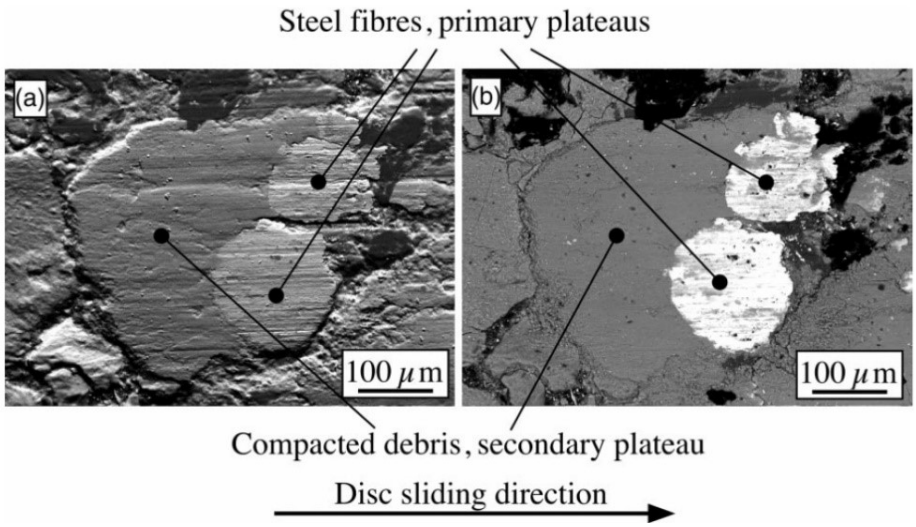

Figure 4.2: Micrograph of primary and secondary plateaus [66].

According to Eriksson et al. [66], the formation and growth of a compact secondary plateaus require a sufficient friction energy and normal load acting on the surfaces, combined with a provision of such small wear debris. A limited space between pad and disc is also reported as recommended for the secondary plateaus growing.

Cho et al. [68] describe an increasing thickness of the friction layer up to a temperature of 250 °C, and then a rapid decreasing above 300 °C. The temperature positively influences the formation of the friction layer since the debris are easily compacted and sintered. However, when the critical temperature is reached, the degradation of the matrix takes places and does not allow for the continuous development of the friction layer.

After formed, the friction layer remains quite stable until the detachment of the supporting primary plateaus. However, instabilities on friction conditions and insufficient normal force to maintain the layer adherent to the surface can lead to the detachment of the secondary plateaus as well. Therefore, each time the brake pressure is reduced during the sliding, the disruption of the friction layer may happen [66].

Of course, newly installed pads have no friction layer on their surfaces. In this regard, Verma et al. [69] and Wahlstrom et al. [70] studied the period called running-in, in which the friction coefficient increases until achieved a steady-state. The raise of the friction coefficient

seems to be accompanied by the development of the friction layer on the mating surfaces. After the running-in period, a dynamic process of formation and disruption of the friction layer takes place. Then, the steady state is reached once the formation rate equals the disruption rate [71].

The area covered by contact plateaus reported by Eriksson et al. [66] is up to 20% of the superficial area of the pad. More recent investigations [72, 73] describe this fraction between 50 to 60%. Figure 4.3 displays the identification and quantification of the contact plateaus from micrographs of a low-metallic pad worn surface, investigated by Leonardi et al. [73].

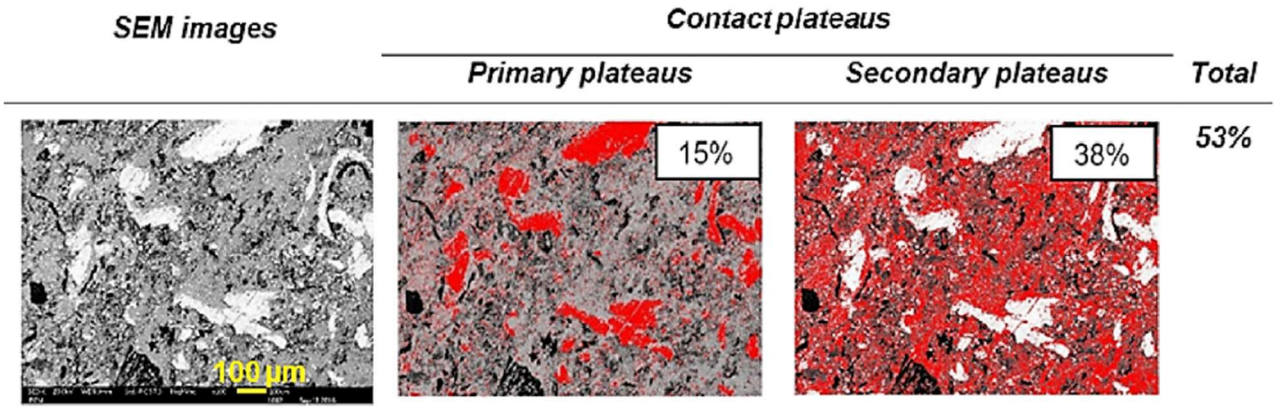

Figure 4.3: Identification and quantification of primary and secondary plateaus [73].

4.3 Friction layer on NAO friction materials

The friction layer developed on the surfaces of NAO friction materials differs quite a lot respect those formed on LM and SM [72, 74]. Usually, NAO formulations do not include large metallic fibers or hard particles that can act as primary plateaus. In addition, during the sliding, a very flat surface is formed. The lowlands, discussed in section 4.2, almost do not exist on the surface of these materials. In fact, the roughness of worn surface reported in the literature for NAO materials is around 3-4 times lower than LM and SM. This behavior is mostly due to the high relative content of organic binder, creating a smoother surface by the action of sliding forces. Figure 4.4 shows a comparison between LM and NAO surfaces after tribological tests [75]. A distinct topography can be appreciated, with LM featuring a mix of lowlands and contact plateaus well-dispersed on the surface. Instead, in case of NAO, the contact plateaus are more evenly distributed, comprising almost whole surface.

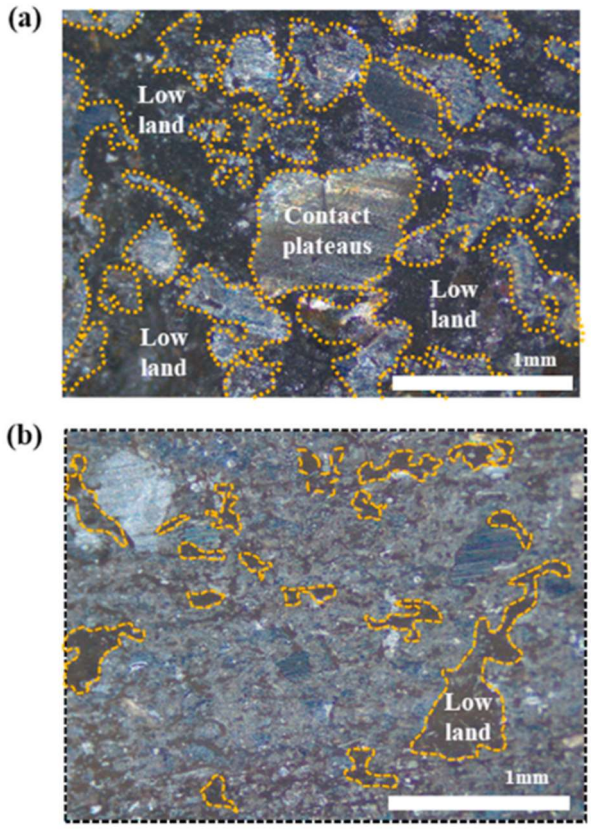

Figure 4.4: Worn surfaces of the (a) LM and (b) NAO pads materials observed using an optical microscope [75].

4.4 Composition

The composition of primary plateaus depends on the ingredients added to the friction material able to play this specific role. Iron and copper, in form of fibers, are common elements composing the primary plateaus on LM and SM materials. Copper fibers are usually plastically deformed in the sliding direction, which makes the iron fibers more efficient working as primary plateaus.

Being the secondary plateaus the result of the piling up and compaction of pad and disc wear debris, they would contain the elements from both. However, as discussed in section 3.4.1, the formulations of the friction materials involve a huge number of ingredients and some of them may easily become part of the friction layer. In any case, investigations addressing the friction layer composition reported iron oxide as the main constituent [61, 63]. In fact, the discs are mainly composed of iron and the fine particles resulting from their wear usually became part of friction layer.

Chapter 5

Particulate Matter Emission

Particulate matter (PM) is composed of liquids and solids particles dispersed in the air, mostly released into the urban environment by non-natural sources, such industries, power plants, domestic heating and traffic. PM size distributions span from few nanometers up to few micrometers. Among the various PM characteristics promoting adverse health effects, two characteristics are here highlighted:

- **Small size:** some components of the PM may feature small diameter and thus easily access to the respiratory system, with the additional risk of reaching the blood circulatory system;
- **Heavy elements**: PM may contain toxic elements, such as heavy metals.

Exposure to PM dispersed in the air has been ranked as a significant risk factor for mortality. It is estimated that in 2015, 4.2 million premature deaths around the world happened as a consequence of the adverse effects caused by PM [76].

This chapter is addressed to discussing issues related to the particulate matter originated from disc brake systems. The estimated contribution on the total amount of PM released into environment is reported, as well as its consequences. Since this thesis takes advantages of characterization techniques for better understanding the wear mechanisms originating the brake emissions, particular attention is given to the main characteristics of PM described in relevant investigations.

An important information to keep in mind is that PM from brakes starts to be extensively studied on the last few years only; several aspects are still controversial. In addition, the lack of standard testing procedures commonly yields incomparable results and contradictory conclusions.

5.1 Non-exhaust PM emissions

Road traffic related emissions are a significant source of pollution and generation of PM emissions, particularly in the urban areas. They are usually divided into exhaust and non-exhaust emissions, indicating respectively: emissions originated from the combustion

of fossil fuels, emitted via tailpipe, and emissions from other traffic and vehicle sources, such as tyres, brakes, road and resuspension. The non-exhaust emissions can be directly emitted into environment or may remain trapped onto the vehicle's parts.

Particulate matter from non-exhaust sources is comparatively becoming more prominent than the exhaust. The chart of Figure 5.1 shows the amount of traffic related emissions PM10 (PM with aerodynamic diameter smaller than 10 μm) released from both exhaust and non-exhaust sources, in European Union countries, Norway and Switzerland over the years [77]. Thanks to regulations established, a comprehensive knowledge of the exhaust emissions was built up and this kind of emissions have now been significantly reduced. On the other hand, the status of non-exhaust emissions remains almost the same, featuring even higher values than exhaust ones. Studies including other countries, outside Europe, report similar results, describing the contribution of non-exhaust emissions to the total traffic related PM10 nearly equal of the exhaust emissions [78, 79].

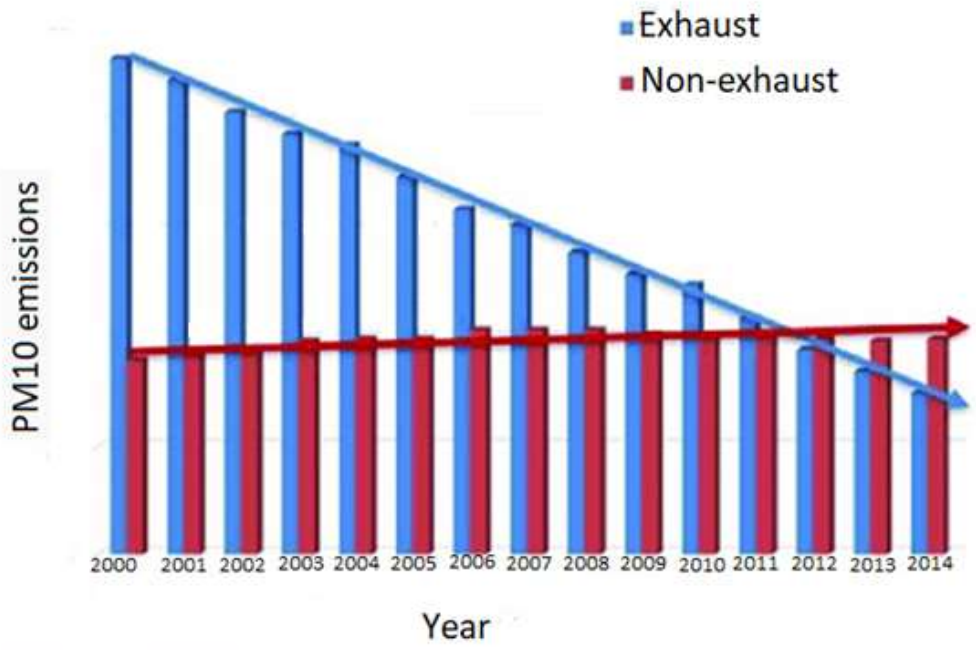

Figure 5.1: PM10 emission from road transport exhaust and non-exhaust 2000-2014 for EU15, Norway and Switzerland [77].

The relative amount of non-exhaust emissions from each source can significantly change according to different real-world driving conditions and vehicle types. In general, it is estimated that between 15-55% of the total mass emitted from non-exhaust sources

comes from the brakes of the vehicles. With respect to the total mass loss, a relevant part of the brake wear became airborne, ranging from 35 up to 55% [80, 81].

New design approaches for brakes, not based on friction contact, should lead to lower brake emissions. This is the case of regenerative braking system, used in electric and hybrid vehicles. However, these vehicles are also equipped with a disc brake system, used as a back-up in case of sever solicitations. Given that the tyre and road wear emissions increase with heavier vehicles, a powertrain and an extra braking system consequently resullt in higher emissions. The net balance between the reduction in brake emissions and the increasing in the emissions by other sources may not affect the total amount of non-exhaust emissions released [82]

5.2 Health issues

Exposure to PM emissions is associated with several human ill-health and premature mortality. In recent years, health concerns related to the PM released from brakes have attracted a significant attention, mostly due to their relatively small size and presence of toxic elements.

The particle's ability of overcoming the barriers of the human body is linked to their size: the smaller they are, the deeper they can penetrate [83, 84]. Around 60% of the particles released from disc brake systems are smaller than 2.5 μm in diameter. As indicated in Figure 5.2, inhaled PM10 can access the nose and throat, while PM2.5 (PM with aerodynamic diameter smaller than 2.5 μm) may go deeper on the respiratory system; causing irritations and inflammatory response, respectively. Particles with aerodynamic diameter smaller than 0.1 μm can achieve the blood circulatory system inducing oxidation reactions and biological stress, with potential damage to the DNA. Moreover, once in the circulatory system, these particles can go through different parts of the body, even reaching the nervous system and traversing the placental barrier [85, 86]

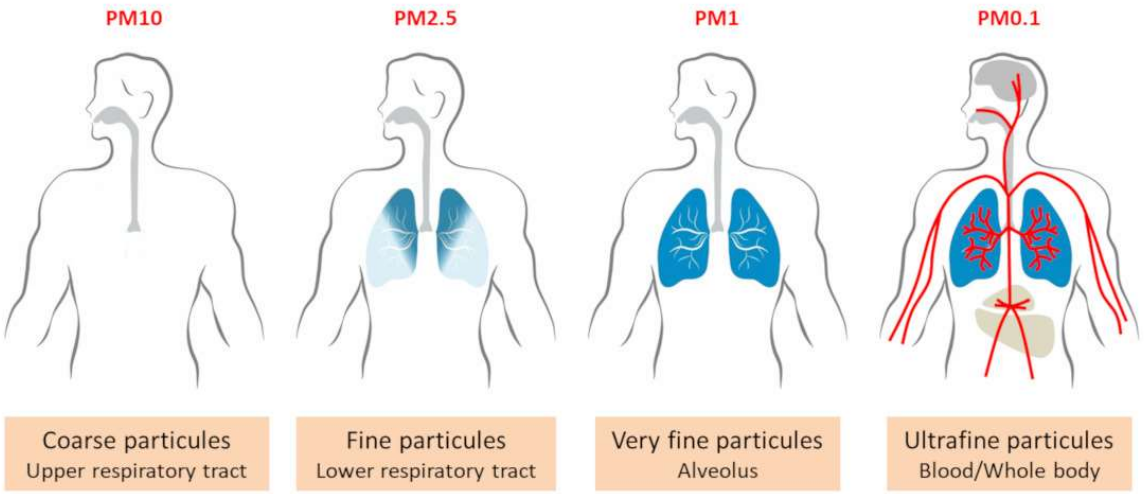

Figure 5.2: Schematic example of the PM penetration in the human body based on particle's size [87].

Regarding the chemical composition of the PM from brakes, adverse health effects can be induced by some key harmful particles, mostly composed of the metals present in both the disc and the pads, such as copper, nickel and chromium [88]. Furthermore, adverse outcomes like pro-thrombotic effects, increased heart rhythm, and elicits pro-inflammatory effects have been associated to the metallic content in the PM [89]. Ostro et al. [90] describe a correlation between inhalation of fine particles containing Pb, Cu, Fe, Ca, Zn, Mn, V and Ti and daily mortality.

5.3 Legislation

Currently, there is no specific regulation concerning the non-exhaust emissions. Although this matter has been increasingly discussed towards its reduction, the lack of solid understanding across several aspects and the no standardized measurement procedures restrains the establishment of regulations.

Despite the absence of regulations, the European Commission already establishes research projects and programs addressing the reduction of the non-exhaust emissions. One of these is the project REBRAKE, developed from 2013 to 2017 by Brembo SpA, Kungliga Tekniska Höegskolan and Università degli Studi di Trento, aiming at a mass reduction of at least 50% of PM10 from brake systems. The goal was achieved through improvements on pad and disc materials and their interactions during the braking action. More recently, the EU-funded project LOWBRASYS (Low Environmental Impact Brake

System) was developed. Coordinated by Brembo SpA in collaboration of nine partners among industries and educational institutions, including the Univeristà degli Studi di Trento, the project aimed the decreasing of 50% PM brake emissions. Many strategies were followed to achieve the objective and they are given in Figure 5.3.

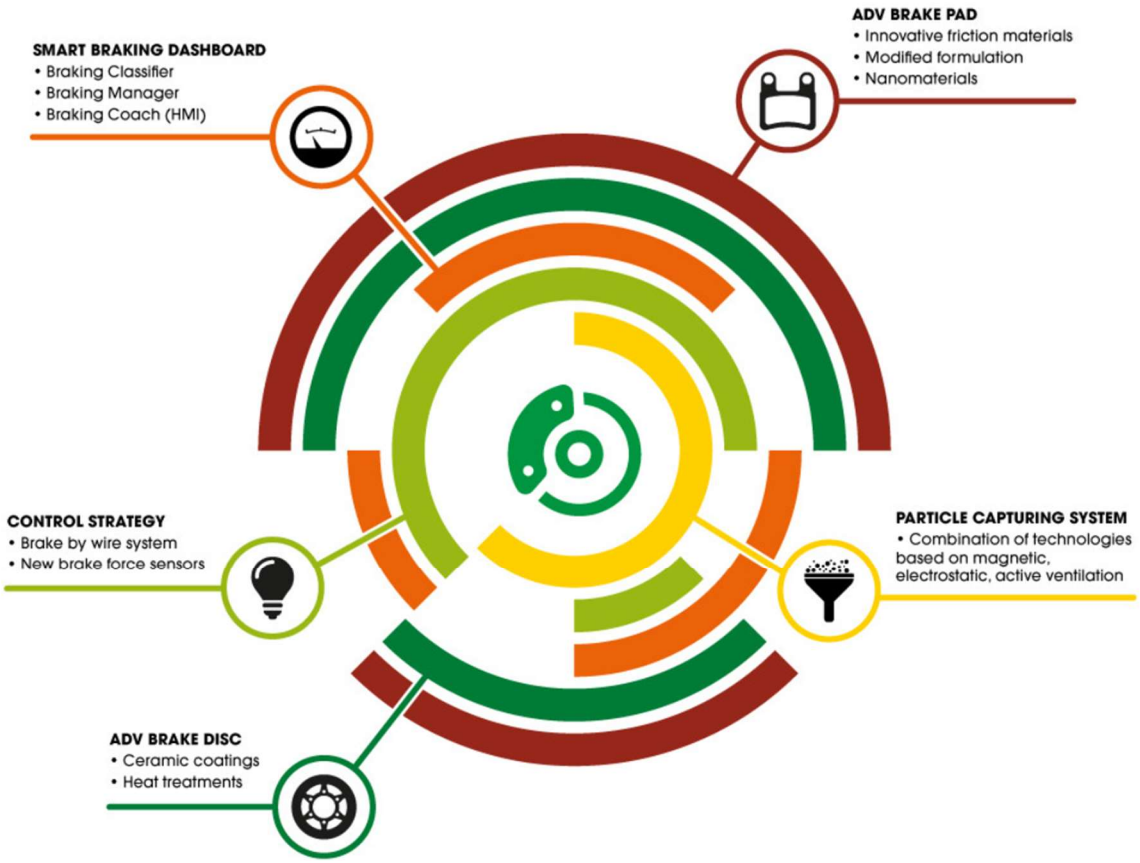

Figure 5.3: Strategies of the project LOWBRASYS in reducing the PM emissions [91].

5.4 PM metrics

Particulate matter can be measured in terms of either mass concentration (μg/m^3) or number concentration (#/cm^3). PM standards are mass-based: PM10 and PM2.5 are defined as the mass concentration of particles with aerodynamic diameters below 10 μm and 2.5 μm, respectively.

Conventionally, the airborne particles are divided into three main classes, accordingly to their aerodynamic diameter (d), defined as the diameter of a sphere of unit density (1 g/cm^3), which settles in still air at the same velocity as the particle in question:

- Coarse particles: 10 μm < d ≤ 2.5 μm
- Fine particles: 2.5 μm < d ≤ 0.1 μm

- Ultrafine particles: d < 0.1 μm

It is important to highlight that the airborne particles after being released may undergo transformations which modify their number and size, such as agglomeration and condensation [72, 81].

Beyond the mass and number concentration, information regarding their size distributions is usually provided by measurements of PM. In case of brake emissions, several investigations report the mass distribution by the converted values of number distribution, based on the assumption of a specific density of the particles. However, different values of densities for brake emissions have been used in the literature, which may lead to not easily comparable results.

5.5 Characteristics of PM brake emissions

5.5.1 Size

Different size distributions of PM from brakes are reported in the literature. Mosleh et al. [92] pin-on-disc (PoD) tested a NAO and a LM friction materials, under pressure between 0.125 and 1.25 MPa, at high and low speeds. A bimodal size distribution was recorded for particles emitted in all conditions. The Authors observed one peak at approximately 0.35 μm in diameter and another peak varying from 2 to 15 μm. As shown in Figure 5.4, the pressure seems not to affect the mode of fine particles. However, in both low and high speeds, the peak of coarse particles shifts to higher values by increasing pressure.

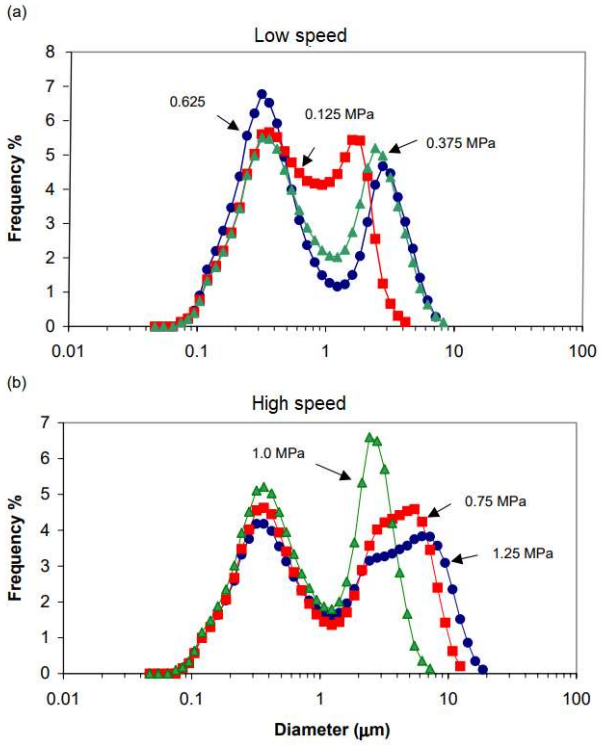

Figure 5.4: Size distribution of wear particles generated during the (a) low-speed (sliding speed = 0.275 m/s) and (b) high-speed tests (sliding speed = 5 m/s) [92].

Wahlström et al. [93] investigated the size and shape of brake emissions, PoD tested a LM and a NAO materials. The Authors reported a bimodal size distribution with peaks at 0.28 and 0.35 µm for both materials. In addition, they observed most airborne particles featuring diameter smaller than 2.5 µm. A model proposed by Olofsson et al. [94] for determining the number of airborne particles generated in a contact disc/pad describes three peaks of size distribution: one of ultrafine particles at 0.08 µm diameter, one of fine particles around 0.35 µm and a coarse particle peak around 2 µm. Nosko et al. [95] also investigated the emissions from LM and NAO materials, PoD tested. In this study, two different instruments were used to measure the number distribution of emitted particles, in order to include a higher size interval. Merging the data from both instruments, the Authors reported a peak of fine particles between 0.3-0.6 µm.

Tests using a dynamometer have displayed different results. Iijima et al. [96] tested a NAO material simulating typical urban driving conditions and severe downhill braking. The Authors reported a peak at approximately 1 µm diameter, shifting to the coarse side with increment of the disc temperature. An investigation carried out by Sanders et al. [81], the three classes of friction materials (LM, SM and NAO) were tested using two different cycles: an urban program (deceleration from 1.4 m/s^2) and an Auto Motor and sport magazine

(deceleration from 7.9 m/s^2). No difference between the materials was detected in terms of size distribution, all featuring a peak ranging from 1 to 2 μm.

In Table 5.1 the main results of the data here considered are summarized.

Table 5.1: Summary of selected investigations on size distributions of brake PM.

Investigation	Type of test	Friction material	Instrument used and range of size measured	Peak of number size distribution
Mosleh et al. [92]	PoD	LM NAO	▪ LA-700 laser scattering analyzer: 0.04–262 μm	▪ 0.35 μm ▪ 2 to 15 μm
Wahlmström et al. [93]	PoD	LM NAO	▪ GRIMM spectrometer: 0.25–32 μm ▪ PTrak counter: 0.02–1 μm	▪ 0.28 μm ▪ 0.35 μm
Nosko et al. [95]	PoD	LM NAO	▪ TSI Fast Mobility Particle Sizer: 0.0056–0.56 μm ▪ TSI Optical Particle Sizer 3330: 0.3–10 μm	▪ 0.3-0.56 μm
Iijima et al. [96]	Dynamometer	NAO	▪ Aerodynamic particle sizer spectrometer: 0.5–20 μm	▪ 1 μm
Sanders et al. [81]	Dynamometer	LM SM NAO	▪ Impactor ELPI: 0.29–10 μm	▪ 1 - 2 μm

Size distributions featuring unlike peaks maybe resulted from different tests parameters and configurations. In this regard, Sanders et al. [81] suggested the difficulties inherent in sampling and transporting micron sized particles as a reason of discrepancies between size distribution measurements. Kukutschovà et al. [97] reported an inconsistency between the data of particle size distribution and real size of particles collected on dynamometer tests: coarse and fine particles observed on SEM and TEM were in fact formed by agglomerates of smaller particles. In fact, several studies also reported fine particles mainly consisting of agglomeration of smaller particles [72, 98, 99].

Regarding the peak of mass distribution, Straffelini and Gialanella [72] summarized several investigations using dynamometer with LM, SM and NAO materials and they report a peak ranging from 3 to 8 μm.

5.5.2 Density

In an investigation conducted by Nosko and Olofsson [100], the effective density of the PM from brake system was determined based on the size distribution of the generated airborne particles. They conducted PoD tests with five LM materials (M1, …, M5) and one NAO material (M6), against a cast iron disc. The density of the particles seems to be dependent of the temperature. The Authors reported a mean value of effective density of 0.75 ±0.2 g/cm^3, decreasing above the temperature of 110 °C. They emphasized that the effective density was approximately 3-5 times lower than the density of the bulk material, as consequence of porosity and shape characteristics. The main results are shown in Figure 5.5.

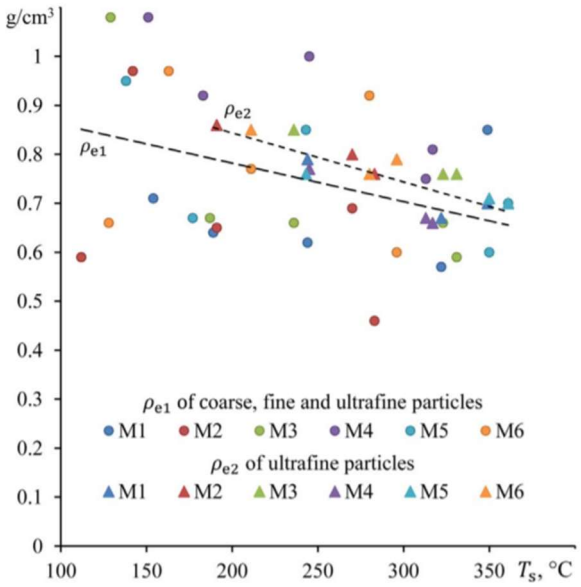

Figure 5.5: Effective density vs stationary temperature [100].

In another investigation, Nosko et al. [101] described a strong effect of the particles shape on the value of effective particle density. The Authors reported that particles emitted from brake materials sizing from 0.1 to 0.9 µm display 9 ±6% of porosity. Particles completely dense as well as particles featuring around 20% of porosity were also observed.

5.5.3 Morphology

Particles featuring different shapes were observed by Nosko et al. [101] from PoD tests with an LM material. Examples of rounded, flake, acicular and agglomerates particles collected during the investigation are given in Figure 5.6. The Authors reported that around 60% of particles are shaped like-flake, displaying a breadth-to-length aspect ratio of 0.7 ± 0.2.

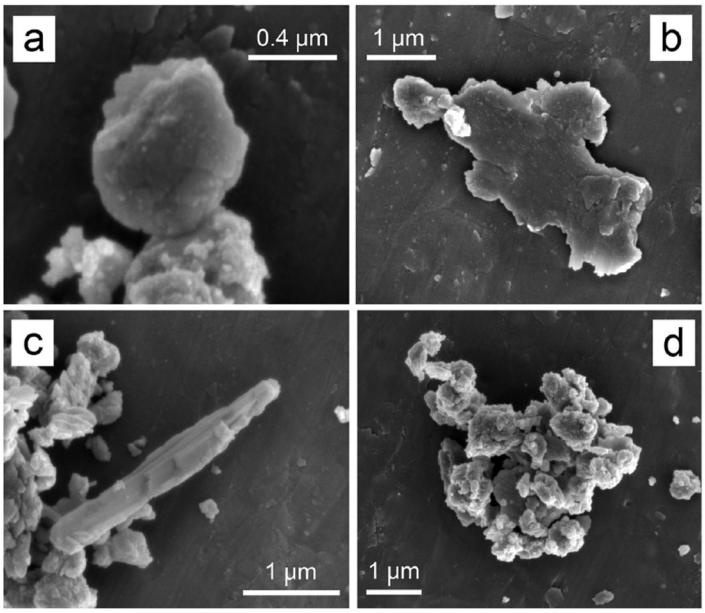

Figure 5.6: Examples of (a) rounded / angular; (b) flake; (c) acicular; (d) agglomerated particles collected from PoD tests [101].

In fact, flake is the shape mainly described on the literature for airborne particles from brake systems. Wahlström et al. [93], by PoD tests with LM and NAO friction materials, observed mostly coarse particles shaped as flakes. The Authors linked this particular shape to some mechanical generation. Figure 5.7 shows particles collected in this investigation.

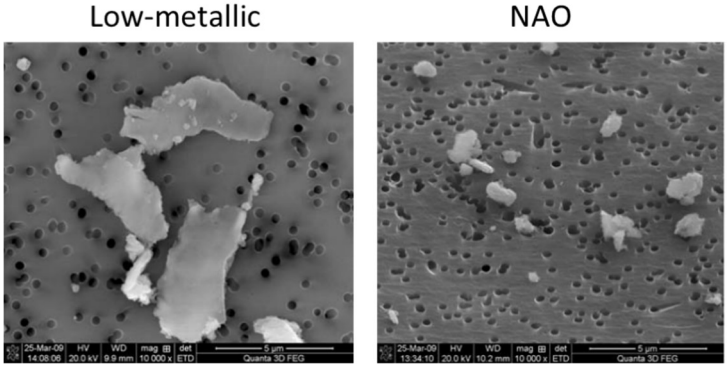

Figure 5.7: Particles collected from PoD tests with low-metallic and NAO friction materials [93].

Particles consisting in agglomeration of smaller grains are also often reported, especially in the fine fraction. The porosity observed by Nosko et al. [101] and discussed in the previous section is the result of cluster formation. Peikertovà et al. [102] by TEM analysis, observed larger agglomerate with smaller crystalline particles, as shown in Figure 5.8.

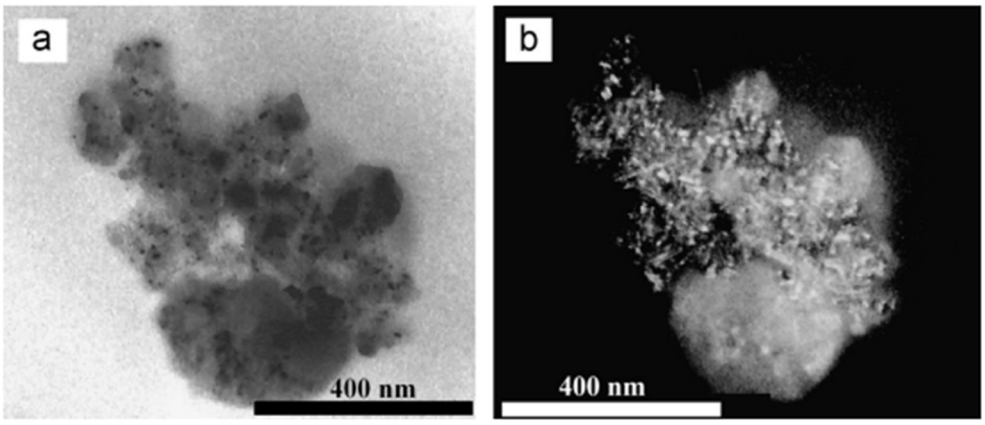

Figure 5.8: TEM bright (a) and dark (b) field image of agglomerate detected in the filtered sample of water suspended particles from dynamometer tests [102].

5.5.4 Composition

Of course, the composition of brake emissions depends on the elements present in the disc and pads. However, the chemical composition of these particles may differ from the bulk composition due to the physical-chemical transformations occurring during the sliding friction contact, such as oxidation, volatilization and condensation.

Coarse and fine particles are mainly composed by iron oxides. In addition, elements from the friction material, in lower relative amount, are usually detected in these particles. Sanders et al. [81] estimated that around 60% of wear debris comes from the disc, based on the composition of the particles collected during the tests. Figure 5.9 shows the main elements detected in this investigation, with iron, silicon, copper and barium displaying higher concentration. The term “hardware” in the Figure 5.9 is used to indicate “non-airborne particles”.

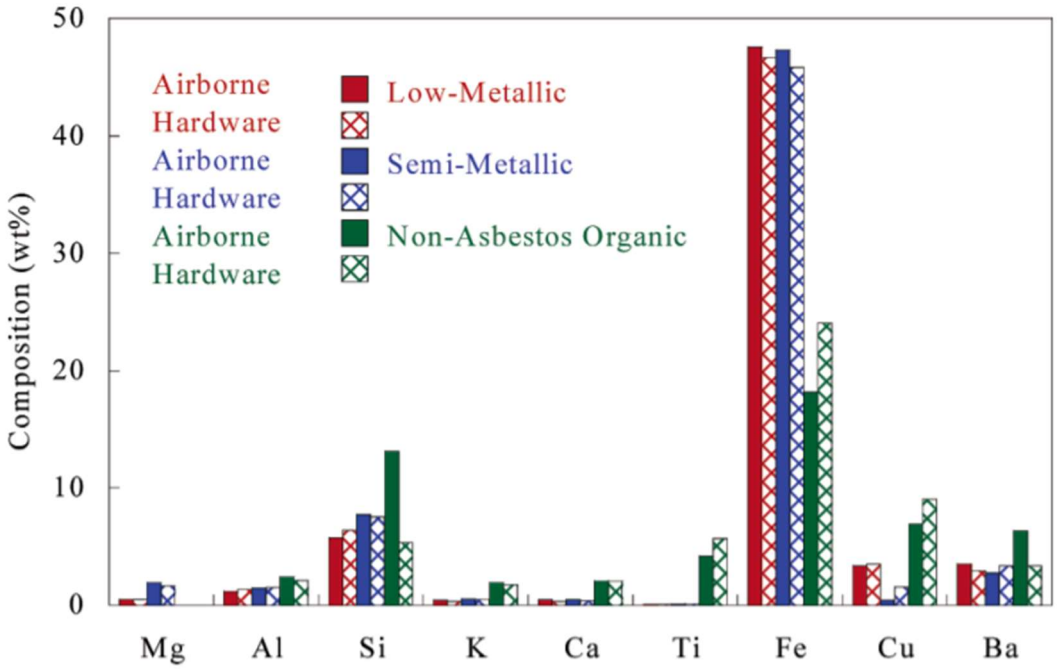

Figure 5.9: Elemental composition of PM emissions from LM, SM and NAO friction materials [81]. The term “hardware” is used to indicate “non-airborne particles”.

As discussed in the previous section, particles formed by agglomerates are usually found in brake emissions. In these case, small particles composed by different elements from disc and pad are held together forming a cluster particle. An example is shown in Figure 5.10, where very small particles of iron oxides (probably from the disc) and compounds from the friction material, such as barite and alumina, can be coalesce on one single particle.

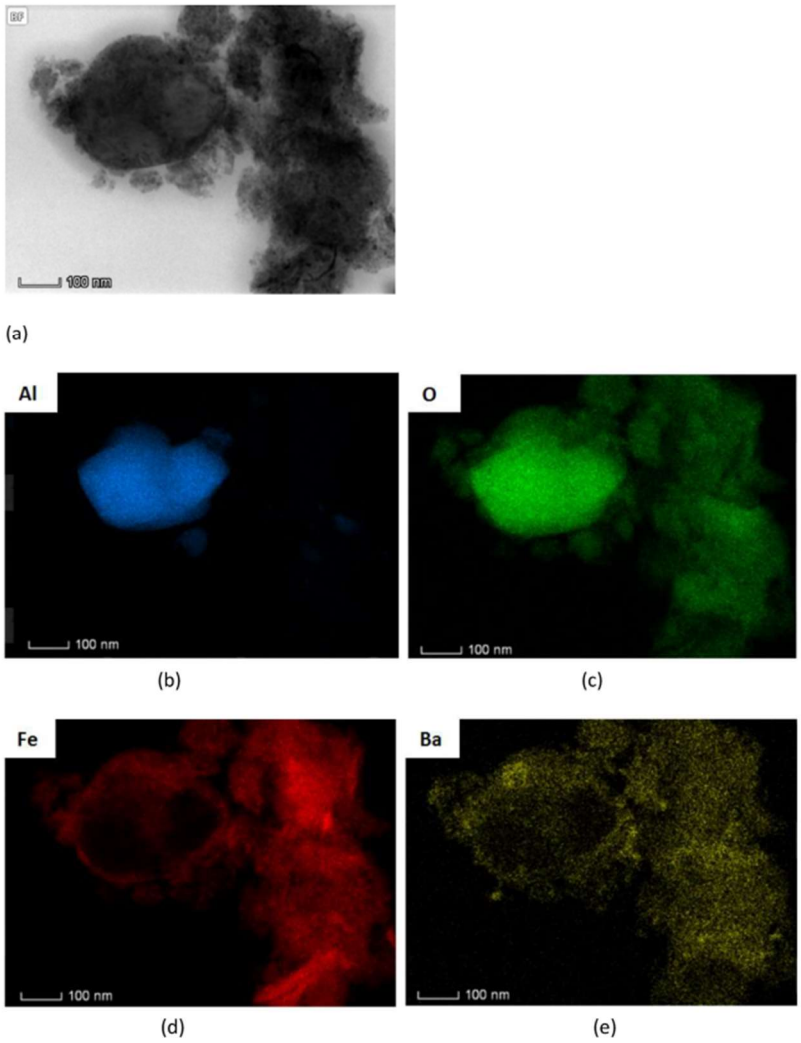

Figure 5.10: (a) TEM micrograph of an agglomerate from PoD tests. EDXS maps of specific elements are provided: (b) aluminum, (c) oxygen, (d) iron, and (e) barium [26].

Ultrafine particles are mainly composed by carbon and its compounds [102, 103]. This agrees with the described main mechanism of formation of this kind of particles: evaporation and condensation of organic components from the friction material matrix. Kukutschovà et al. [97] analyzed nanosized particles of wear debris, collected from dynamometer tests with a LM friction material. They found amorphous carbon and iron oxides as the main components.

Menapace et al. [104] investigated the effect of different disc compositions on the emissions; by dynamometer tests with commercial friction material pressed against cast iron and a WC-CoCr coated discs. Regarding the composition of the emissions, iron oxides were the main constituents when the cast iron disc was used. Instead, elements from the friction material were predominant in the emissions from coated disc tests, as shown in Figure 5.11.

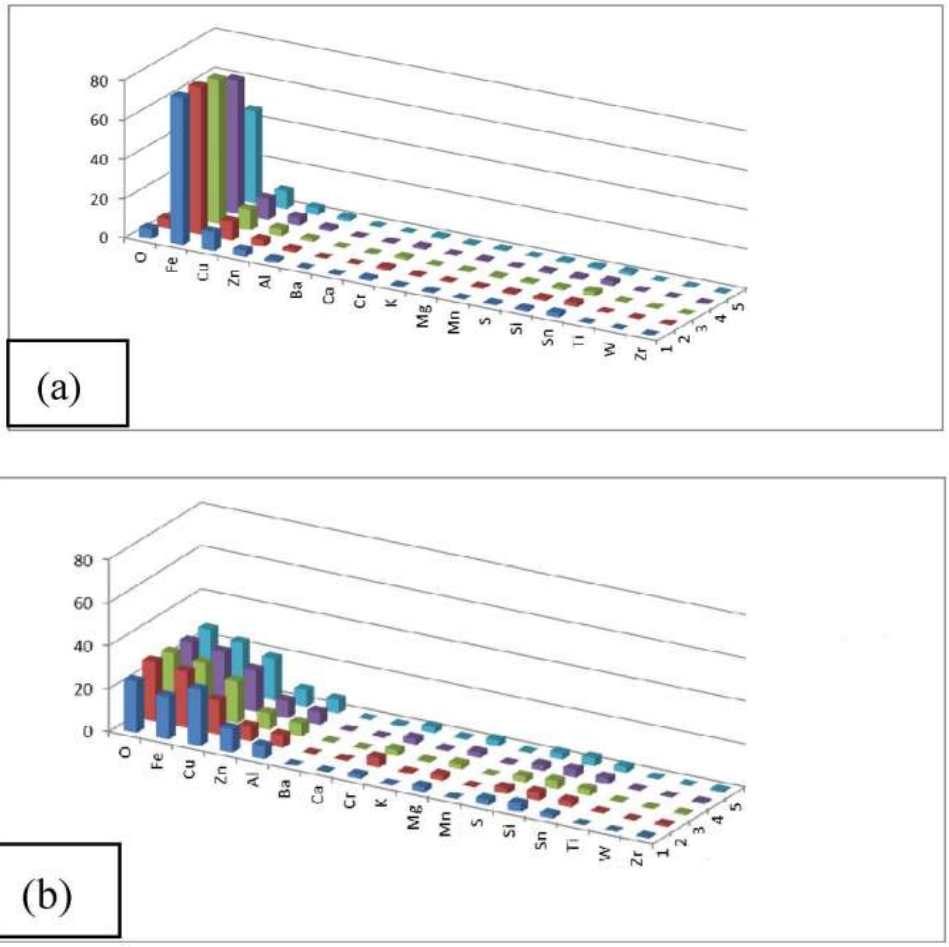

Figure 5.11: Elemental composition of PM emissions from a commercial pad against a (a) cast iron disc and against a (b) WC-CoCr coated disc [104].

5.6 Parameters affecting the PM brake emissions

While a detailed understanding of the aspects affecting the brake emissions is highly complex, it is possible to develop a broad knowledge comprising the most important issues. Vehicle weight, braking conditions and type of brake pads are regarded as the main influencing parameters. However, since such parameters are mostly determined by laboratory tests, some degree of uncertainty remains as concerns the effective influence in the real-world driving. Even if driving tests are performed, limitations in all simulated braking scenarios as well as complexity in isolating one single parameter persist. Nevertheless, investigations addressed to understand these parameters are discussed in the following.

5.6.1 Vehicle weight

As discussed in section 2.3, the mass of the vehicle is directly proportional to the amount of kinetic energy to be transformed during the braking. The vehicle weight is one of the factors contributing to total brake wear. In case of the airborne particles, the behavior seems to be the same [105, 106]. According to an investigation conducted by Garg et al. [107] using seven pad formulations, the brakes of large cars emit 55% more PM10 and PM2.5 than small cars. Similar results are reported by Luekewille et al. [108], in a comparison between light duty trucks (including vans, pick-up trucks and SUVs) and passenger cars. It is estimated that PM10 brake emissions vehicle-km increase around 0.004-0.005 mg per kg of vehicle weight [106].

5.6.2 Braking conditions

Several studies using PoD tribometer were conducted to investigate the effect of pressure on the amount of brake emissions. One of them carried out by Alemani et al. [109], tested a LM friction material under pressure varying from 0.29 MPa to 1.95 MPa. An increasing amount of the emissions with corresponding increase of contact pressures was observed. However, the Authors attributed this effect to the temperature induced by the higher pressures. In an investigation conducted by Mosleh et al. [92], NAO and LM materials were tested under pressures varying between 0.125 and 1.25 MPa. In this case, the effect on the emissions was observed only for particles size from 2 and 15 μm, thus excluding the influence on the smaller fraction. On the other hand, Wahlström et al. [110] reported a significant increase with the PoD applied pressure in the concentration of particles smaller than 2.5 μm.

The role of pressure on the emissions was also investigated using dynamometer tests. Mamakos et al. [111] applied the World-harmonized Light duty Test Cycle (WLTC), followed by some selected modes of the AK Master procedure, with three LM and one NAO materials. The Authors reported elevated particle number emissions and systematic formation of nano-sized particles when higher pressures were applied.

Regarding the speed, in an experiment conducted by Namgung et al. [112], an increment by around one order of magnitude on the total amount of emitted particles is reported when the speed rises from 25 km/h to 50 km/h. Olofsson et al. [113] conducted an investigation using two different instruments capable to measure the emissions in distinct size intervals. The Authors show that as the sliding velocity increases, wear rate increases

too together with the related emission rate of airborne particles. This effect was more significant for sliding speeds above 1 m/s, as shown in Figure 5.12, for both instruments.

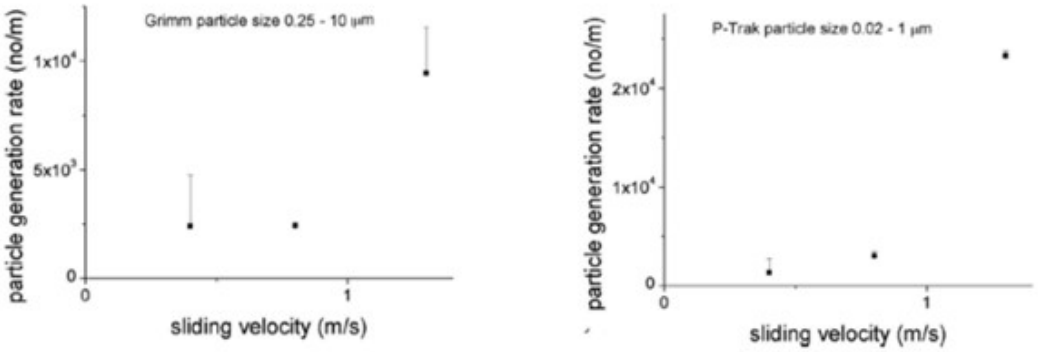

Figure 5.12: Particle generation rate in function of the sliding velocity, measured by Grimm and T-trak instruments [113].

Alemani et al. [114], describe the friction power as the most important brake parameter affecting the emissions. The Authors define the friction power (P) as function of the friction coefficient (μ), normal load (N) and sliding speed (v), by the equation P=μNv. Nevertheless, the increase of the sliding speed is accompanied by an increase in the emissions even when the nominal contact pressure is decreased.

Temperature too is dependent on the aforementioned braking parameters through their relationship with the friction power. A significant increase in the emissions is known to be determined by the achievement of the critical temperature, i.e., a temperature related to the decomposition temperature of the organic matrix. The ultrafine particle fraction seems to be the most sensitive to the achievement of such decomposition stage by [97, 114]. The chart of Figure 5.13 clearly shown this effect [114].

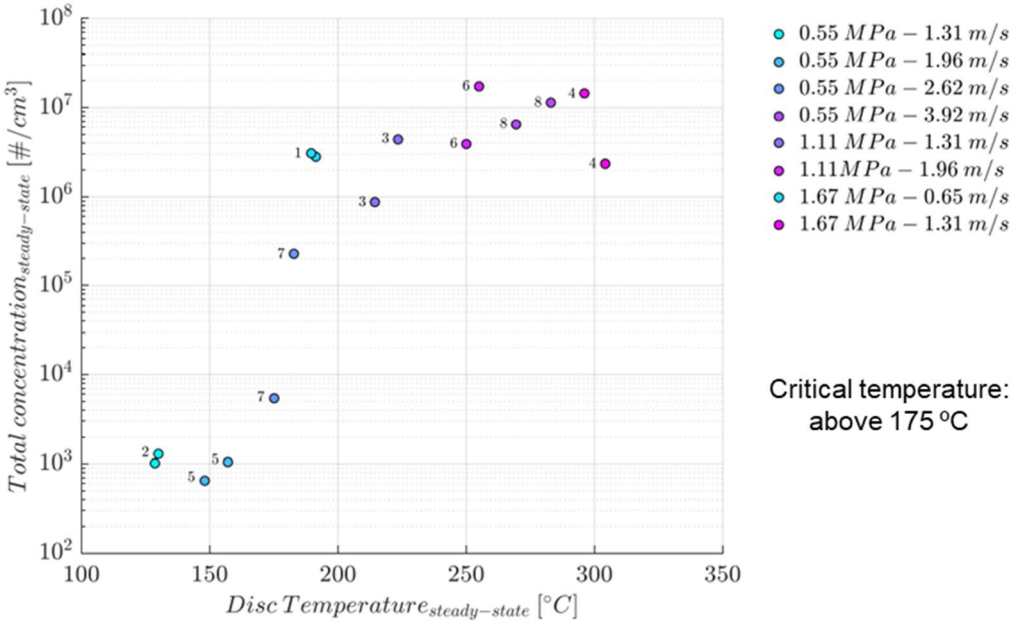

Figure 5.13: Number concentration of emitted particles vs disc temperature at steady state [126].

5.6.3 Type of pad friction material

LM and SM friction materials feature different behavior than NAO materials in terms of formation and release of airborne particles. Sanders et al. [81] by dynamometer tests observed that LM emits 3-4 times more than NAO. Similar results were found by Gramstat et al. [115], describing higher amount of emissions from LM compared to NAO even under severe brake conditions. Perricone et al. [116] ranked the pad-disc combinations, testing five different pad materials against cast iron disc. This ranking revealed that NAO have the lowest emission in terms of mass, but the highest emission with respect to particle numbers. LM displays higher emissions with respect to mass, and lower ones with respect to particle number.

Five times higher emissions from LM compared to NAO was also reported by Park et al. [75], which attributes the results to the particular surface topography of each material. In fact, as discussed in section 4.3 and shown in Figure 5.14, the contact plateaus on LM are placed at discrete areas, separated by lowlands. As consequence, a high stress is concentrated on the plateaus, producing a larger amount of wear particles. Furthermore, the lowlands act as reservoirs to retain these wear particles for resuspension during driving.

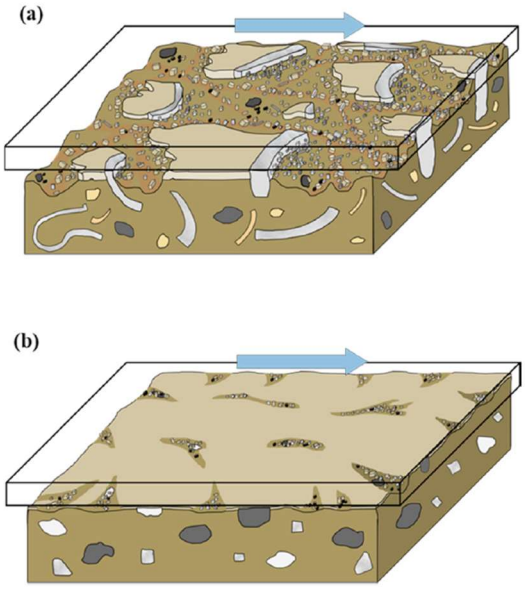

Figure 5.14: Schematic surface topography of (a) LM material and (b) NAO material [75].

Park et al. [75] also reported a higher relative content of iron in the emissions from LM compared to NAO friction material. Due to the high abrasive content in LM materials, larger disc wear is generated.

5.6.4 Bedding

Matějka et al. [117] compared the emissions from brand new LM pads and used ones, by dynamometer tests. The results show a significantly higher emission when new pads are used. They explained the results for new pads in terms of wear phenomenon determined by a dominant abrasive wear. According to the Authors, after some braking events, the contact surfaces became smoother and the adhesive wear takes place, leading a reduction and stabilization of the emissions. Figure 5.15 shows the total number of particles as a function of the cycles, being the T-1xP2 the first cycle, i.e., using new pads.

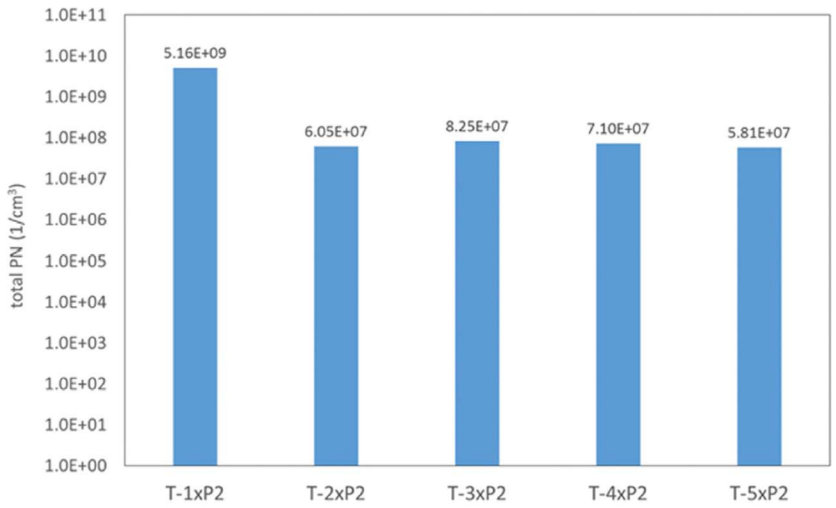

Figure 5.15: Particle number concentration emitted in function of cycles test [117].

Applying the World-harmonized Light duty Test Cycle (WLTC) with a dynamometer, Hesse et al. [118] investigated the effects of the bedding procedure on brake emissions. They observed a peak of number-related emissions during the first stages of braking and then a significant reduction. In addition, the Authors reported that the number of braking events necessary to complete the bedding is fully dependent on the type of pad materials. Park et al. [75] indicated that number concentration of particles from NAO materials decreases faster than LM, i.e., the number of braking necessary to complete the bedding in case of NAO materials is lower than LM.

Chapter 6

Methodology

6.1 Characterization protocol

A characterization protocol was established during this thesis aiming at studying the mechanisms producing the PM emissions. Based on the techniques available and on the characteristics of the samples to be analyzed, a comparative investigation, using SEM-EDXS techniques, between the elemental composition of the virgin friction materials, the secondary plateaus formed on the pin's worn surfaces and the airborne particles emitted and collected during the tribological tests was performed. Figure 6.1 shows the scheme of such characterization protocol.

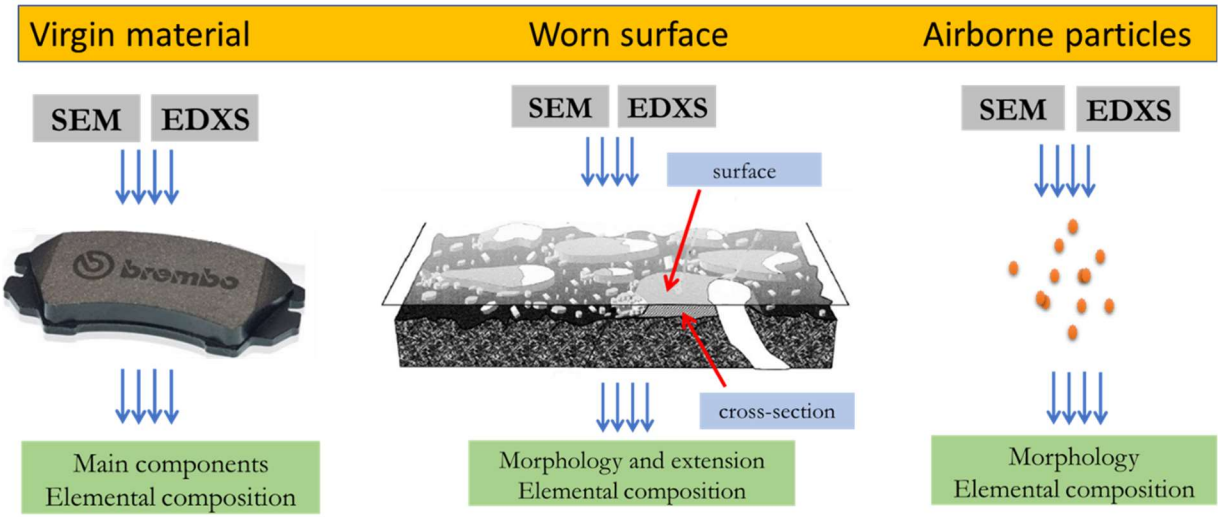

Figure 6.1: Scheme of the characterization protocol used for the investigations.

6.2 Materials

6.2.1 Commercial friction materials

For the investigations described in Chapters 7 and 8, low-metallic commercial friction materials were used. The pins were extracted from these commercial pads with a diameter of 10.0 mm and height of around 16 mm.

Since the characterization of the virgin materials is part of the characterization protocol, the reader is referred to the first part of each chapter dedicated to the respective results (Chapters 7 and 8).

6.2.2 Non-commercial friction materials

For the investigation described in Chapter 9, low-metallic non-commercial friction materials were tested. In this case, three different compositions were produced, with the manufacturing of the pins performed in the laboratory, according to the following description.

6.2.2.1 Preparation of the rice husk

The rice husk (RH) is a natural agro-waste residue containing a relative high amount of silica, which may display interesting properties to be used as an ingredient in brake friction material. In this study, the RH in two different conditions was added to the friction material compositions: one just grinded; and another grinded plus heat treated. The purpose of the griding is to facilitate the mixing of RH with the other ingredients of the friction material. The heat treatment is performed aiming to reduce the organic fraction of the RH, since its degradation, occurring is service, might be problematic during the brake application. Figure 6.2(a) shows the morphology of the neat RH, as received from Brazil. The RH was first submitted to the griding process, for 20 minutes in air. A 3D Turbula mixer with tungsten carbide vial and balls was used for the griding operation. As a result of this process, an average particle size lower than 350 μm was obtained. After grinded, RH was dried up in an oven at 105°C for 2h in air, thus obtaining the removal of any residual moisture. The morphology of the RH after grinding is shown in Figure 6.2(b). Following specific literature indications [119-121], part of the RH was also heat treated at 600 ºC for 2h in air. Figure 6.2(c) shows the RH after the heat treatment, featuring particle sizing around 100-150 μm. In this latter condition, RH exhibits a porous and cracked microstructure, as shown in Figure 6.2(d).

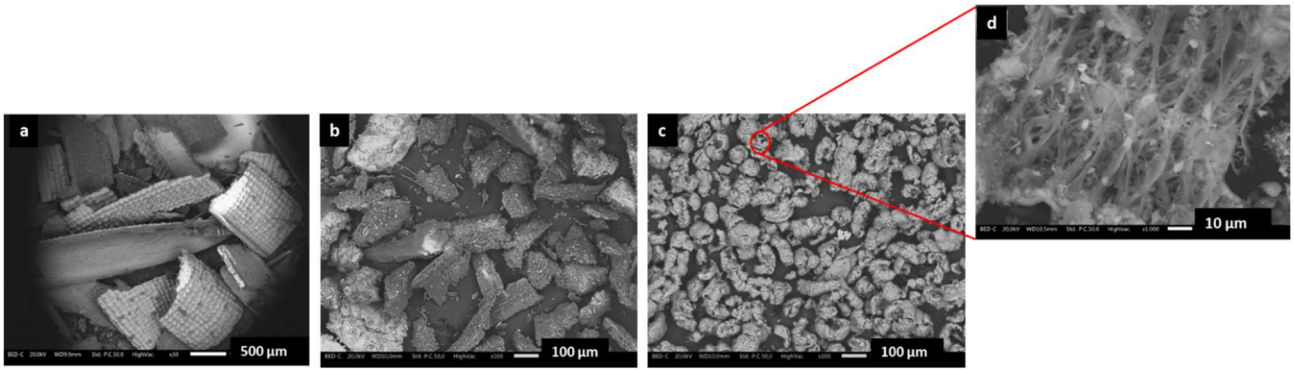

Figure 6.2: SEM observations of the rice husk (a) as received, (b) after griding and (c) after grinding and heat treatment at 600°C. A porous, cracked microstructure of the rice husk treated at 600°C is highlighted in (d).

In order to verify the proper heat treatment parameters, a thermogravimetric analysis (Tg) was carried out on the grinded RH, and the result is shown in Figure 6.3. It is possible to observe a significant loss of weight until 500 ºC, attributed to degradation of organic fraction. After this temperature, remains the inorganic content of the rice husk, basically composed by silica in a percentage at around 20 wt.% [119].

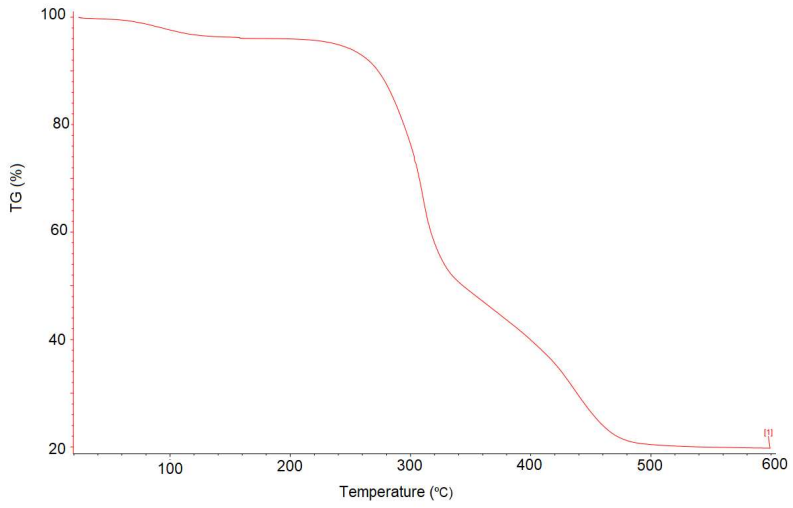

Figure 6.3: Thermogravimetric analysis performed on the RH.

The elemental composition of the RH after grinding and after heat treatment are given in Table 6.1. As expected, a significant reduction in the carbon content of the RH can be appreciated as the result of the heat treatment, with a consequent relative increase in the silicon (and silica, as a result) content.

Table 6.1: Elemental composition of the rice husk after grinding and after heat treatment, obtained by EDXS analysis.

Element	RH grinded (wt.%)	RH grinded plus heat treated (wt.%)
C	33.2 ± 1.1	4.2 ± 0.8
O	49.4 ± 1.3	50.3 ± 4.1
Si	17.4 ± 1.5	46.5 ± 3.8

Figure 6.4 shows the XRD patterns of RH samples after grinding and after grinding plus heat treatment. Figure 6.4(a) shows a broad diffuse halo with some peaks due to coherent scattering. The main crystalline structure has been identified as cellulose. In the diffraction pattern, the Miller indexes of this phase are indicated. The RH XRD pattern after grinding plus heat treatment is shown in Figure 6.4(b), in which a fully amorphous structure can be inferred from the diffuse halo, that is the main and only feature of the XRD pattern. As previously indicated by the compositional data in Table 6.1, in this material silicon oxide is the main compound of RH, possibly with a minor concentration of carbon, which has been mostly eliminated by the heat treatment.

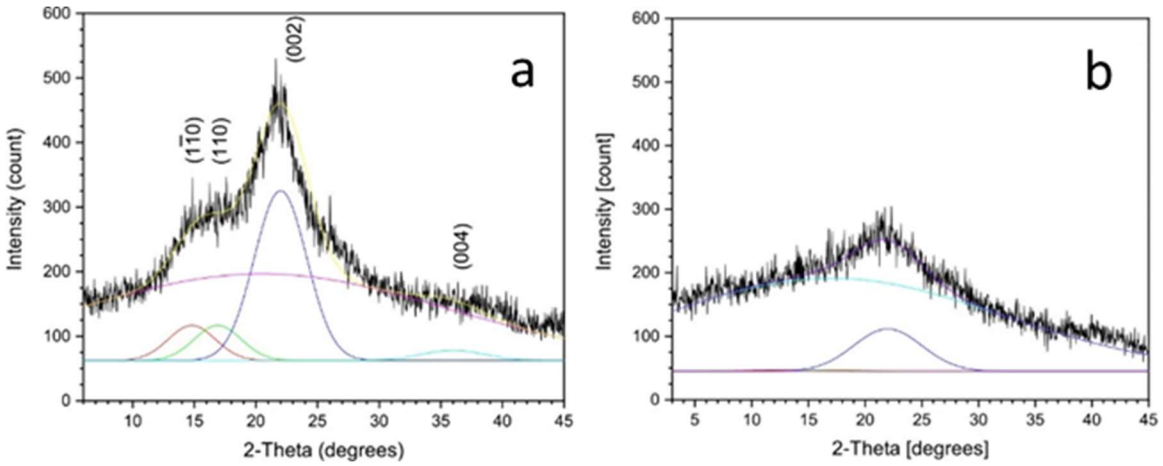

Figure 6.4: XRD patterns of the (a) grinded and (b) grinded plus heat treated RH samples.

6.2.2.2 Pins production

The compositions of the three friction materials investigated are given in Table 6.2. Two formulations contain 6 wt.% of RH: one after grinding, codenamed F-RH, and the other after grinding and heat treatment, called F-RHT. The third formulation contains alumina in

the place of RH, still with a 6wt. % concentration (F-AL). This benchmark formulation with alumina was used to compare the results with those of the two formulations containing RH.

Table 6.2: Friction material compositions.

		F-RH (wt%)	F-RHT (wt%)	F-AL (wt%)
Parental composition/ingredient	Fillers ($BaSO_4$ +$CaCO_3$)		57	
	Lubricant (Graphite)		7	
	Binder (Phenolic resin)		15	
	Fibers (Iron fibers)		15	
Variation in the composition	RH grinding	6	-	-
	RH grinding plus heat treatment	-	6	-
	Allumina	-	-	6

To produce the pins, all ingredients were mixed for 30 min using a 3D mixer Turbula. Cylindrical pins with 10 mm of diameter and 15 mm of height were prepared out of each mix using a cylindrical die placed in a hot-press for 10 min under a 14 MPa pressure. Finally, the specimens were post-cured in an oven with the similar cycle used for real brake pads: temperature = 200ºC and time = 4 h, followed by cooling down in room temperature. The mean values of density of the produced pins are given in Table 6.3.

Table 6.3: Density of produced pins.

Composition	Density (g/cm^3)
F-RH	2.0 ±0.3
F-RHT	2.5 ±0.1
F-AL	2.3 ±0.1

The elemental composition of the friction materials is provided on the first part of the Chapter 9, dedicated to the results.

6.2.3 Counterface disc

The discs used in all investigations were made of pearlitic grey cast iron. The microstructure of the discs, obtained through an optical microscope, is reveled in Figure 6.5, showing graphite flakes in a pearlitic matrix. Its elemental composition, analyzed by means of EDXS, is reported in Table 6.4. By an ENCO-TEST M4U 025 durometer a hardness of 216 HV30 was measured in the disc surface.

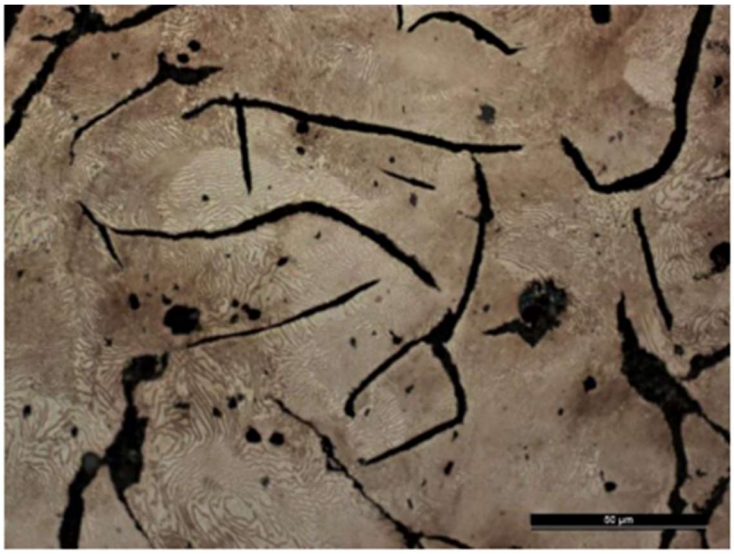

Figure 6.5: Microstructure of the disc, after 2% Nital etching.

Table 6.4: Elemental composition of the disc.

Element	wt.%
C	6.6
Si	1.4
Cr	0.3
Mn	0.4
Fe	91.1
Sn	4.0

The dimensions of the discs used are specified in Figure 6.6.

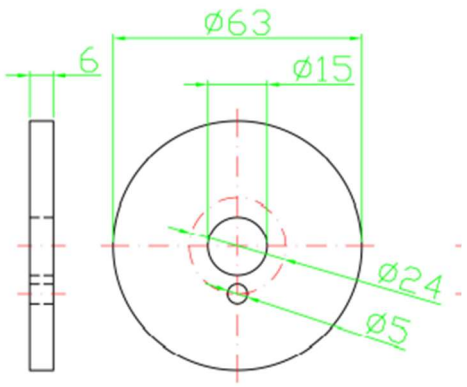

Figure 6.6: Dimensions of the disc used in the tests.

6.3 Testing set-up

The tribological tests were performed using a laboratory pin-on-disc (PoD) tribometer. In this kind of equipment, the pin is kept stationary and pressed against the rotating surface of the disc through a normal load, as schematized in Figure 6.7. This test procedure implies the sliding of the disc under drag conditions (the angular velocity of the disc is kept constant).

The PoD configuration is not designed aiming to simulate the real brake system action, for which specific types of equipment, such as dyno-bench tests are used; but rather useful for investigating fundamental tribological mechanisms acting during the sliding, which match with the specific objective of this thesis [49, 122,123].

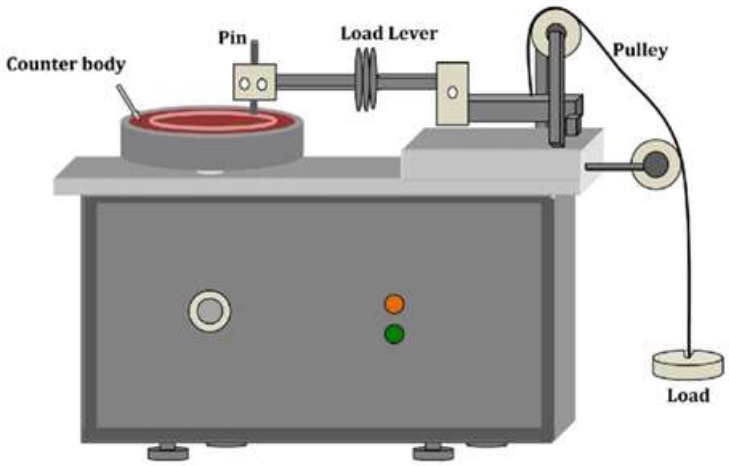

Figure 6.7: Schematic representation of a PoD tribometer.

A nominal contact pressure of 1 MPa and a constant sliding velocity of 1.51 m/s were used in all PoD tests. These parameters correspond to mild sliding conditions resembling those faced in real braking. Dry sliding tests were carried out at room temperature using a Ducom PoD machine for 5400 s. A preliminary running-in of 1800 s to provide a conformal contact between the pin and the disc surface was conducted. The dynamic friction coefficient was continuously recorded during the tests.

Using an analytical balance, with a sensitivity of 10^{-4} g, the weight of pins was measured before and after each PoD test. From these values, the specific wear coefficient, K_a, was calculated, as given below:

$$K_a = V/Fd \tag{6.1}$$

where V is the volume loss (m^3), F is the applied normal load (N), and d is the sliding distance (m). The volume loss was determined by measuring the weight of pins before and after each test and considering the bulk density of the materials.

The tribometer is equipped with an enclosure, especially designed for investigating both the tribological properties as well as the airborne particles generated from tribological tests. A scheme of the test apparatus is shown in Figure 6.8. This test equipment has been previously used in other study of the present research team [26] and it is based on a design developed by Olofsson et al. [70, 113]. The ambient air (A), pumped by a fan (B), passes through a HEPA filter (C), which ensures a clean air flow entering in the chamber (D). The

fan was set at a flow rate at around 10 m/s and before each test the cleanliness of the air flow inside the chamber was verified by measuring the background concentration of airborne particles. A TSI® Optical Particle Sizer (OPS) model 3330 connected to the chamber (G) measured the particle number concentration from particle size 0.3 μm up to 10 μm divided over 16 channels. A sampling rate of 1 Hz was set for measuring the concentration of airborne particles emitted during the PoD tests. Using a Dekati® PM_{10} impactor connected to the chamber (F), the particles were also collected on aluminum foils for a successive characterization in two size range: from 10 to 2.5 μm and from 2.5 to 1 μm.

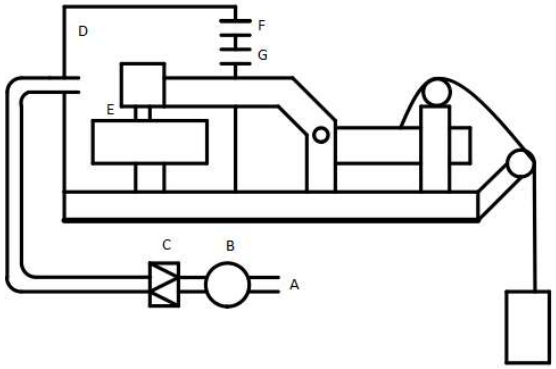

Figure 6.8: Schematic of test equipment. Room air (A), fan (B), filter (C), air inside the chamber (D), rotating disc sample (E), air outlet to the OPS (G), air outlet to impactor PM_{10} (F).

Figure 6.9 shows the apparatus used for PoD tests. In Figure 6.9(a) the Dekati® PM_{10} impactor (on the left) and the TSI® Optical Particle Sizer (on the right) are shown. The enclosed chamber, used to isolate the region of contact pin/disc and thus enable the measurement and collection of airborne particles emitted from the contact, is given in Figure 6.9(b). Figure 6.9(c) depict an overview of the apparatus.

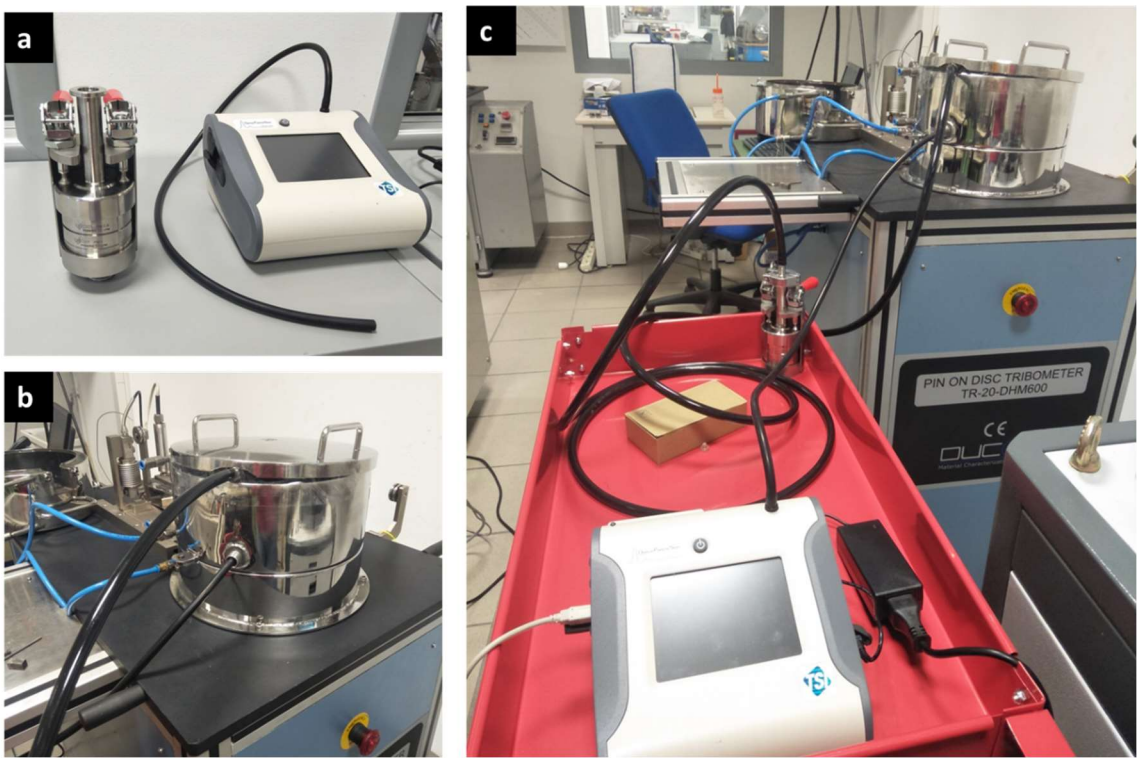

Figure 6.9: Testing apparatus. (a) Dekati® PM_{10} impactor (on the left) and the TSI® Optical Particle Sizer (on the right). (b) Chamber used to isolate the pin/disc contact environment. (c) Overview of the test apparatus.

Optical Particle Sizer: it measures the number concentration of particles in the inlet air, according to their aerodynamic size in 16 different channels ranging from 0.3 to 10 μm. The working principle of the instrumentation is based on light scattering, as shown in Figure 6.10. A pump allows the entrance of a sampling flow rate of 1 l/min with an additional flow rate of 1 l/min used to prevent the optic system contamination. The sampling flow passes through the optic chamber and each particle is invested from a laser beam. Part of the laser beam is scattered on a U-shaped mirror that directs and reflects the scattered beam on a photo detector able to count the number of particles and their size. In the end the sampling, the flow passes through a series of filters and the flow separates in two parts, one goes to the exhaust part (1 l/min) and the remaining amount will be reused as sheath air flow (1 l/min) to avoid optic contamination.

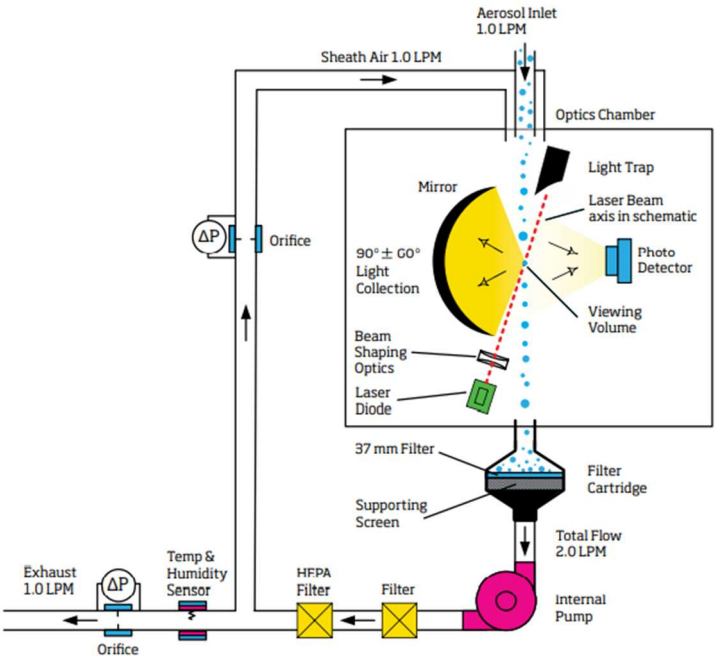

Figure 6.10: Working principle of the Optical Particle Sizer.

Impactor PM10: a three-stage cascade impactor. For the investigations conducted in this thesis, it was used to collect the airborne particles, divided into two range of size: from 10 to 2.5 μm and from 2.5 to 1 μm. To allow a correct feeding of the sampling flow rate to the impactor, the latter is assembled with an external pump set on a nominal air flow rate of 9.8 l/min. The particles are collected in circular aluminum foils with a specific grease on it to allow particle's sticking. The working principle is based on the particle inertia, which is directly proportional to its size. As schematized in Figure 6.11, the sampling flow passes through the first specially pierced plate that directs the flow on the greased filter. The larger particles, with the larger inertia, are not able to deviate their direction and get stuck on the filter. Instead, smaller particles thanks to their smaller inertia can deviate from the filter and passes laterally to it and are conveyed on the next pierced plate, and so on for the following filters.

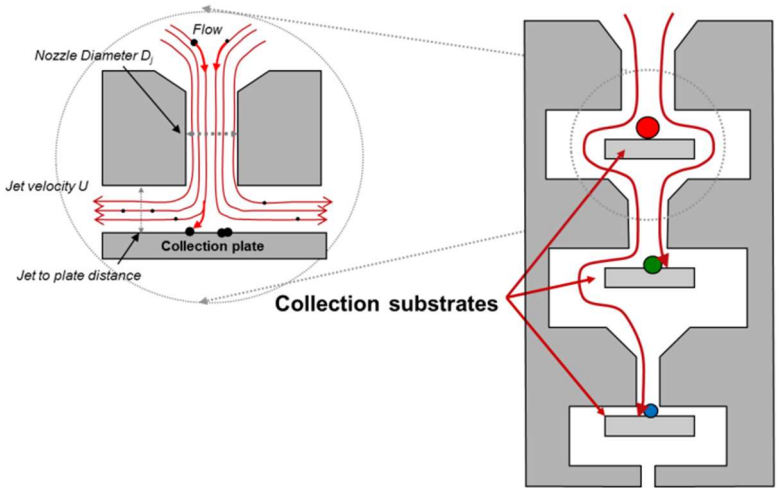

Figure 6.11: Work principle of the Impactor PM10.

6.4 Characterization methods and instruments

6.4.1 Scanning Electron Microscopy (SEM) and Energy Dispersive X-Ray Spectroscopy (EDXS)

Scanning electron microscope (SEM) and energy dispersive X-Ray spectroscopy (EDXS) were used to analyze and characterize the virgin friction materials, the worn surfaces of pins and the emitted PM. The experimental apparatus used during this research is a JEOL IT300 equipped with the EDXS probe. These techniques allow surface analysis. SEM micrographs can be acquired using both secondary and back-scattered electron (SE and BSE, respectively) so to have a topographic and phase contrast.

EDXS gives compositional information by detecting the X-rays radiation produced by the different elements present on the analyzed area. All EDXS analysis are given as mean value of three measurements, considering a representative area of the samples.

For the worn surface's observations, both top view and cross-section analysis were carried out. The top view observation did not require any preparation, and it was mainly focused on evaluating the extension and compaction of the secondary plateaus. Cross-sections of the pins have been prepared by cutting the samples, embedded in a cold mounting resin and metallographic prepared. The particles emission collected on the aluminum foils during the tests were transferred to an acetate film to avoid the interference of the substrate on the elemental composition measurements. For the characterization protocol described in Section 6.1, the carbon was not considered on the EDXS analysis.

6.4.2 X-ray diffraction (XRD)

The crystalline phases and their composition in the rice husk (grinded and heat treated) were identified using X-ray diffraction (XRD) measurements, carried out with an Italstructures IPD3000 instrument equipped with a Co anode source (line focus) operating at 40 kV and 30 mA. Diffraction spectra were acquired in reflection geometry by means of an Inel CPS120 detector over 5-120° 2-theta range (0.03 degrees per channel). The phase identification has been conducted using a full pattern search match software, FPSM [124], based on a Rietveld algorithm.

X-rays consist of a wide spectrum of extremely penetrating electromagnetic radiation, characterized by wavelengths in between 10 nm and 0.01 nm. When an X-ray beam hits a crystalline solid, the single atom vibrates, emitting electromagnetic radiation of a certain wavelength in all directions. The waves interaction can produce constructive or destructive interference. The constructive interference occurs in specific directions when the X-rays are reflected by a family of parallel and equidistant crystalline planes, resulting in a reinforcement of the signal.

6.4.3 Thermogravimetric (TG) analysis

In order to verify the degradation temperature of the rice husk, thermogravimetric analysis on the material were carried out. The analyses were conducted using a Netzsch STA 409 Luxx thermal analyser with alumina sample holder. The heating rate was set to 10 °C/min in air flux. A small amount of material was heated up to 600°C. During the heating of the samples in the thermo-balance, if some degradation phenomena occur, the analyzer detected the relative mass variation.

Chapter 7

PM brake emissions from Cu-full and Cu-free friction materials

This chapter investigates the particulate matter (PM) emissions behavior and its relations with friction and wear aiming to identify the mechanism of generation the PM emissions. In order to better understand the relation between the tribological response and the PM emissions, the friction coefficient and the total concentration of emitted particles were simultaneously measured during the pin-on-disc (PoD) tests. Additionally, both collected particles and pin's worn surfaces were characterized in terms of its morphology and elemental composition, following the protocol described in Section 6.1. Furthermore, the characterization of the virgin friction materials was performed and compared to the further results.

A copper-containing and copper-free commercial friction materials were used in this investigation. As discussed in Section 3.4.2, several efforts have been made over the last years to remove toxics components on the friction material formulations, since they can become hazardous emissions and causing adverse health effects. The new developed Cu-free formulations might effectively respond both performance and low emissions requirements.

The effect of the *scorching treatment*, commonly used on brake pads before their usage, was also investigated. For that, tests were carried out in both scorched surface and bulk material, as schematized in Figure 7.1. The scorching treatment consists in expose the surface of new pads to high temperature (usually around 650 °C) for a period ranging from 15 s to a few minutes, depending on material composition. This treatment aims at promoting the mutual adaption of pad/disc from the fist braking, facilitating the formation of the friction layer and improving the friction performance.

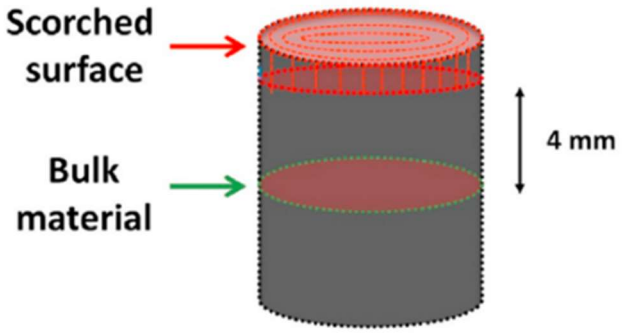

Figure 7.1: Scheme of the tested sample conditions: scorched surface and bulk conditions, using a surface cut through the bulk unaltered material, far from the scorched surface [125].

Part of the results discussed in this chapter were published in [125].

7.1 Characterization of the friction materials

The two commercial low-metallic friction materials investigated, 'Cu-full' and 'Cu-free', differ for their copper-content, as indicated in Table 7.1. Figures 7.2 and 7.3 show the surface microstructure (SEM micrographs) a relevant X-ray maps, acquired using EDXS for both materials. The main identified constituents are indicated. The two materials display similar microstructures, featuring coarser graphite and silicates particles dispersed into a matrix containing also finer grains of other ingredients, such as fibers and abrasives (alumina, zinc). In Cu-full material (Fig. 7.2) the presence of copper fibers can be appreciated; in general, larger than iron fibers.

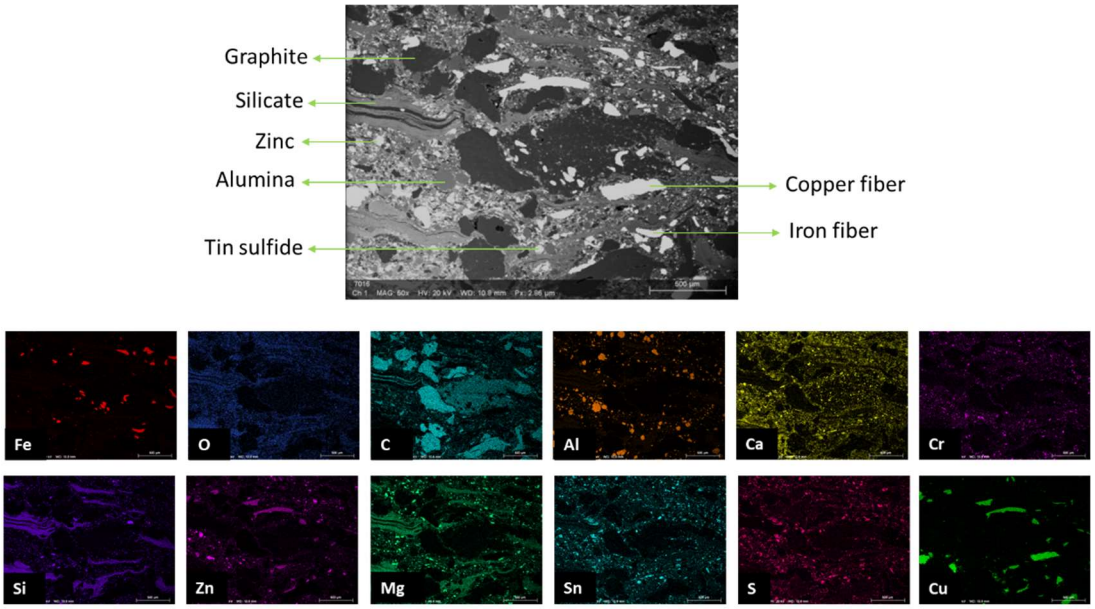

Figure 7.2: SEM/EDXS analysis of Cu-full material, with the identification of main constituents.

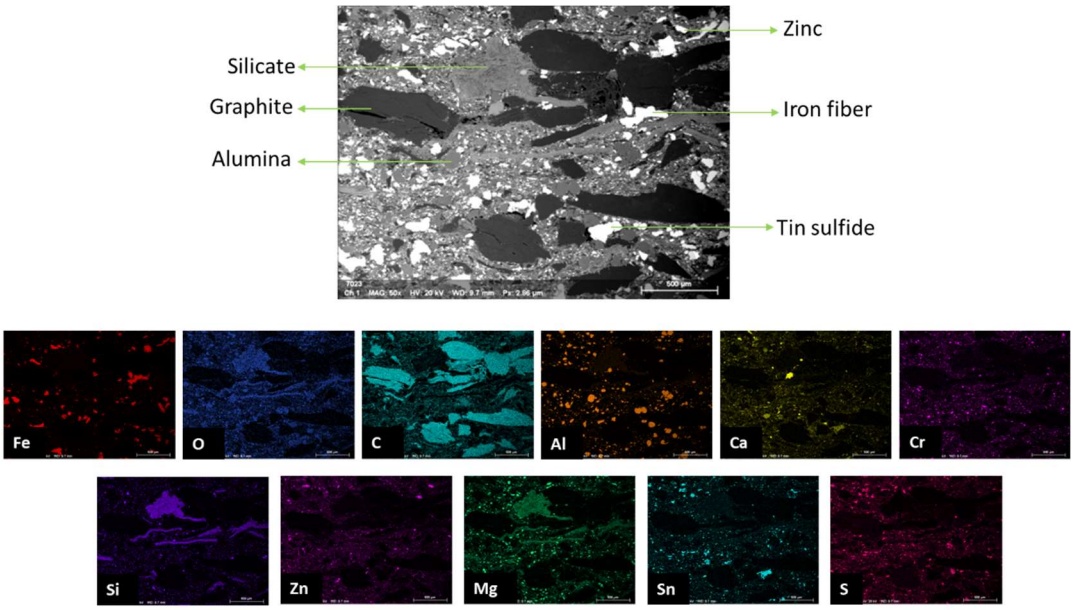

Figure 7.3: SEM/EDXS analysis of Cu-free material, with the identification of main constituents.

The elemental composition of both friction materials is given in Table 7.1. The two materials feature compositions qualitatively similar, with some exceptions, as concerns for instance the 12 wt.% of copper in Cu-full material, replaced by iron in case of Cu-free.

Table 7.1: Elemental composition of Cu-full and Cu-free materials. Carbon not quantified.

Element wt.%	Cu-full	Cu-free
Fe	12.4 ±1.5	25.6 ±1.3
Mg	8.4 ±0.9	7.8 ±0.5
Zn	9.0 ±0.3	8.2 ±0.5
Al	6.0 ±0.4	6.0 ±0.2
Si	3.8 ±0.8	3.0 ±0.1
S	4.1 ±0.2	4.9 ±0.3
Cu	12.1 ±2.1	-
Sn	7.0 ±0.6	4.8 ±0.5
Ca	3.6 ±0.3	2.1 ±0.2
Cr	1.6 ±0.1	1.8 ±0.3
O	32.0 ±0.8	35.8 ±1.1

The scorching treatment was carried out with a hotplate at around 650 ºC for a few seconds. The penetration depth of the scorching effect, investigated with an optical microscope, is shown in Figure 7.4, for both friction materials. In the Cu-full, a penetration of around 1800 µm is evidenced by the dark surface region, interpreted as mainly due to the organic compound degradation and formation of carbonaceous particles. A less marked dark region is noticed in Cu-free material. In this case, the heat affected zone is much more limited, as an indication of a lower degradation of the organic constituents. This result can be explained in terms of better thermal diffusivity promoted by copper [126]. Consequently, during the scorching, the surface heating in the Cu-full material is much more intense and able to deeper penetrate.

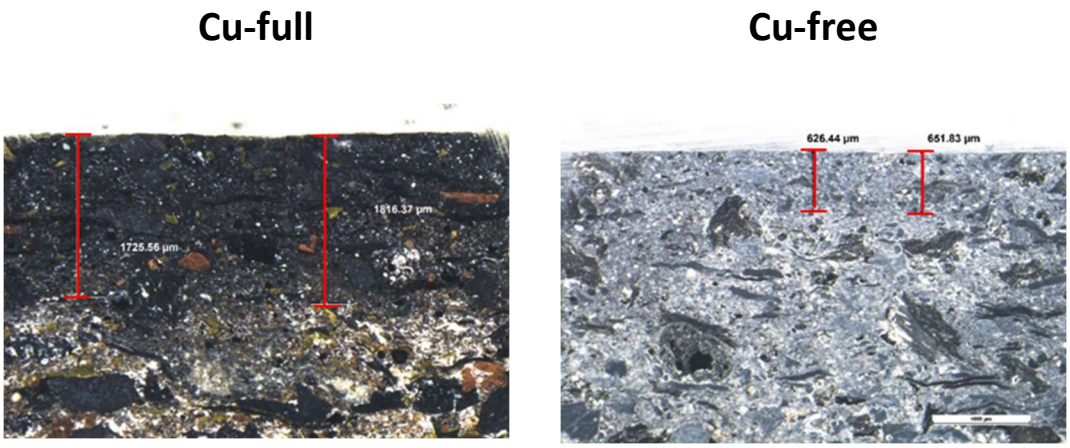

Figure 7.4: Optical microscope observation of the scorching penetration for Cu-full and Cu-free materials. The extension of the scorching penetration depths in the two materials is indicated [125].

7.2 Tribological and emissions behavior

Typically, the friction coefficient curves from PoD tests are characterized by two stages: the running-in and the steady-state. The running-in corresponds to the first stages of contact, during which the asperities on the virgin surfaces are removed, wear of both friction material and disc initiates, and the friction layer starts to be formed. Very often, the friction coefficient increases during the running-in until achieving a steady-state condition, not necessarily characterized by a constant value of the friction coefficient [66, 72]. Figure 7.5 shows the evolution of both friction coefficient and the total concentration of emissions from the PoD tests conducted on the Cu-full friction material, in scorched (Fig. 7.5a) and bulk (Fig. 7.5b) conditions. The material seems to achieve the steady state after around 4000s, in both conditions. This is quite long running-in considering that the samples were already submitted to a previously running-in, as specified in the Section 6.3. Long running-in in the total concentration of emissions is equally noticed for all samples, in both conditions. Interestingly, this is not the only similarity between friction coefficient and total concentration curves: they exhibit corresponding behavior. For example, in case of sample 3 in scorched condition, the evolution of friction coefficient does not follow the typical behavior of friction coefficient curves. Instead of a short running-in with increasing friction coefficient, the curve displays a long step of running-in, in which the coefficient of friction increasing in a very low rate. The corresponding curve of total concentration follows the same behavior. Such correspondence is better observed Figure 7.6, confirming the unusual behavior and the similarity between the curves.

a)

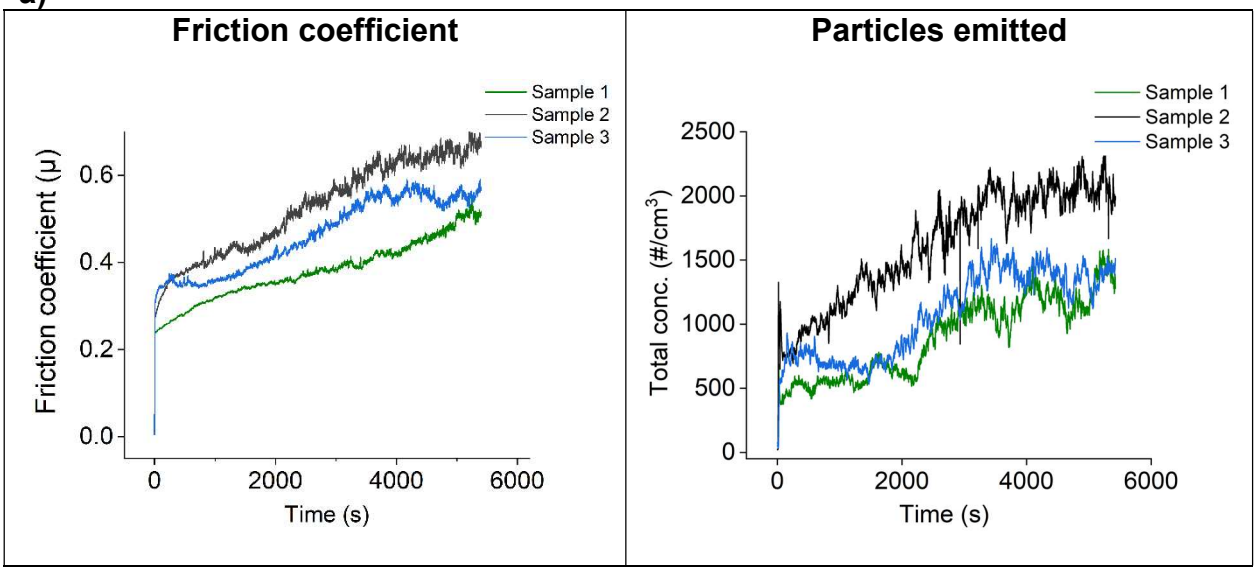

b)

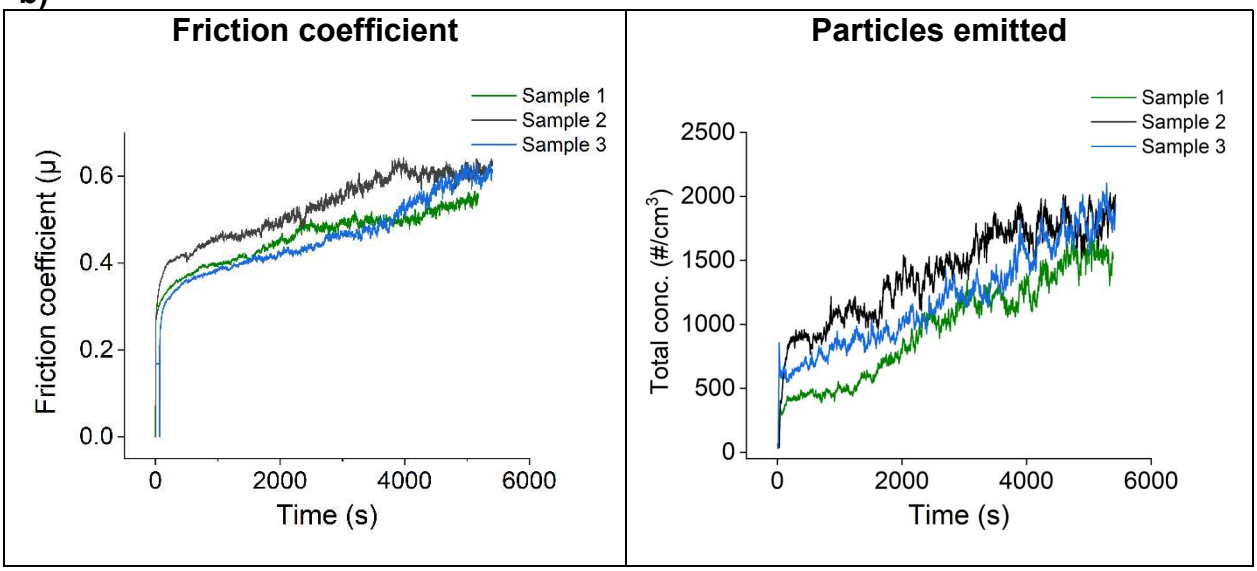

Figure 7.5: Evolution of the friction coefficient and total concentration of emitted particles obtained from PoD tests conducted on Cu-full material, in (a) scorched and (b) bulk conditions.

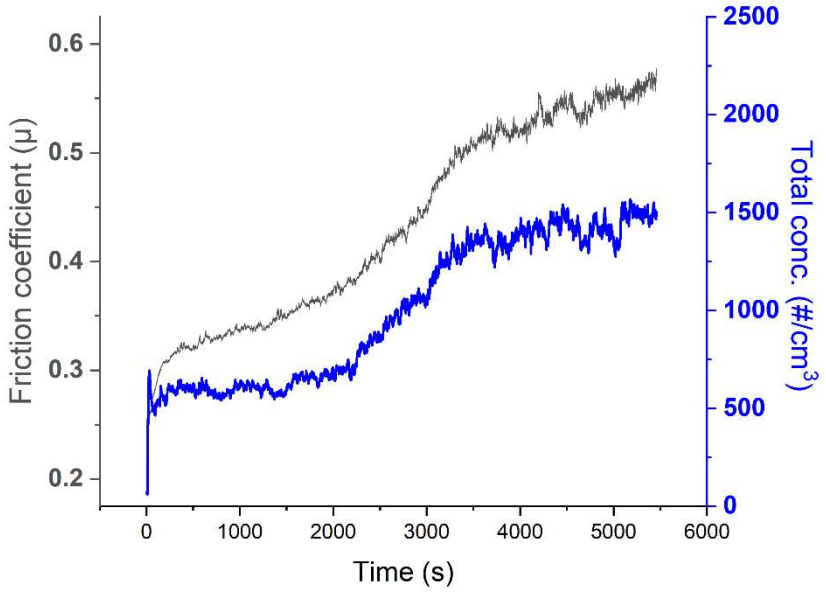

Figure 7.6: Evolution of the friction coefficient and total concentration of emitted particles of sample 3 of Cu-full scorched.

Figure 7.7 shows the evolution of the friction coefficient and the total concentration of emitted particles from PoD tests conducted on Cu-free friction material, in (Fig. 7.7a) scorched and (Fig. 7.7b) bulk condition. In this case, long running-in of friction coefficient is observed only in bulk condition, featuring around 4000s. Instead, all samples in scorched condition exhibit a stable behavior after around 2000s. In analogy to the observations for the Cu-full material, the emissions follow same trend of its corresponding friction coefficient curves. To allow a better view of such correspondence, Figure 7.8 shows in the same graph the friction coefficient and the emissions for sample 1 in scorched condition.

a)

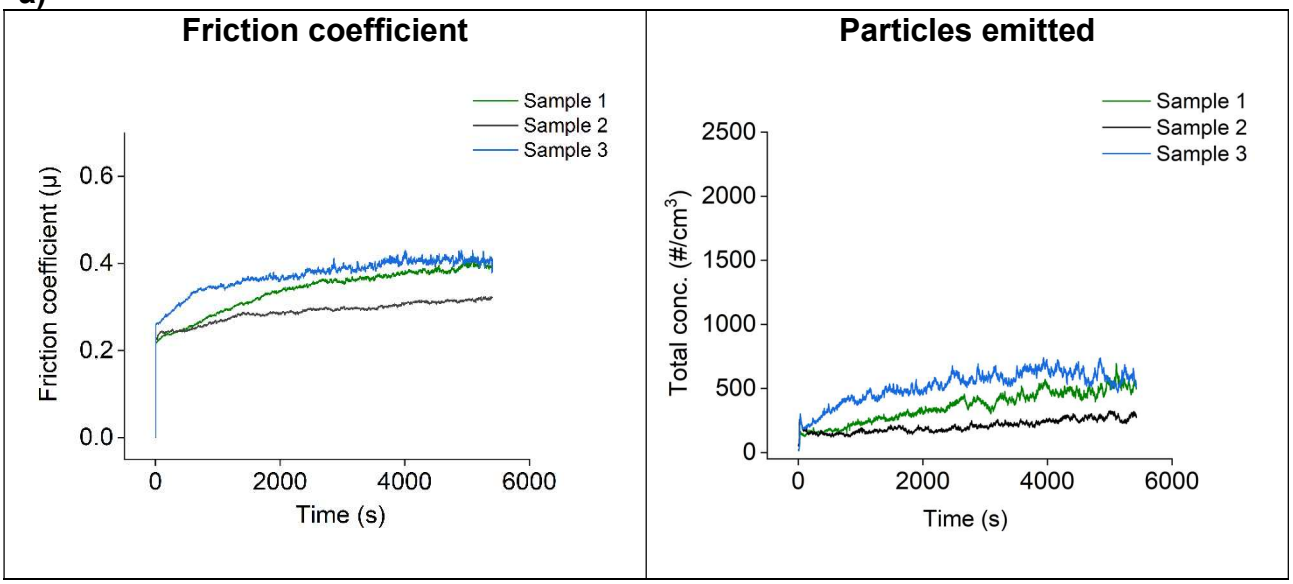

b)

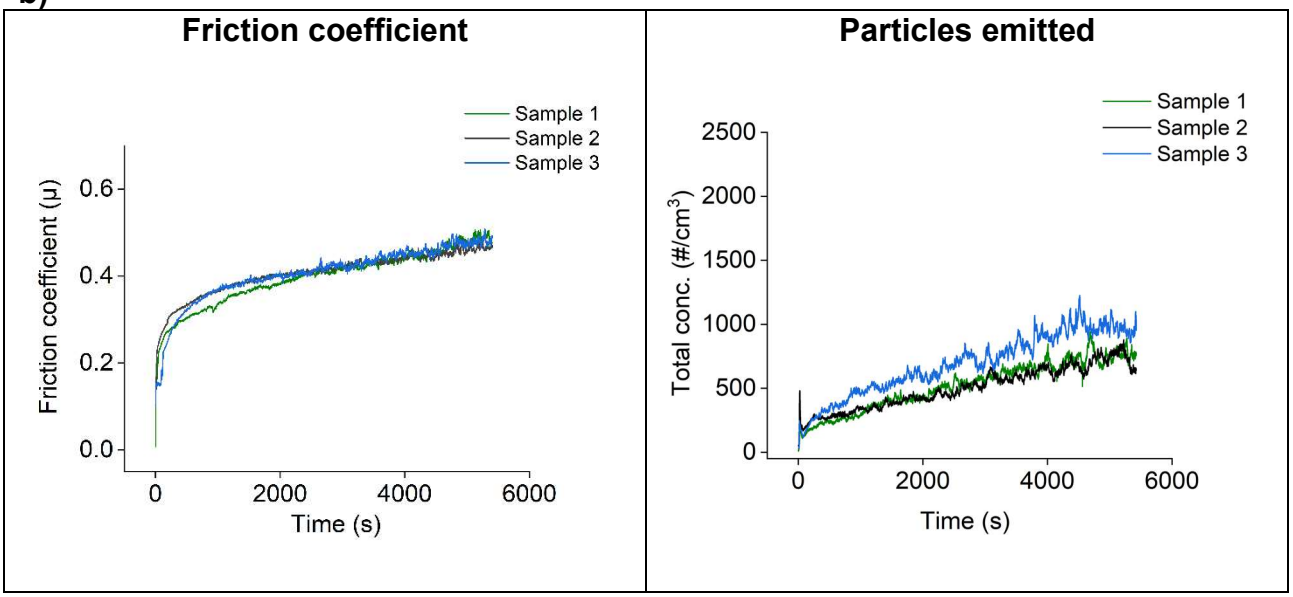

Figure 7.7: Evolution of the friction coefficient and total concentration of emitted particles obtained from PoD tests conducted on Cu-free material, in (a) scorched and (b) bulk conditions.

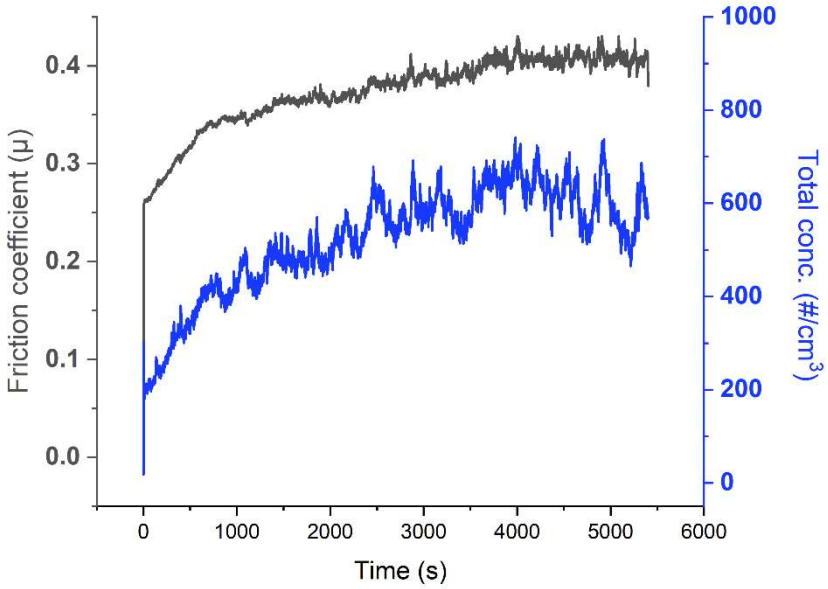

Figure 7.8: Evolution of the friction coefficient and total concentration of emitted particles of sample 1 of Cu-free scorched.

The similar behavior of the curves observed for both materials Cu-full and Cu-free indicates a relationship would exist between the friction behavior and the emissions of the airborne particles.

A corresponding increase in both friction coefficient and emissions during PoD tests was also evidenced by Alemani et al. [126] and Nosko et al. [100]. However, in these investigations, the explanation involves the high temperatures achieved during the tests: the friction coefficient increases with the contact temperature; consequently, the formation of wear debris is favored. Moreover, as discussed in Section 5.6.2, above the critical temperature (temperature of degradation of the organic matrix), the emissions increase tremendously.

The temperature displayed by all tests conducted on the present investigation have never exceeded 80 °C. An example is given in Figure 7.9, showing the evolution of the temperature during a test with Cu-full - condition bulk.

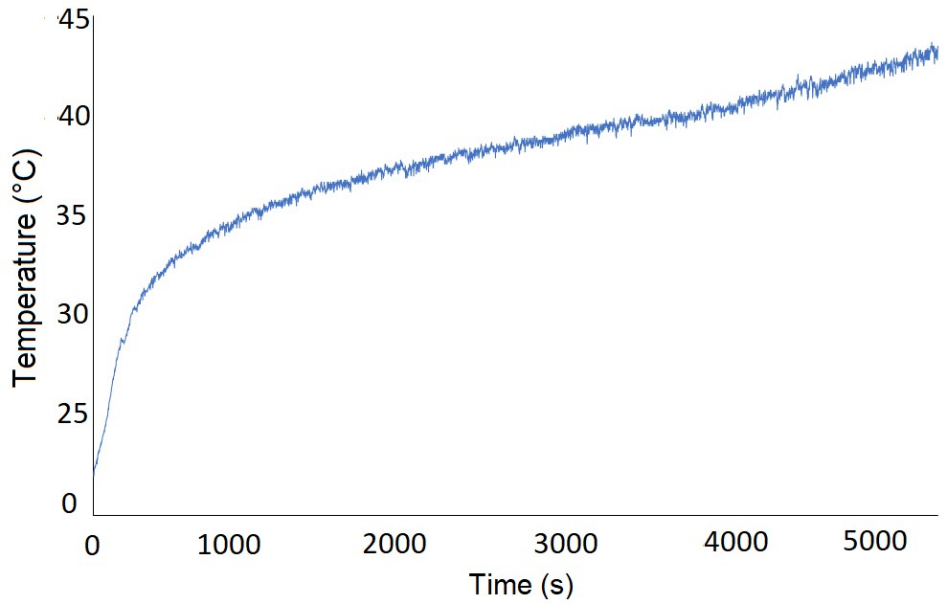

Figure 7.9: Disc temperature during the PoD test for Cu-full in bulk condition.

Figure 7.10 (a and b) shows the mean values of the friction coefficient and the total concentration of particles in the steady-state conditions, respectively. The Cu-full material features friction coefficient of 0.56 for both conditions; higher than the values for the Cu-free scorched (0.36) and bulk (0.46). Same trend is observed for the emissions: Cu-full displaying close values for both conditions (around 1500 #/cm^3), higher than Cu-free scorched (454 #/cm^3) and bulk (802 #/cm^3).

Comparing the conditions, no differences can be detected between the scorched and bulk in case of the Cu-full material, for both friction coefficient and total concentration of particles. Instead, in case of the Cu-free friction material, the difference is evident: the bulk condition displays higher values than scorched. This means that with the Cu-free material, the removal of the scorched region leads to an increase in the friction coefficient, and a correspondingly higher total concentration of emissions.

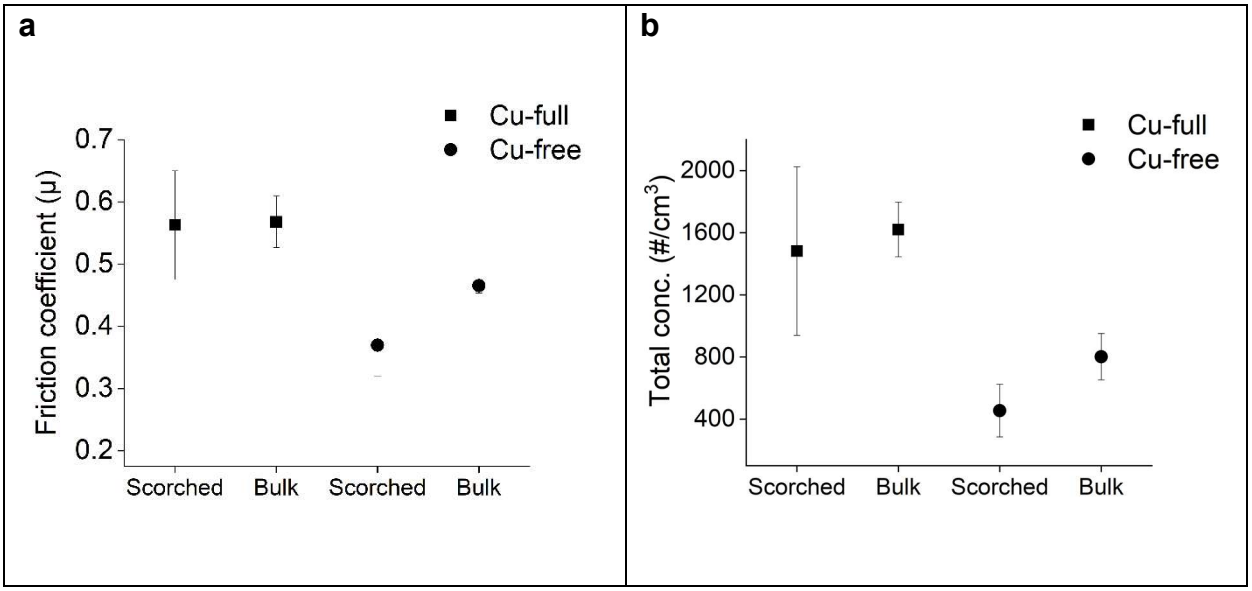

Figure 7.10: Mean values of (a) friction coefficient and (b) total concentration of emitted particles at steady-state for Cu-full and Cu-free friction materials in the scorched and bulk conditions.

Figure 7.11 (a and b) shows the values of the specific wear coefficient (Ka) of the pins. To calculate the wear, the total volume of lost material during the entire test is considered. Cu-full friction material exhibits higher wear than Cu-free, but any appreciable difference between scorched and bulk is noticed. On the other hand, the Cu-free displays slightly higher wear in bulk condition than in scorched. In all cases, the materials exhibit a mild wear, as expect for mild conditions of testing.

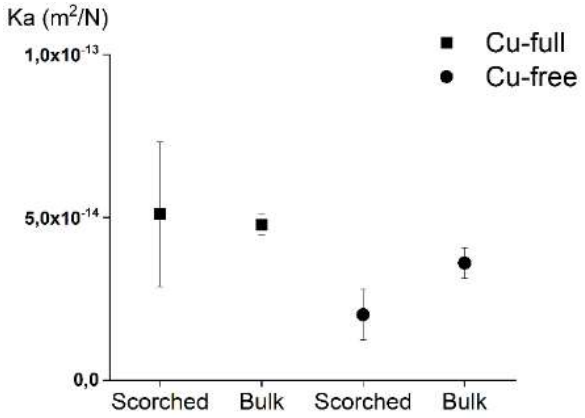

Figure 7.11: Mean values of specific wear coefficient of Cu-full and Cu-free friction materials in the scorched and bulk conditions.

7.3 Characterization of the pin's worn surfaces

SEM observations of the pin's worn surfaces, both planar and cross-sectional views, allow to identify the contact plateaus. Since these are the real contact areas between friction material and disc during the sliding contact, their characterization enables a better understanding of the tribological response of the couple. The SEM planar views of the pin's worn surfaces for both materials and conditions are given in Figure 7.12. The primary plateaus (marked as "1") are well defined and formed by steel fibers, identified by EDXS maps do not present herewith. Copper fibers, if present, may also act as primary plateaus. The secondary plateaus (marked as "2") are mainly made by the compaction of wear fragments, as discussed in Section 4.2, originated from the wear of both friction material and counterface disc. Cu-full in both conditions (Fig. 7.12 a and b) features secondary plateaus more compact and with higher extension than Cu-free friction material (Fig. 7.12 c and d). Loose particles around the secondary plateaus are present, especially in case of Cu-full scorched and both conditions of Cu-free. These particles are wear debris which pilled up close to the fibers, since the fibers acting as a barrier for debris moving [66]. This phenomenon shows the mechanism of formation the secondary plateaus, extensively discussed in Section 4.2. In general, at the first stage of the secondary plateaus formation, the wear debris pile up close to the primary plateaus (hard fibers/particles) and by the action of the pressure and sliding, they are compacted. In case of Cu-full bulk (Fig. 7.12b), the wear debris were almost totally compacted, showing the ability of this material in well-forming the secondary plateaus. On the other hand, in Cu-free scorched, a lot of loose particles can be noticed and consequently lower extension of the secondary plateaus. These observations can explain the higher friction coefficient displayed by Cu-full, since the μ is given by;

$$\sigma_m A_r / F_N \qquad (7.1)$$

where A_r is the contact area of the mating surfaces, i.e., the extension of the contact plateaus. Thus, higher real contact area determines a higher friction coefficient. Other regions of the pin's surfaces were analyzed and confirm the higher extension of plateaus for Cu-full compared to Cu-free. In fact, the ability of copper in favouring the formation and stabilization of the secondary plateaus was already demonstrated by Kumar et al. [48].

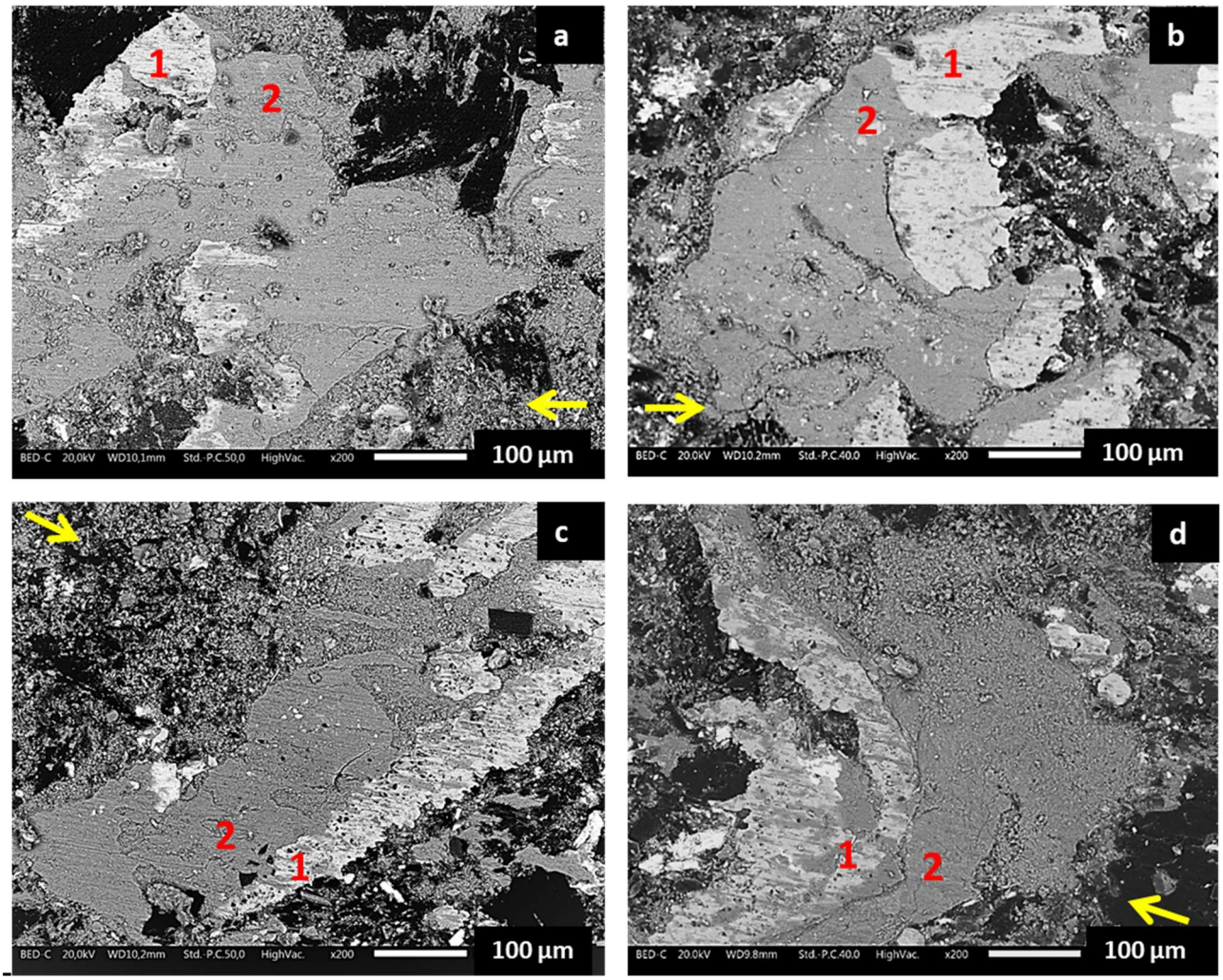

Figure 7.12: SEM micrographs of pin's worn surface: (a) Cu-full scorched, (b) Cu-full bulk, (c) Cu-free scorched, (d) Cu-free bulk. The arrows indicate the sliding direction and 1- primary plateaus; 2- secondary plateaus [125].

Figure 7.13 shows the SEM micrographs of the cross-sections of the pins tested in bulk condition, for both materials. The secondary plateaus observed on Cu-full is thicker than on Cu-free. This fact agrees with the observations on pin's worn surface (Figure 7.10), confirming the tendency of the Cu-full material to easily form secondary plateaus in its friction layer. The cross-sections of pins in the *scorched* condition were not analyzed since the same pins were successively tested in bulk condition.

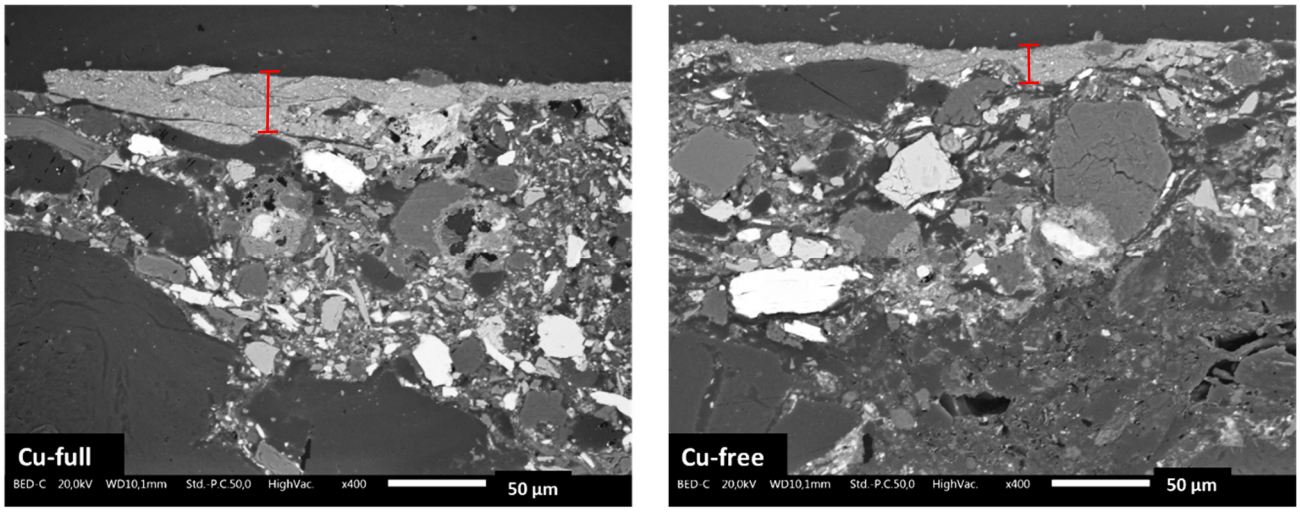

Figure 7.13: SEM micrographs of the cross-sections of pins: Cu-full and Cu-free, both in bulk condition.

To complete the characterization of the friction layer, the elemental composition of the secondary plateaus analyzed on the cross-section is given in Table 7.2, without considering the carbon content. Following the composition of the virgin materials, the main difference on the composition of the secondary plateaus of Cu-full as compared to the Cu-free material is the higher amount of iron onto the Cu-free and, of course, the presence of copper on the Cu-full. Furthermore, for both materials, the amount of iron on the secondary plateaus is higher than in virgin material (see Table 7.1), due to the contribution of disc wear.

Table 7.2: Elemental composition of secondary plateaus of Cu-full and Cu-free analyzed on the cross-section.

Element (wt.%)	Cu-full	Cu-free
Fe	58.2 ±2.8	65.5 ±2.3
Mg	2.8 ±0.8	2.9 ±1.3
Zn	5.8 ±1.3	2.1 ±1.1
Al	2.4 ±0.7	2.2 ±0.9
Si	1.5 ±0.6	1.7 ±0.2
S	2.1 ±0.3	2.1 ±0.5
Cu	2.6 ±0.9	-
Sn	3.4 ±1.1	1.9 ±0.7
Ca	1.3 ±0.2	1.0 ±0.4
Cr	0.9 ±0.1	0.8 ±0.2
O	18.8 ±2.8	19.4 ±3.2

7.4 Characterization of the PM emissions

The morphology of the airborne particles collected by the impactor in size ranging from 10 to 2.5 µm is shown in Figure 7.14, for the Cu-full and Cu-free materials, in scorched and bulk conditions. Both coarse particles shaped-like flake and small rounded particles can be appreciated in all cases. Mostly of these coarse particles own a flat face (see arrows), indicating they came from regions which were in contact, i.e, the contact plateaus. In fact, as discussed in Section 2.2, the tribo-oxidative wear is a typical wear mechanism for brake systems, consisting in a breakage of the layer formed between the surfaces.

Cu-full features higher fraction of comparatively coarse particles, as compared to Cu-free. This is in agreement with the more compacted secondary plateaus observed in Figures 7.12 and 7.13 for Cu-full. The presence of copper that renders the friction layer more compact, resulting in the formation of coarser fragments on its disruption [49, 126].

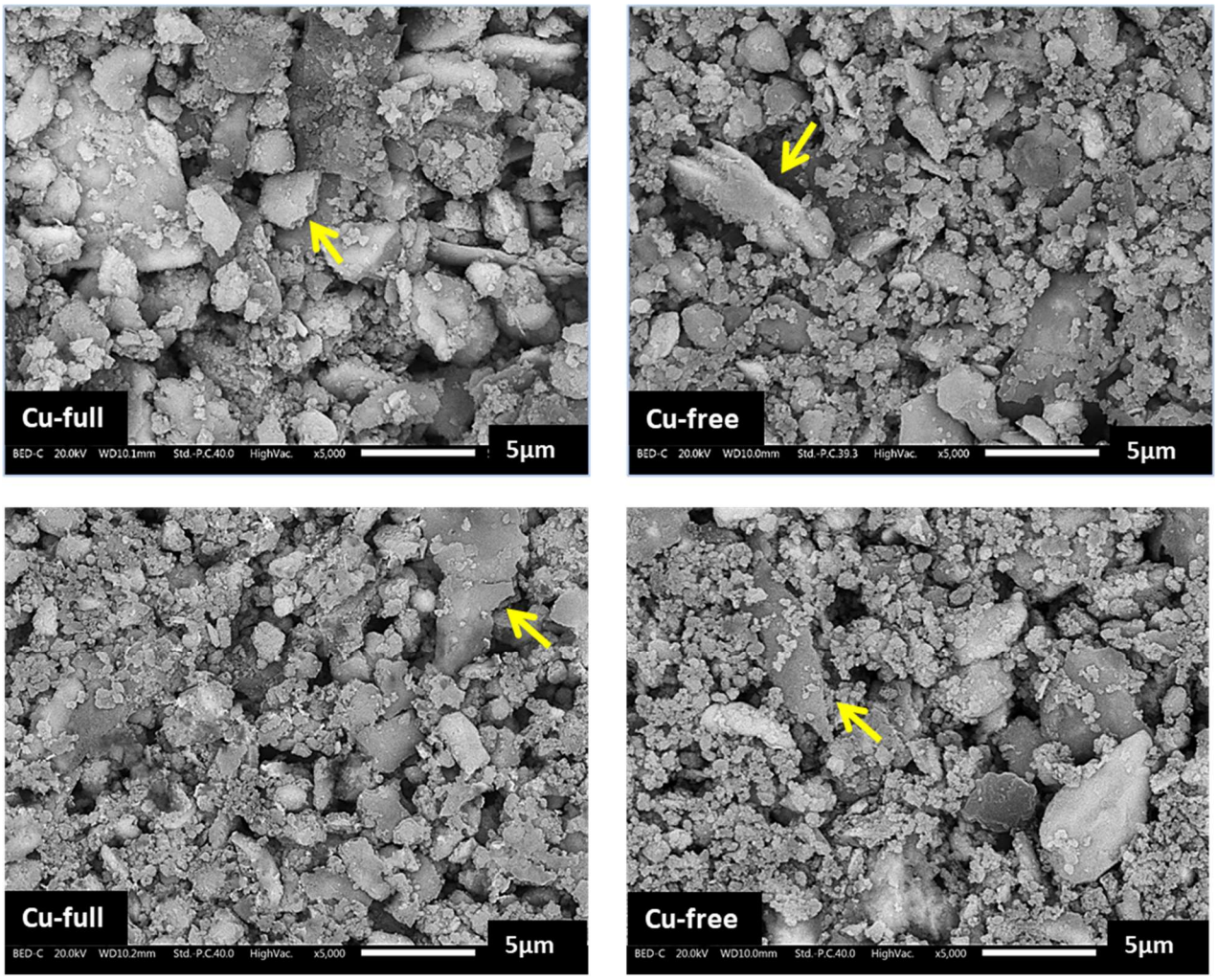

Figure 7.14: SEM micrographs of the airborne particles with the 10 - 2.5 µm aerodynamic diameter range. Above: scorched condition. Below: bulk condition [125].

Figure 7.15 shows a secondary electron (SE) SEM micrograph of airborne particles from the tests on the Cu-free material, sizing from 10 to 2.5 µm, it is possible to recognize some sliding marks on the coarse particle at the center of the image (see arrow). This fact confirms that such flat particles came from a region of contact. Indeed, according to Eriksson et al. [66], the plateaus can be defined as the areas of the pad showing signs of sliding contact with the disc and typically, these signs involve a relatively flat surface with shallow grooves in the sliding direction.

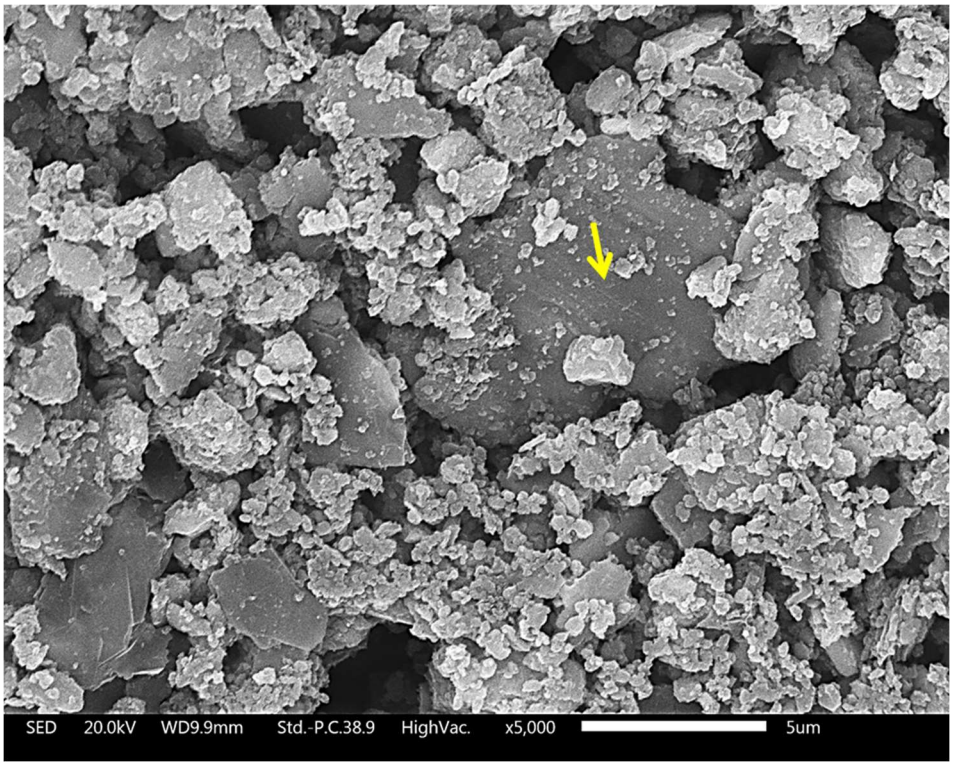

Figure 7.15: SE-SEM micrograph of the Cu-free airborne particles with the 10 - 2.5 μm aerodynamic diameter range. The arrow indicates the particle in which sliding marks can be recognized.

The SEM micrographs of the airborne particles sizing from 2.5 to 1 μm are given in Figure 7.16, for both materials and conditions. The flat coarse particles are also observed for the smaller size range (see arrows). However, in this case, the predominance of these flake particles is not so clear, showing a high fraction of rounded particles as well, especially for bulk condition for both materials.

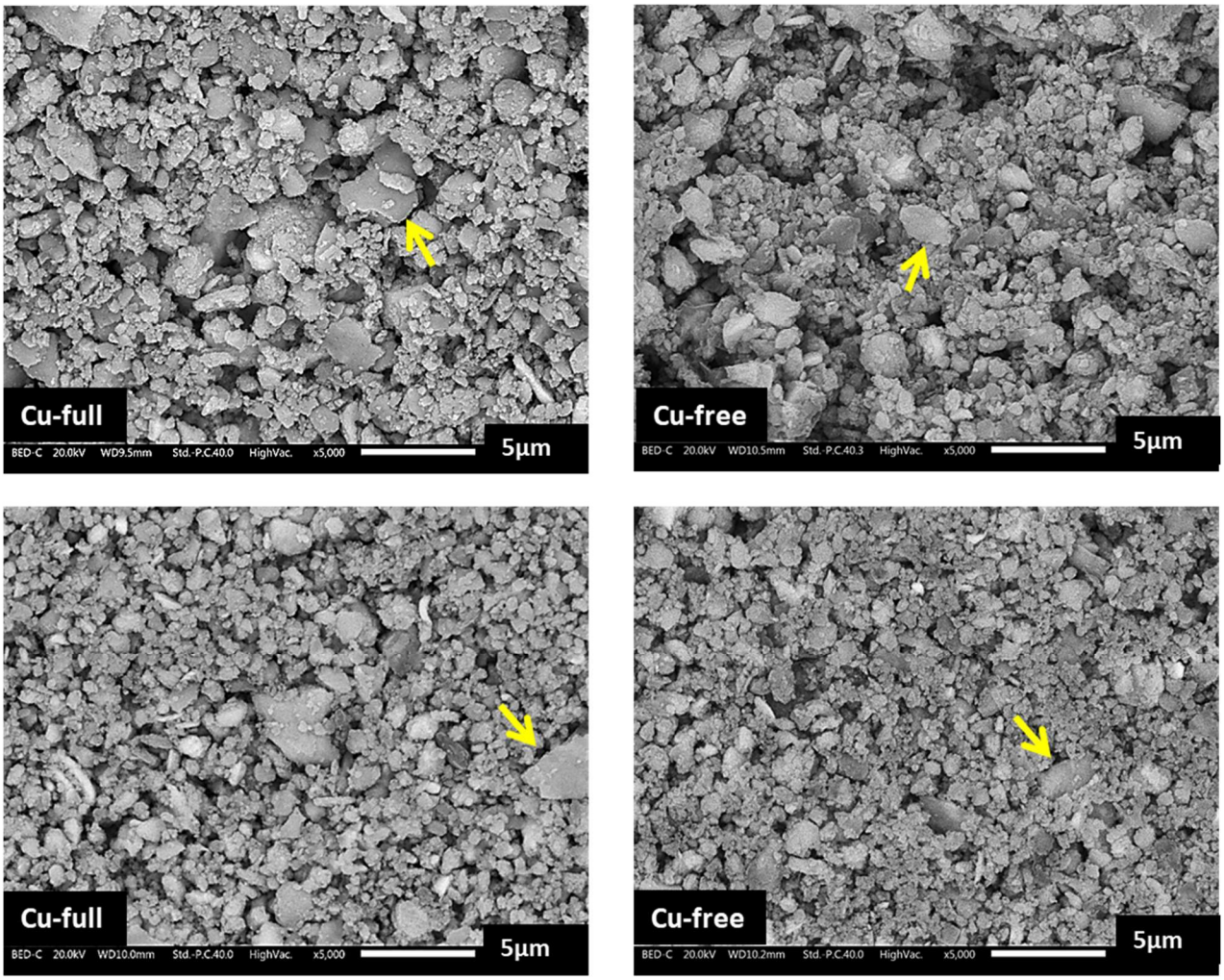

Figure 7.16: SEM micrographs of the airborne particles with the 2.5 - 1 µm aerodynamic diameter range. Above: scorched condition. Below: bulk condition.

Figure 7.17 and Figure 7.18 show the SEM/EDXS elemental composition of a coarse single particle for Cu-full and Cu-free materials, respectively. Iron and oxygen are the main detected elements in both cases, also containing small content of elements from the friction material, such as zinc and aluminum. These results are in line with [66, 72], which describe iron oxide as the main compound of the coarse and fine brake emissions.

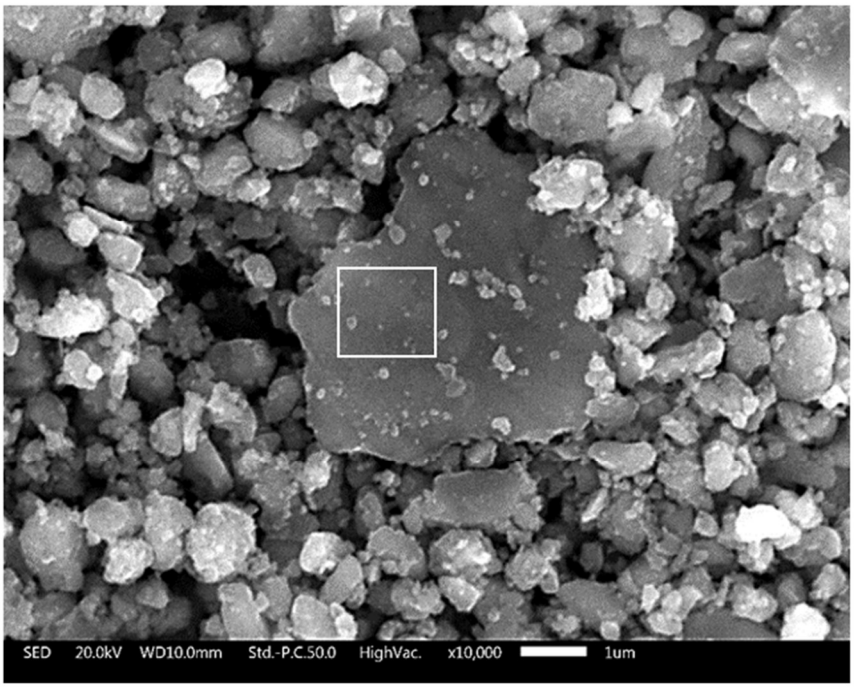

Element	wt.%
Fe	61.2
O	24.0
Mg	2.1
Zn	2.9
Al	2.1
S	1.4
Sn	1.9
Si	1.3
Cu	1.3
Ca	0.7
Cr	0.7
Mn	0.7

Figure 7.17: SEM/EDXS elemental composition of the indicated particle, from tests with Cu-full material.

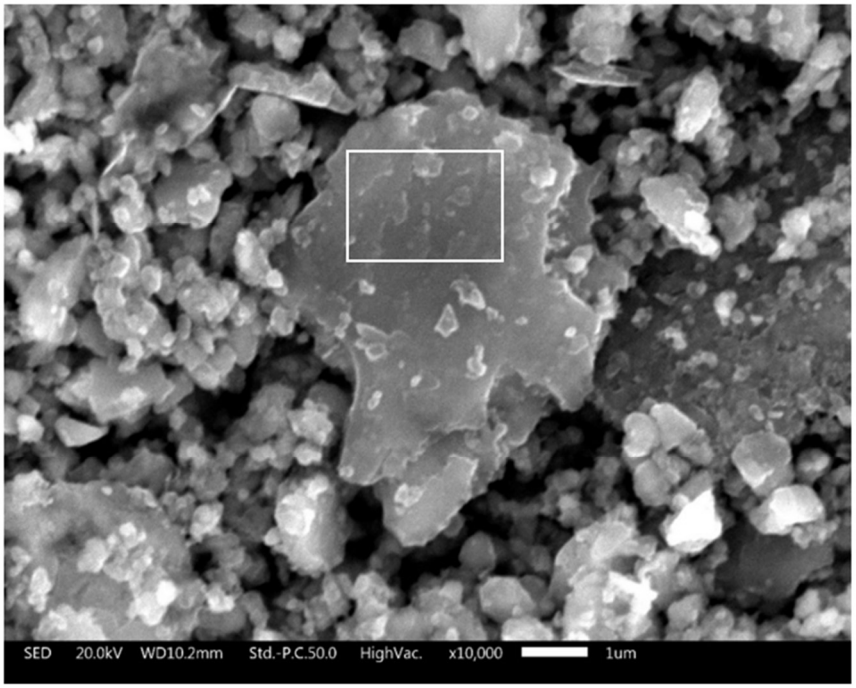

Element	wt.%
Fe	60.3
O	30.8
Mg	0.6
Zn	2.9
Al	0.8
S	0.4
Sn	1.6
Ca	1.0
Cr	1.8
Mn	0.6
Si	0.1

Figure 7.18: SEM/EDXS elemental composition of the indicated particle, from tests with Cu-free material.

Table 7.3 revels the elemental composition of the airborne particles for Cu-full and Cu-free materials, both in bulk conditions. In order to obtain results representative of the overall emissions composition, the measurements were fulfilled in full frame low

magnification images (e.g., 700x original magnification), able to analyze a significant amount of particles. For both materials, the emissions have nearly the same composition to their corresponding secondary plateaus.

Table 7.3: Elemental composition of the particle matter in two different size range for Cu-full and Cu-free friction materials in bulk condition.

	Cu-full		**Cu-free**	
Element (wt.%)	**Particles from 10 – 2.5 µm**	**Particles from 2.5 – 1 µm**	**Particles from 10 – 2.5 µm**	**Particles from 2.5 – 1 µm**
Fe	63.3 ±2.5	63.3 ±2.3	68.9 ±3.0	68.8 ±2.6
Mg	2.6 ±1.0	2.5 ±0.6	2.7 ±0.6	2.5 ±0.4
Zn	3.5 ±0.6	4.3 ±0.9	2.9 ±0.4	3.1 ±1.1
Al	3.0 ±0.4	2.7 ±0.3	3.0 ±0.2	2.7 ±0.3
Si	2.0 ±0.2	1.7 ±0.1	2.2 ±0.4	1.7 ±0.1
S	2.1 ±0.3	1.9 ±0.3	2.3 ±0.1	2.3 ±0.2
Cu	5.3 ±1.3	5.1 ±0.8	-	-
Sn	3.3 ±0.1	3.2 ±0.6	2.3 ±0.3	2.4 ±0.2
Ca	1.3 ±0.1	1.2 ±0.2	0.7 ±0.2	0.7 ±0.2
Cr	1.1 ±0.1	1.1 ±0.0	1.0 ±0.3	1.3 ±0.1
O	12.2 ±1.4	12.8 ±1.5	13.1 ±1.8	13.0 ±0.9

To allow for an easier and straightforward interpretation, Figures 7.19 and 7.20 show a comparison of EDXS data for the virgin material, secondary plateaus and PM emissions in the bulk condition. The amount of iron increases in passing from the virgin material to the secondary plateaus and airborne particles, due the contribution to the wear coming from the counterface cast iron disc. Comparing the secondary plateaus to the collected particles, its elemental composition is very similar, which confirms the disruption of the friction layer as the origin of particulate matter emissions.

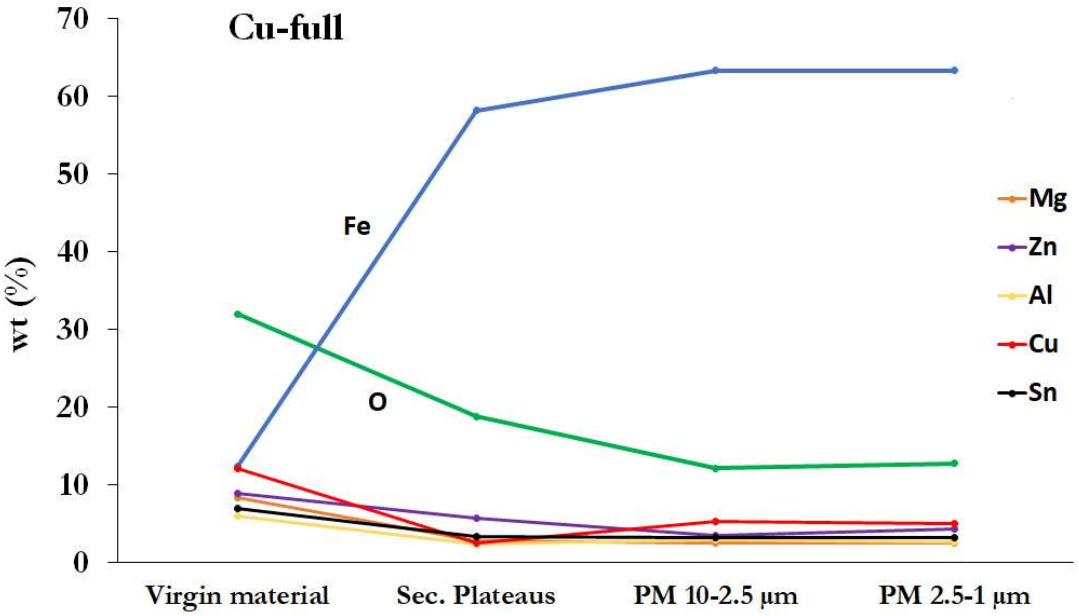

Figure 7.19: Comparison of the compositional values of different regions (virgin material, secondary plateaus cross section, airborne particles PM 10-2.5 µm and PM 2.5-1 µm) for Cu-full friction material.

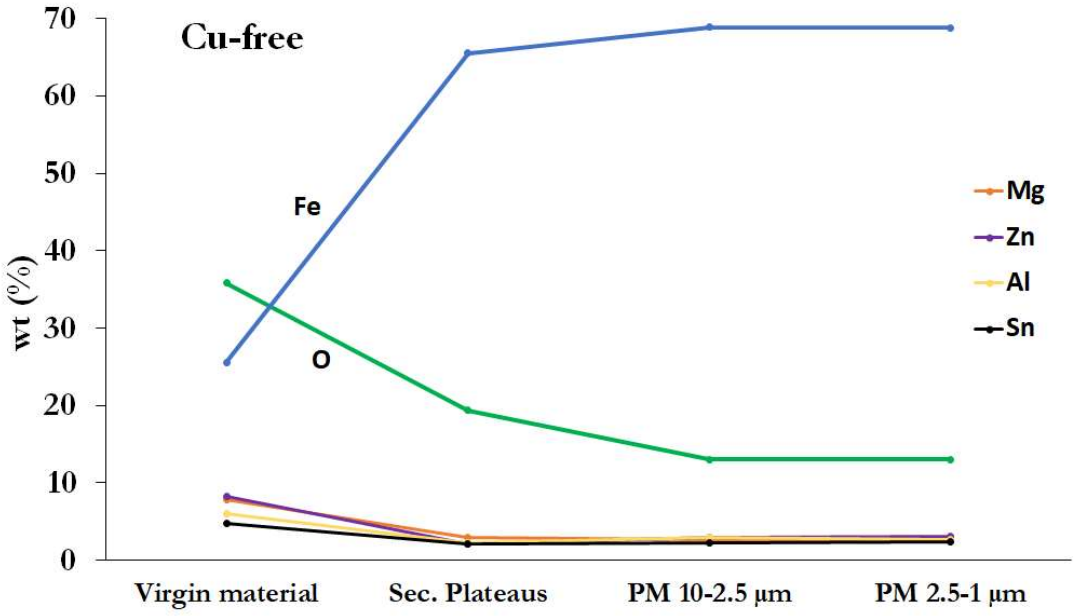

Figure 7.20: Comparison of the compositional values of different regions (virgin material, secondary plateaus cross section, airborne particles PM 10-2.5 µm and PM 2.5-1 µm) for Cu-free friction material.

7.5 Final comments

From the results herewith presented it turns out an important role is played by the friction layer, affecting both the tribological performances and airborne particle emission. A larger extension of the secondary plateaus leads to a higher friction coefficient, owing to a larger real contact area. At the same time, since more extensive and thicker secondary plateaus in the friction layer are formed, its disruption produces a larger amount of airborne particles, particularly coarse ones, as noticed in case of Cu-full friction material. This fact is in agreement with the observed relationship between friction coefficient and emissions curves (see Figg 7.6, 7.8), as well as the similarity of the elemental composition between the emitted particles and the secondary plateaus. Moreover, the flat surface morphology displayed by many collected particles, especially the coarser ones, and the sliding marks recognized on some of them, confirm that these particles actually come from the disruption of the secondary plateaus.

As concerns the effect of the scorching treatment, this was observed for the Cu-free material only. Indeed, in scorched condition lower friction coefficient, wear rate and emissions, compared to the bulk, were recorded. In fact, the heating of the pad surface at around 650 ºC involved with the scorching treatment can lead to two counteracting effects: the decrease in the cohesion of the components for the carbonization of the organic matrix; and the sintering of the components induced by the elevated temperature. In case of the Cu-free material, the extent of carbonization of the organic components is significantly lower than in the Cu-full material, as evidenced by the lower thickness of the relevant heat altered layer (Fig. 7.4). Consequently, the surface sintering was more pronounced, increasing the wear resistance of the friction material with a consequent reduction in the particle emission.

Chapter 8

PM brake emissions from two commercial Cu-free friction materials

This chapter investigates the tribological behavior and the corresponding PM emissions in two low-metallic commercial friction materials, aiming at better understanding the effect of abrasive ingredients on the emissions generation. Both materials are Cu-free, one featuring a relatively high content of abrasives and the other one a particularly high amount of filler. As discussed in Section 3.4.1, these ingredients, i.e., abrasives and fillers, play different roles in the friction materials. The abrasives are hard particles and are meant to increase the friction coefficient and improve the overall wear resistance. They are also described as essential in supplying wear fragments necessary for the formation of the secondary plateaus. Instead, fillers are added in friction materials mainly to reduce their cost without compromising the performance.

In the Chapter 7, a clear relationship between the friction coefficient and the emissions was noticed, and the key for such relation is the friction layer formed on the mating surfaces. In this present investigation, a deeper characterization of the friction layer was carried out, including the elemental composition of the secondary plateaus on top view.

Part of the results discussed in this chapter were published in [127].

8.1 Characterization of the friction materials

The elemental composition of both friction materials is given in Table 8.1. High relative amount of magnesium, zinc and aluminum can be noticed in case of material Cu-free/A. Those elements are usually added as oxides, behaving as abrasives. Instead, Cu-free/F displays high relative content of barium, added as the compound barite, used as a filler in friction materials. This latter friction material is the output result of the project ECOPADS (Eliminating COpper from brake PADS and recycling), aimed the development of a ‘green’ copper-free brake pad formulation, combining excellent brake performance and reduced certified emissions [128].

Table 8.1: Elemental composition of Cu-free/A and Cu-free/F materials. Carbon not quantified.

Element (wt.%)	Cu-free/A	Cu-free/F
Fe	18.2 ±1.5	12.2 ±2.6
Mg	9.8 ±0.8	6.2 ±0.1
Zn	12.3 ±1.7	8.7 ±0.5
Al	7.9 ±0.7	6.3 ±0.9
Si	3.4 ±0.6	2.8 ±0.3
S	8.7 ±0.9	11.4 ±0.7
Sn	6.8 ±0.6	5.4 ±0.1
Ca	3.9 ±0.1	3.0 ±0.0
Cr	2.5 ±0.4	1.8 ±0.1
O	21.9 ±1.5	17.2 ±0.5
Ba	-	25.1 ±0.4

8.2 Tribological and emissions behavior

The evolution of both friction coefficient and the total concentration of emissions from representative PoD tests conducted on Cu-free/A and Cu-free/F is given in Figure 8.1. In the friction coefficient curves, a running-in of around 2000s and 1000s can be appreciated for Cu-free/A and Cu-free/F, respectively. Regarding the emissions, a rather longer running-in is noticed and the steady-state is achieved at around 3000s in case of Cu-free/F and 4000s for Cu-free/A.

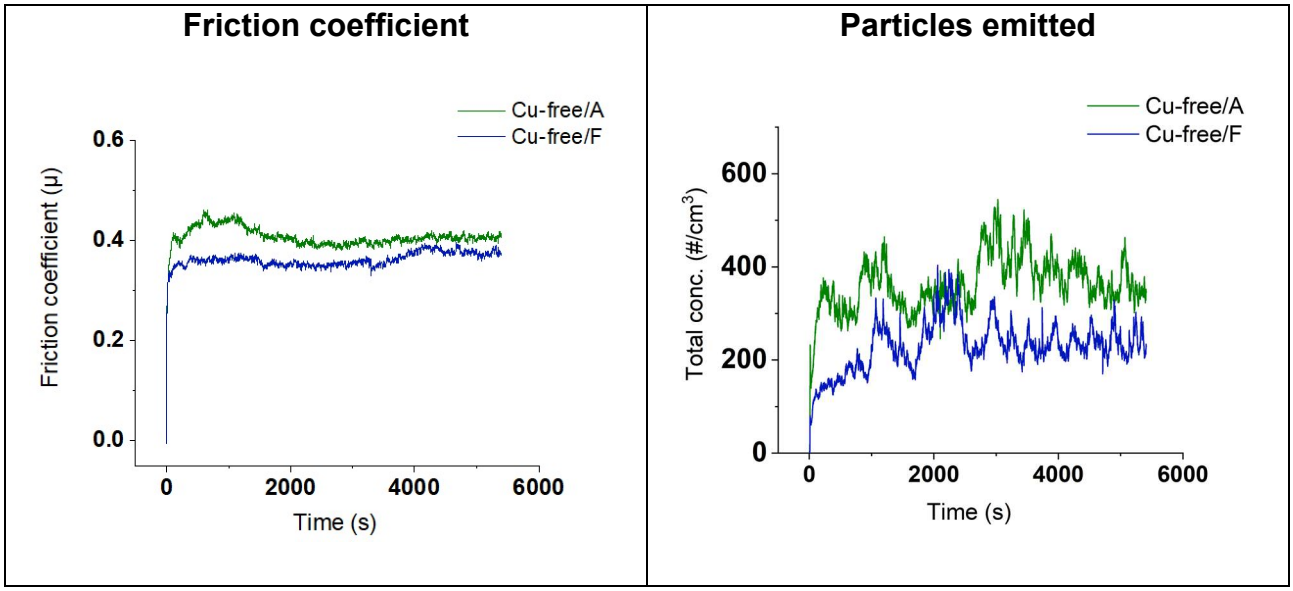

Figure 8.1: Friction coefficient and particle concentration evolutions obtained from representative PoD tests conducted on the two friction materials.

Figure 8.2a shows the mean values of the friction coefficient at the steady state regime for both materials. Cu-free/A features friction coefficient of 0.43 ±0.04, as expected higher than Cu-free/F, displaying 0.40 ±02. The corresponding total concentration of emissions is given in Figure 8.2b. Cu-free/A displays higher emissions than Cu-free/F, i.e., 294 ±69 #/cm^3 and 232 ±29 #/cm^3, respectively.

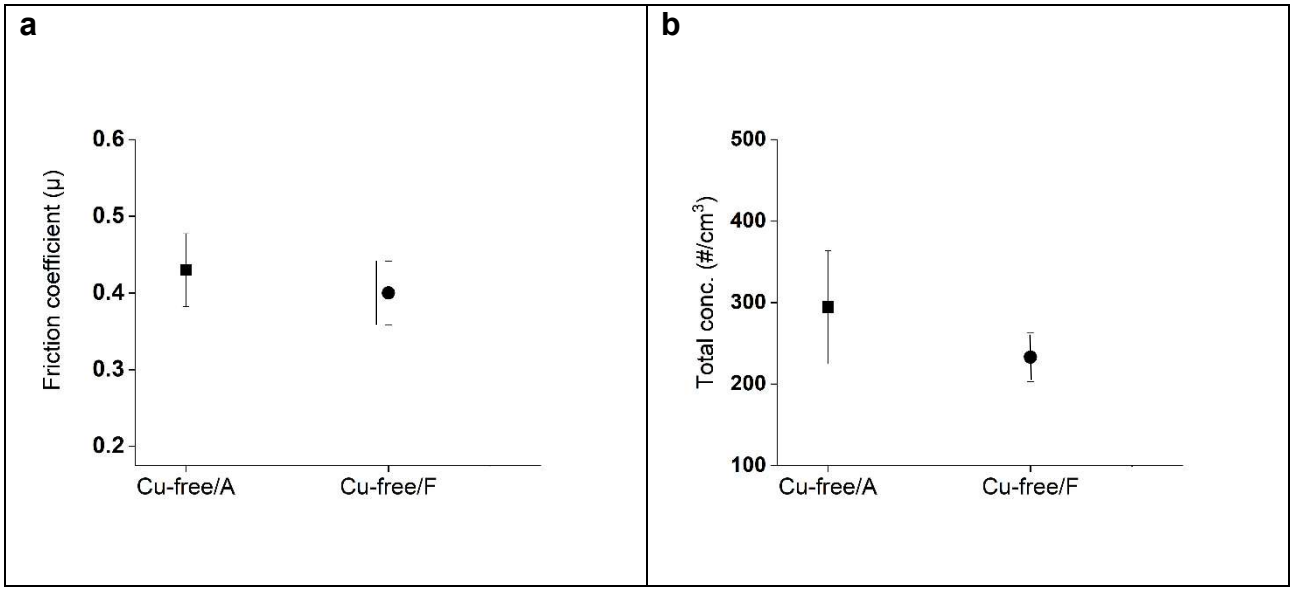

Figure 8.2: Mean values of (a) friction coefficient and (b) total concentration of emitted particles at steady-state for Cu-free/A and Cu-free/F.

Figure 8.3 shows the values of the specific wear coefficient (Ka) of the pins for both materials. The materials display similar wear rate. The comparatively lower emission presented by Cu-free/F can then be ascribed to a wearing out producing a higher fraction of relatively large fragments, which do not become airborne after abandoning the mating surfaces and therefore are not recorded by the particle counter experimental set up.

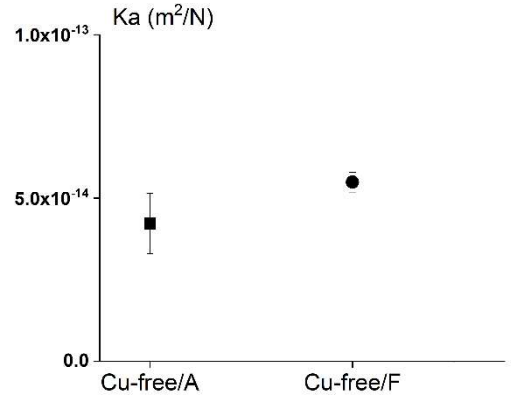

Figure 8.3: Mean values of pin's specific wear coefficient (Ka) for both friction materials.

8.3 Characterization of the pin's worn surfaces

Figure 8.4 shows the pin's worn surfaces for both friction materials. On the left side the images were obtained using backscattered electrons, whereas the corresponding SEM images at the right side were obtained using secondary electrons (SE). The presence of secondary plateaus close to the iron fibers can be appreciated in both materials. Cu-free/A displays higher extension secondary plateaus than Cu-free/F. Loose particles close to the secondary plateaus are more evident in case of Cu-free/F, with Cu-free/A featuring more compact secondary plateaus. This is also evident for darker and more uniform secondary plateaus in SE images (right side), as noticed for Cu-free/A.

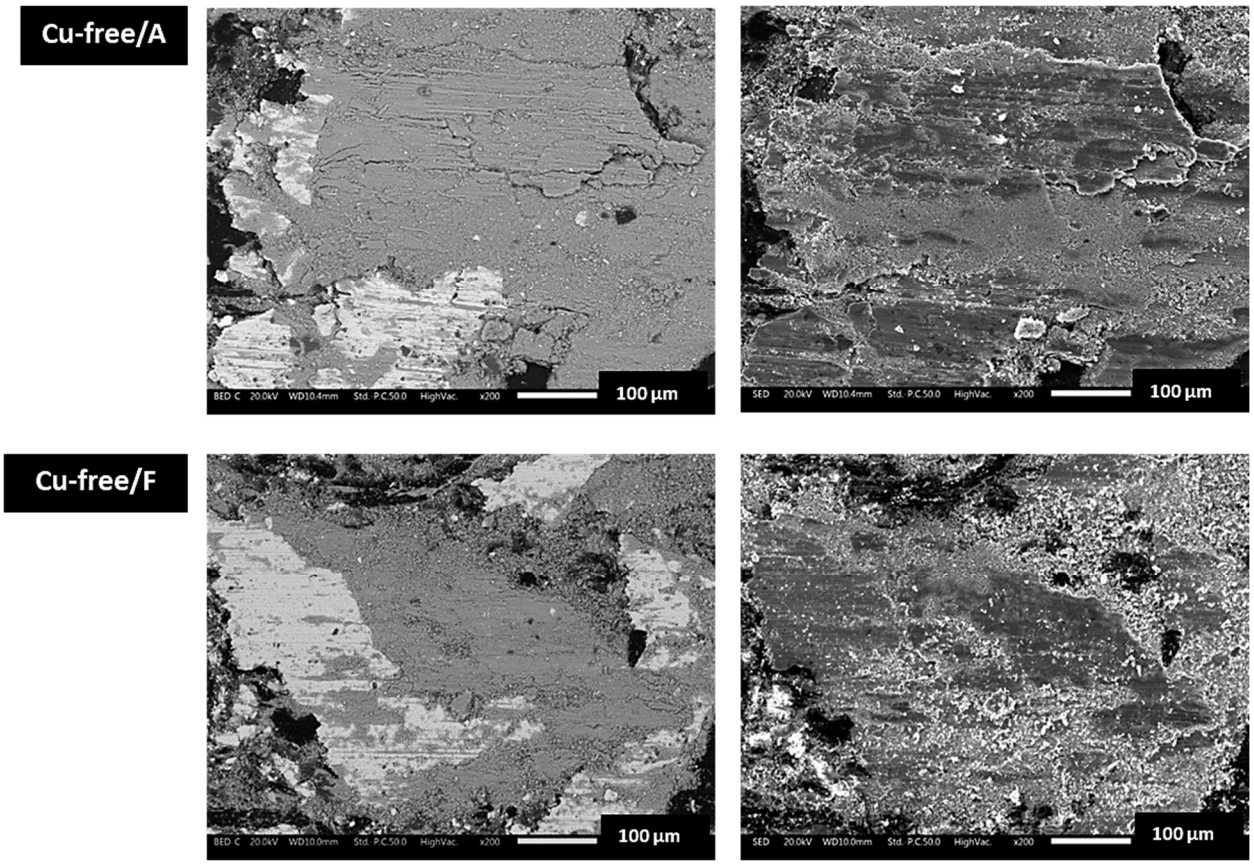

Figure 8.4: SEM micrographs of pin's worn surface for both friction materials. On left side: backscattered electrons. On right side: secondary electrons [127].

The elemental composition of the secondary plateaus measured on the surfaces from top view of pins is given by Table 8.2, for both tested materials. The same elements found in the virgin materials (Table 8.1) are all present in the secondary plateaus, but in different concentrations. In particular, an increased amount of iron is observed in both materials, indicating the contribution from the counterface disc wear.

Table 8.2: Elemental composition of secondary plateaus of Cu-free/A and Cu-free/F analyzed on the surface top view. Carbon not quantified.

Element (wt.%)	Cu-free/A	Cu-free/F
Fe	71.6 ±3.0	64.6 ±1.7
Mg	1.8 ±0.3	1.3 ±0.1
Zn	3.8 ±0.2	2.8 ±0.5
Al	1.9 ±0.1	1.3 ±0.1
Si	1.4 ±0.1	1.3 ±0.2
S	2.2 ±0.0	3.7 ±0.4
Sn	2.6 ±0.2	2.2 ±0.1
Ca	0.6 ±0.1	0.5 ±0.1
Cr	1.0 ±0.0	0.9 ±0.2
O	12.6 ±1.5	13.3 ±0.4
Ba	-	8.0 ±0.3

Beyond the fact that higher extension of secondary plateaus can lead to an increased friction coefficient due to a larger real contact area, the higher content of iron on the secondary plateaus of Cu-free/A compared to Cu-free/F may also affect the friction coefficient values. In fact, higher iron concentration provides a higher tribological compatibility with the cast iron counterface [1], thus increasing the adhesive interaction between the mating surfaces during braking and the relevant adhesive contribution to friction.

Figure 8.5 shows SEM backscattered electrons observations of the cross-section of the worn pins, where the secondary plateaus can be recognized. As observed already in surface planar images (Fig. 8.4), the Cu-free/A exhibits better formed secondary plateaus, featuring larger thickness. The elemental compositions measured on the cross-section of the secondary plateaus for both tested materials are given in Table 8.3. The results which

appear to be in agreement with the worn surface compositions shown in Table 8.2. However, the oxygen is present to a lower extent in the cross-section.

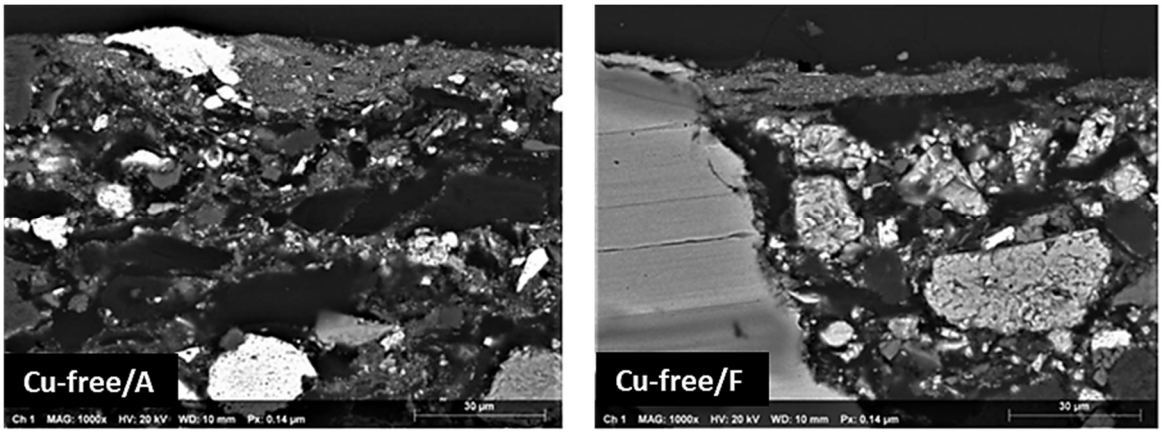

Figure 8.5: SEM micrographs of cross-section of the pins for both friction materials [127].

Table 8.3: Elemental composition of secondary plateaus of Cu-free/A and Cu-free/F analyzed on the cross-section. Carbon not quantified.

Element (wt.%)	**Cu-free/A**	**Cu-free/F**
Fe	72.9 ±1.5	65.2 ±1.7
Mg	1.3 ±0.3	2.6 ±0.3
Zn	5.9 ±0.5	4.2 ±0.7
Al	0.8 ±0.2	2.3 ±0.3
Si	0.5 ±0.1	3.2 ±1.6
S	3.8 ±0.3	5.1 ±0.6
Sn	3.4 ±0.7	2.2 ±0.1
Ca	1.2 ±0.1	0.5 ±0.1
Cr	0.8 ±0.1	0.9 ±0.2
O	9.1 ±0.5	4.2 ±1.1
Ba	-	9.1 ±0.8

Comparing the elemental composition of the secondary plateaus measured on the surface (Table 8.2) and on the cross-section (Table 8.3), the iron content does not appear to vary between the external surface (top view) of the secondary and the internal part (cross-section). The oxygen percentage does instead change depending on the distance from the pin surface. In particular, it goes down when moving from the top surface to the inner part of the friction layer. Furthermore, the oxygen-containing compounds, such as Al2O3, MgO and BaSO4, are usually present in higher amount in the plateaus cross-section with respect to its surface. All these remarks suggest that the observed oxygen gradient is mainly due to the oxidation of metallic iron present close to the surrounding environment, with the formation of iron oxides, such as magnetite and hematite [66, 67].

8.4 Characterization of the PM emissions

Figure 8.6 shows the SEM micrographs of airborne PM emissions for Cu-free/A and Cu-free/F, collected by the impactor 2.5–10 μm filters. For both materials, the predominance of coarse flake-shaped particles can be appreciated; most of them featuring a flat face, as highlighted by the arrows. Smaller rounded particles are also visible, in a relative lower amount though.

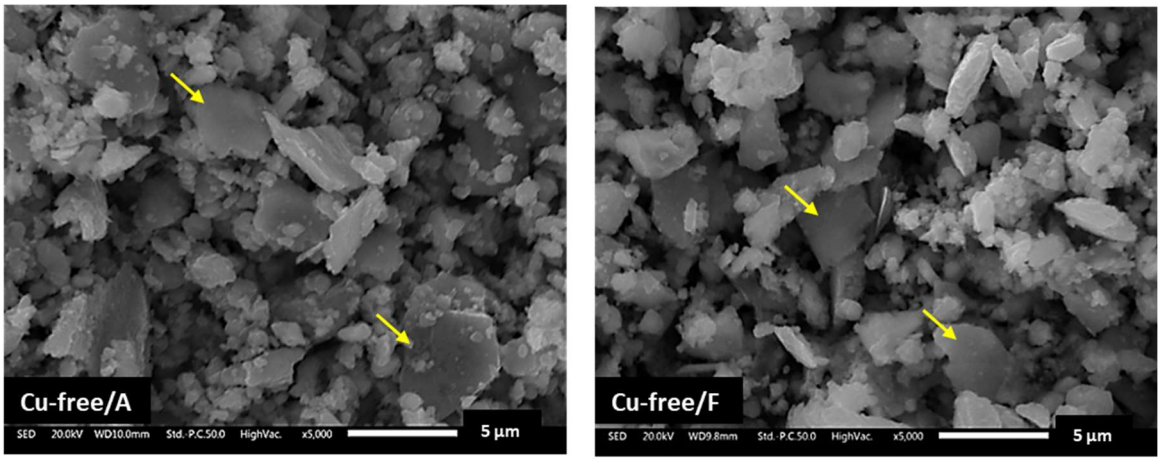

Figure 8.6: SEM micrographs of the airborne particles with the 10–2.5 μm aerodynamic diameter range, for both friction materials. The yellow arrows indicate particles featuring flat face [127].

The micrographs of the 2.5 to 1 μm particles is given in Figure 8.7, for both materials. Cu-free/A seems to feature a higher relative amount of flake-shaped particles with flat surfaces than Cu-free/F.

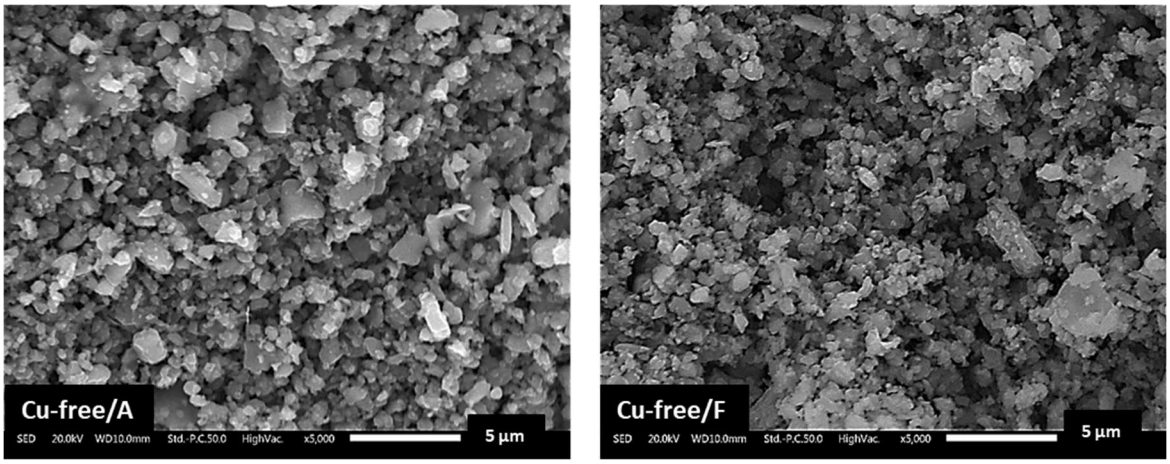

Figure 8.7: SEM micrographs of the airborne particles with the 2.5–1 µm aerodynamic diameter range, for both friction materials.

The elemental composition of the airborne particles is provided in Table 8.4. Both materials feature compositions of the emitted particles very similar to the secondary plateaus (Tables 8.2 and 8.3). To allow an easily interpretation, Figures 8.8 and 8.9 show a comparison of EDXS data for the virgin material, secondary plateaus (both surface top view and cross-section) and PM emissions.

Table 8.4: Elemental composition of emitted particles. Carbon not quantified.

	Cu-free/A		**Cu-free/F**	
Element (wt.%)	**Particles from 10 – 2.5 µm**	**Particles from 2.5 – 1 µm**	**Particles from 10 – 2.5 µm**	**Particles from 2.5 – 1 µm**
Fe	79.1 ±1.7	78.6 ±2.0	64.5 ±0.4	65.8 ±2.6
Mg	1.9 ±0.2	1.9 ±0.4	1.9 ±0.1	1.8 ±0.3
Zn	3.0 ±0.1	2.9 ±0.8	2.7 ±0.0	2.7 ±0.7
Al	1.7 ±0.1	1.7 ±0.3	1.9 ±0.1	1.9 ±0.3
Si	1.7 ±0.1	1.8 ±0.1	1.5 ±0.1	1.5 ±0.1
S	1.7 ±0.1	1.8 ±0.2	3.7 ±0.2	3.7 ±0.8
Sn	2.6 ±0.3	2.3 ±0.6	2.4 ±0.4	2.1 ±0.5
Ca	0.1 ±0.0	0.3 ±0.1	0.3 ±0.1	0.5 ±0.2
Cr	0.7 ±0.1	0.6 ±0.1	0.7 ±0.0	0.6 ±0.1
O	7.1 ±1.6	7.5 ±1.1	11.8 ±0.7	11.6 ±1.0
Ba	-	8.2 ±0.2	-	8.0 ±0.3

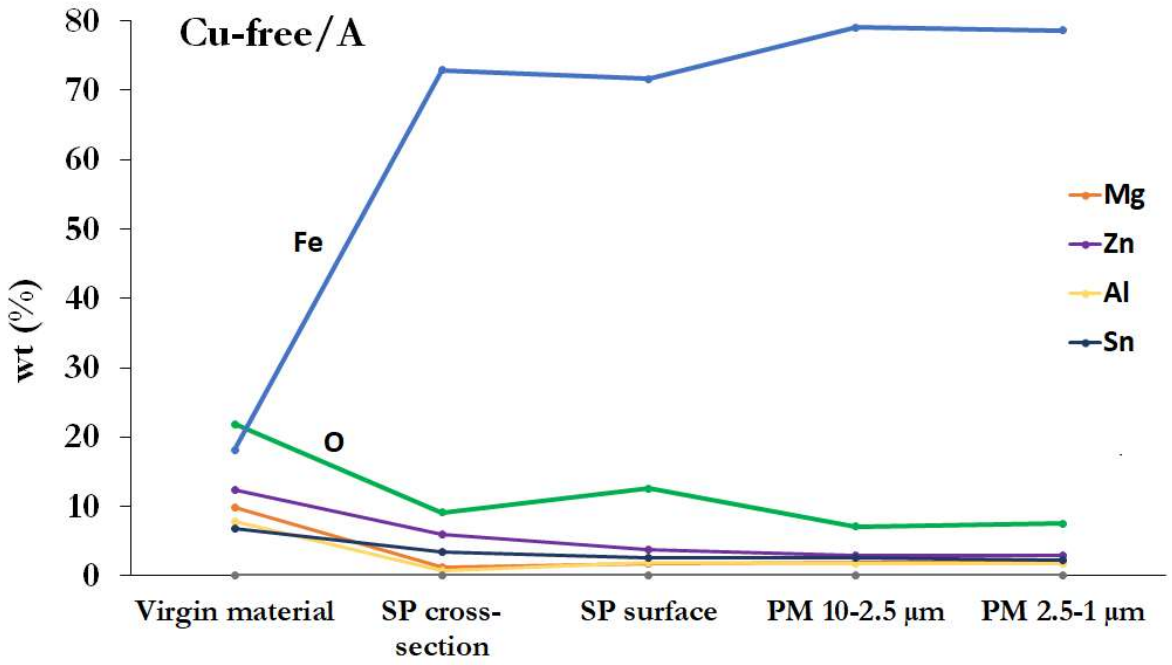

Figure 8.8: Comparison of the compositional values of different regions (virgin material, secondary plateaus surface and cross section, airborne particles PM 10-2.5 µm and PM 2.5-1 µm) for Cu-free/A friction material.

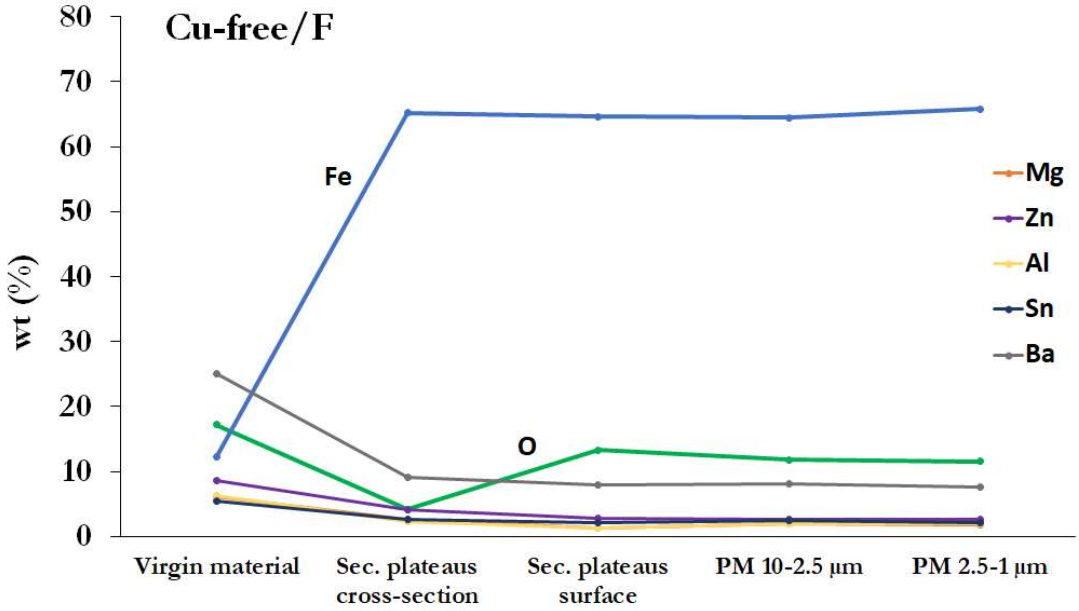

Figure 8.9: Comparison of the compositional values of different regions (virgin material, secondary plateaus surface and cross section, airborne particles PM 10-2.5 µm and PM 2.5-1 µm) for Cu-free/F friction material.

Based on the composition of the emitted particles (Table 8.4), it is possible to understand their formation mechanisms by comparing the obtained results. In Cu-free/A

friction material, the iron content in the produced particles (79.1 wt.%) is higher than the one recorded in both the inner (72.9 wt.%) and superficial portions (71.6 wt.%) of the secondary plateaus. Considering the corresponding trend of decrease in oxygen content (down to 7.1 wt.% from 9.1 wt.% and 12.6 wt.%, respectively), it suggests that the airborne particles contain more metallic iron than the secondary plateaus, especially when compared to the superficial secondary plateau. This indicates that, for the Cu-free/A friction material, the airborne particles originate mainly from the disruption of the secondary plateaus, but with a contribution also from the direct wear of the cast iron counterface. This latter mechanism is in line with the abrasive character of the Cu-free/A friction material. Instead, in case of Cu-free/F, the iron content in the particles emitted is nearly the same of its content in the friction layer (Figure 8.9), while the oxygen content is intermediate between the one of the external and the internal part of the plateaus. All these remarks indicate that most of the airborne particles come from the disruption of the friction layer, and in particular of its external parts. It is also important to reiterate that the iron content is significantly lower in the starting material composition due to the fact that it has not yet interacted with the cast iron disc.

8.5 Final comments

The tribological and the associated emission behavior of the two Cu-free friction materials are related to the characteristics of the friction layers that formed on the pin surfaces during PoD sliding tests.

The higher iron content in the PM emissions than in its secondary plateaus, forming on the surface of the Cu-free/A friction material indicates that the airborne particles come not only from the disruption of the secondary plateaus but also from the wear of the cast iron disc, through a direct wear induced by the abrasives present in this friction material. In case of Cu-free/F instead, the airborne particles are mainly fragments coming from the disruption of the friction layer, as proved by the corresponding composition of the emitted particles and secondary plateaus.

The in-depth characterization of the friction layer reveals that the outer surface layer of the secondary plateaus is more oxidized than internal part, being also more similar to the elemental composition of the emitted particles.

Chapter 9

PM brake emissions from a simplified friction material composition containing rice husk

This chapter aims at investigating the effect of an addition of rice husk in a new eco-friendly Cu-free brake pad composition, focusing on the tribological and emissions behavior. Rice husk (RH) is an abundant agricultural industry waste containing a relatively large amount of amorphous silica (a-SiO2), which should display abrasive properties that are not easily found in other natural materials.

Several natural ingredients have been proposed as sustainable raw materials to be used in brake pad formulations, like: hemp fibers, flax, kenaf, jute fibers, and palm kernel, just to mention the most popular ones [4-6]. In general, these lignocellulosic materials are intended to replace reinforcement fibers or simply to act as fillers, in the general perspective of using renewable ingredients, less harmful once emitted in the atmosphere. A drawback commonly displayed by the natural ingredients is attributed to the absorption of water and to the hydrophilic nature, that weakens the interface between the ingredient bundles and the lignin matrix [9]. In this regard, the ash of RH, i.e., its inorganic compound was added to one of the compositions investigated in the present study. To obtain the ash from RH, a controlled heat treatment was carried out, following specific literature indications [119-121].

It is important to highlight that the friction material formulations used in this part of the study have been developed with the deliberate intention to carry out laboratory tests for the assessment of the role of RH on the tribological and emission performances of friction materials.

This study was developed in collaboration with the University of Rio Grande do Sul, in Brazil, and part of the results was published in [129].

9.1 Characterization of the friction materials

Three non-commercial friction materials were studied. Two formulations contain 6 wt.% of RH, added in two different conditions: one after grinding, codenamed F-RH, and the other after grinding and heat treatment, called F-RHT. The third formulation contains

alumina (an abrasive) in the place of RH, still with a 6 wt.% concentration (F-AL). The grinding and heat treatment preparation of the RH are described in detail in Section 6.2.2.1.

The SEM micrographs of the microstructure of the three friction materials after pin preparation is shown by Figure 9.1, with the indication of the main components, identified through EDXS analyses. It can be appreciated the presence of metallic fibers (steel wool) and powders (barite, magnesium and calcium carbonate, aluminum oxide for F-AL and rice husk for F-RH and F-RHT).

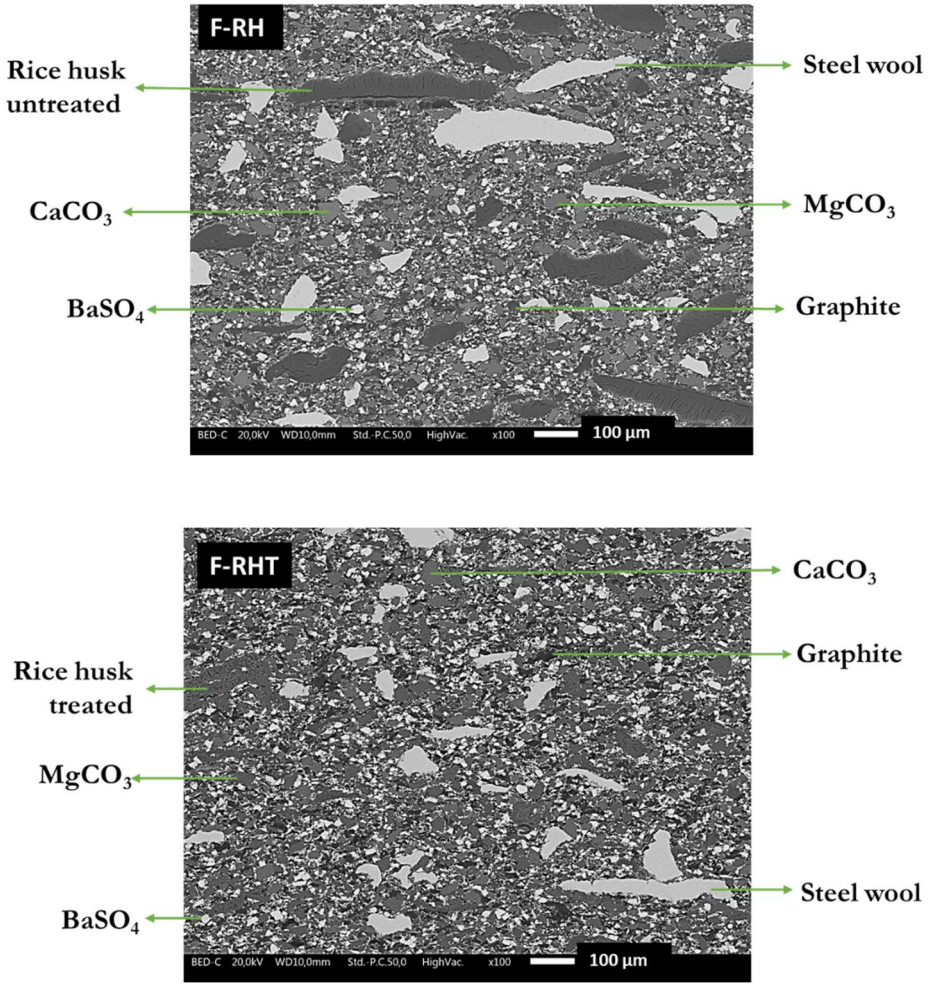

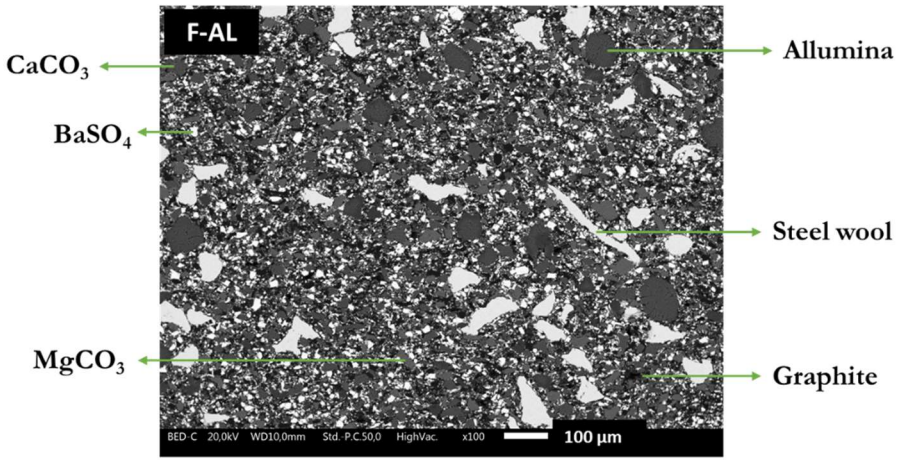

Figure 9.1: SEM micrographs for the F-RH, F-RHT and F-AL formulations, after pin preparation, with the identification of the main components, based on the indications of the EDXS map results [129].

The elemental compositions of the three materials are given Table 9.1, in which a rather higher amount of Si can be appreciated for F-RHT compared to F-RH. As expected, aluminum was detected in the F-AL material.

Table 9.1: Elemental composition of F-RH, F-RHT and F-AL formulations, obtained by EDXS analyses. Carbon was not considered.

Element (wt.%)	F-RH	F-RHT	F-AL
O	27.5 ±0.2	27.8 ±1.0	25.0 ±0.2
Mg	3.0 ±0.0	3.7 ±0.1	2.2 ±0.0
Al	-	-	2.8 ±0.1
Si	2.2 ±0.2	6.2 ±1.0	-
S	6.0 ±0.5	6.1 ±0.1	4.7 ±0.5
Ca	14.6 ±0.3	11.8 ±0.3	14.5 ±0.7
Fe	14.3 ±0.4	13.8 ±0.6	15.7 ±0.5
Ba	32.5 ±0.2	30.6 ±0.3	35.0 ±0.8

9.2 Tribological and emissions behavior

The evolution of both friction coefficient and the total concentration of emissions from representative PoD tests conducted on F-RH, F-RHT and F-AL is given in Figure 9.2. A rather unstable friction coefficient curves are observed for all three materials, which is coherent with the fact that the materials not comprise complex and optimized formulations, as commercial friction materials.

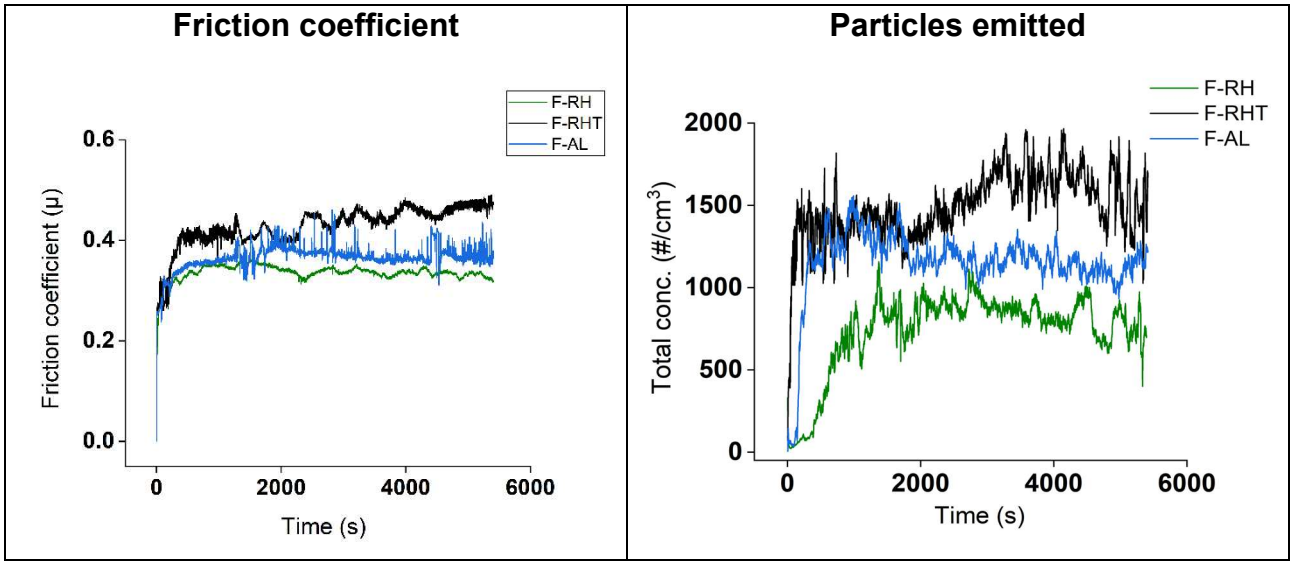

Figure 9.2: Evolution of friction coefficient and total concentration of particles emitted from representative tests conducted on the three materials.

Figure 9.3a shows the mean values of the friction coefficient for the steady state regime of the PoD tests. The F-RHT material yields the highest friction coefficient (0.45 ±0.03), followed by F-AL (0.39 ±0.03) and F-RH (0.37 ±0.02). The emissions display same raking: F-RHT yields highest value (1553 ±268), followed by F-AL (1164 ±196) and F-RH (715 ±122).

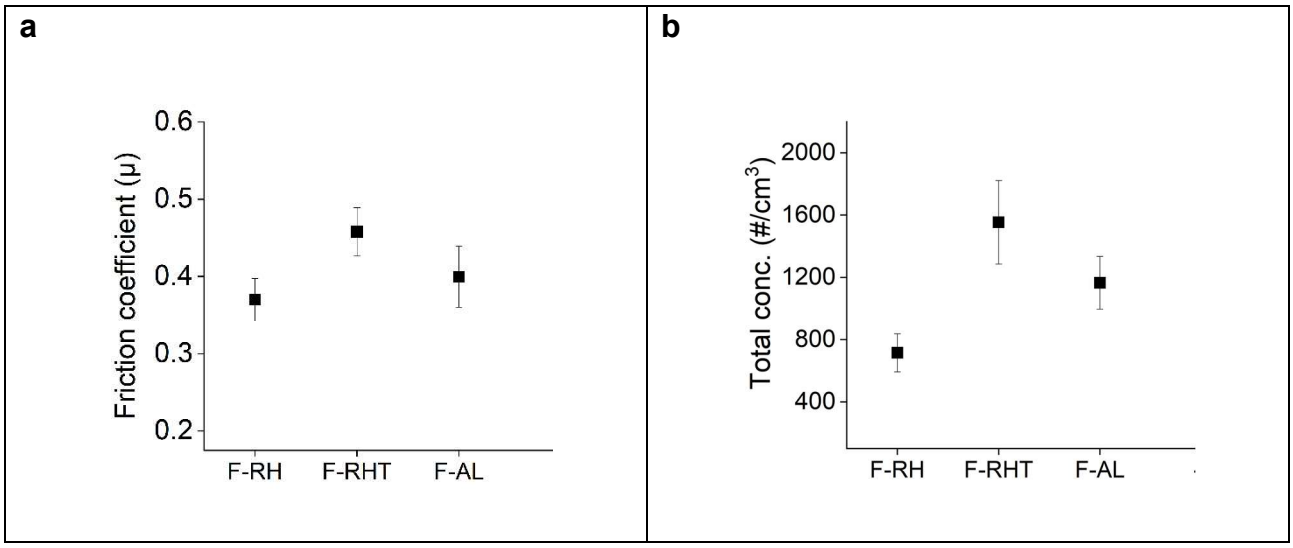

Figure 9.3: Mean values of (a) friction coefficient and (b) total concentration of emitted particles at steady-state for F-RH, F-RHT and F-AL materials.

Figure 9.4 shows the mean values of specific wear coefficient (Ka) of the pins. The Ka-values found for all three materials are typical of a mild wear regime [28]. F-RHT and F-AL display close values and F-RH exhibited the lowest one. This suggests that F-RH showed the best wear resistance among all the three formulations selected in this investigation.

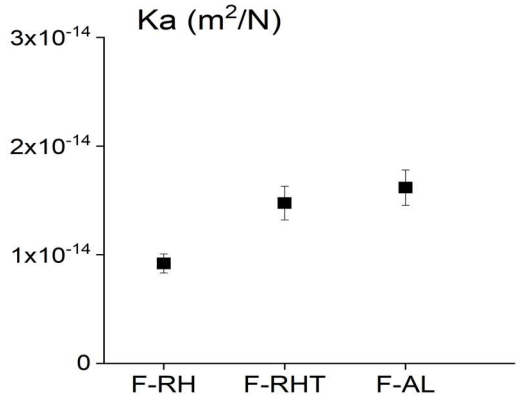

Figure 9.4: Mean values of pin's wear coefficient (Ka) for three materials.

9.3 Characterization of the pins and discs worn surfaces

The characteristics of the friction layers present on the pins' worn surfaces after the PoD tests are shown by the SEM micrographs in Figure 9.5. It is evident that F-RHT could easily form secondary contact plateaus, displaying a larger fraction of the surface covered by patches of compacted debris, compared to F-RH and F-AL. Another important

observation in case of F-RHT concerns the formation of the secondary plateaus without the contribution of steel wool fibers as primary plateaus for supporting them (highlighted by red circle in Fig. 9.5). Just a few, smaller regions with this kind of plateaus can be appreciated in F-RH and F-AL materials. Furthermore, the presence of untreated RH particles can be also clearly recognized in F-RH material (highlighted by a blue circle).

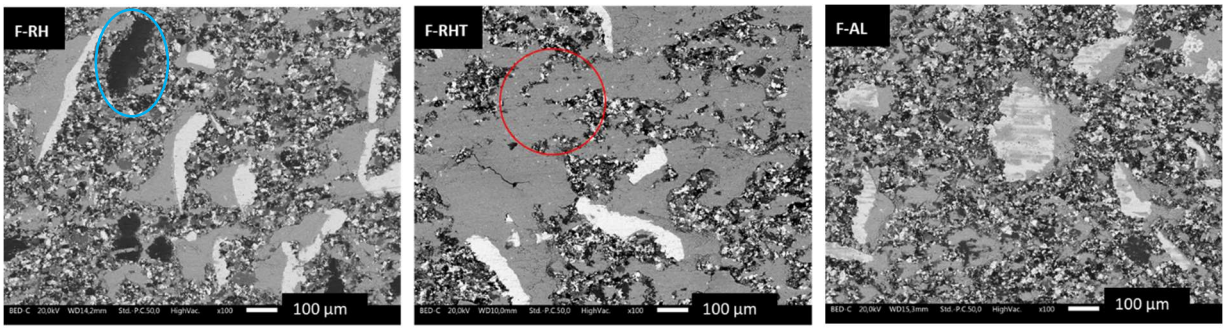

Figure 9.5: Pins' worn surfaces for F-RH, F-RHT and F-AL materials [129].

Figure 9.6 shows higher magnification images of the friction layer formed on pins' surfaces for the three materials. On the left side the images were obtained using backscattered electrons, whereas the corresponding SEM images at the right side were obtained using secondary electrons. The secondary plateaus of F-RH and F-RHT seems to be more compacted than F-AL. In addition, abrasive marks can be noticed in the steel wool of F-AL, which is not too evident for the other two materials.

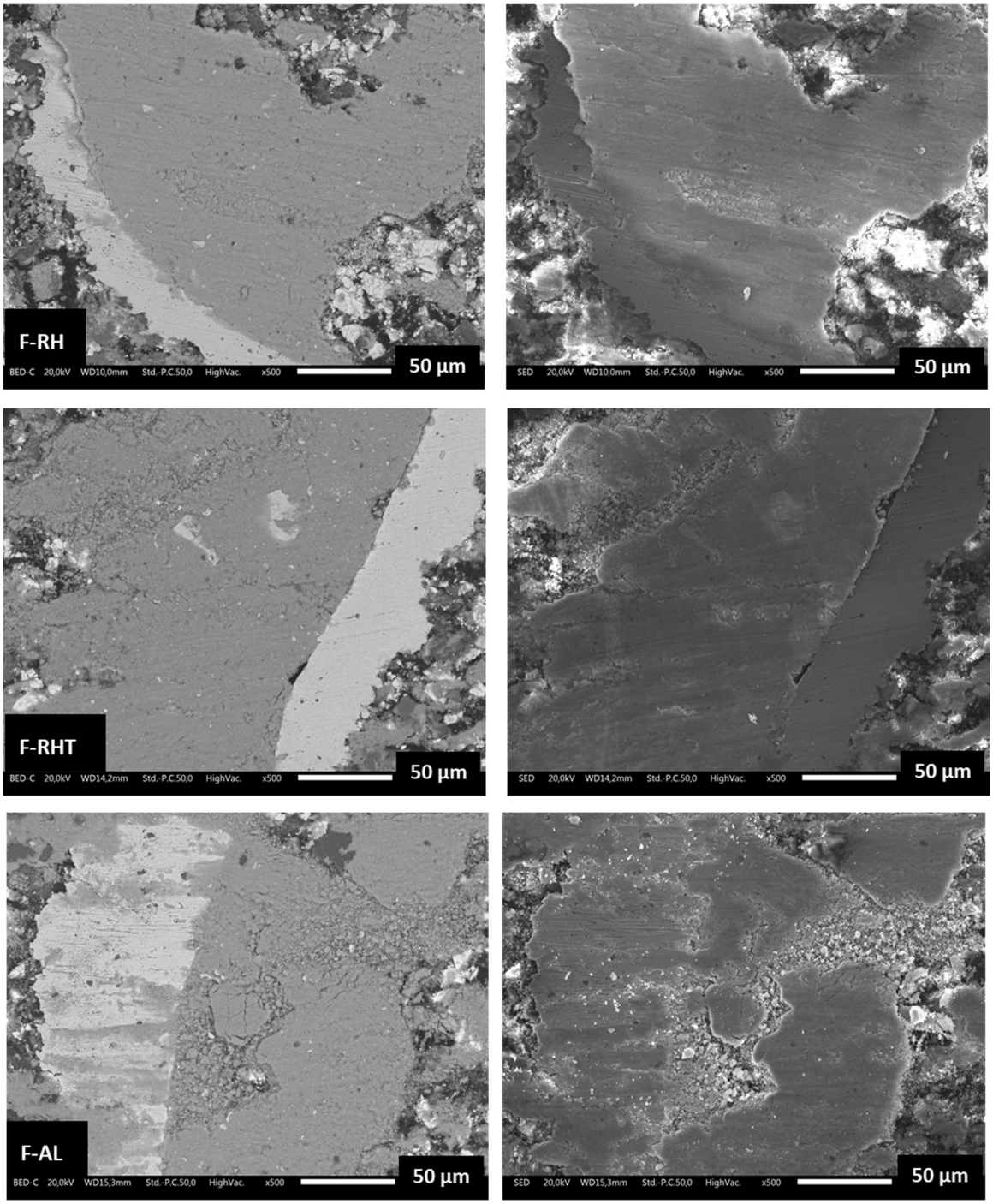

Figure 9.6: SEM micrographs of pins' worn surface for all friction materials. On left side: backscattered electrons. On right side: secondary electrons [129].

The elemental compositions of the secondary plateaus are given in Table 9.2. The results are mean values of tests acquired from three distinct regions of the secondary plateaus. The same set of elements found in the virgin materials (Table 9.1) can be observed, although in different concentrations. The secondary plateaus of all materials exhibited a higher iron concentration than the virgin pins, due to the contribution of the disc wear. In particular, the F-AL has secondary plateaus with the highest amount of iron, and

the lowest content of the other elements, like barium, calcium and sulfur. This suggests a higher contribution from the wear of the disc, which could be attributed to a more intense abrasive action of the alumina added to F-AL, as compared to the rice husk added to F-RH and F-RHT. The abrasive marks noticed on the iron fibers in Figure 9.6 for the material F-AL also suggest the more abrasive character displayed by this material.

Table 9.2: Elemental composition of secondary plateaus of F-RH, F-RHT and F-AL analyzed on the surface top view.

Element (wt.%)	**F-RH**	**F-RHT**	**F-AL**
Fe	34.1 ±1.6	30.0 ±0.1	41.1 ±0.3
Mg	1.5 ±0.2	2.0 ±0.2	1.3 ±0.2
Al	-	-	2.3 ±0.0
Si	1.2 ±0.1	2.1 ±0.1	-
S	4.3 ±0.3	4.5 ±0.2	3.1 ±0.1
Ca	6.2 ±0.2	7.2 ±0.3	4.4 ±0.5
Ba	16.1 ±1.1	17.3 ±0.9	12.5 ±0.1
O	36.7 ±0.3	36.9 ±0.1	35.4 ±0.6

Figure 9.7 shows the disc's worn surface after testing against the F-RH and F-AL pins, respectively. In both cases, the surface damage by sliding wear is rather limited. However, abrasive scratches can be noticed for F-AL (they are indicated with a yellow arrow), not evident in case of F-RH. This observation confirms the more intense abrasive action displayed by the alumina present on F-AL. The disc's worn surface after sliding against F-RHT is similar to that shown in case of F-RH and it is then not included.

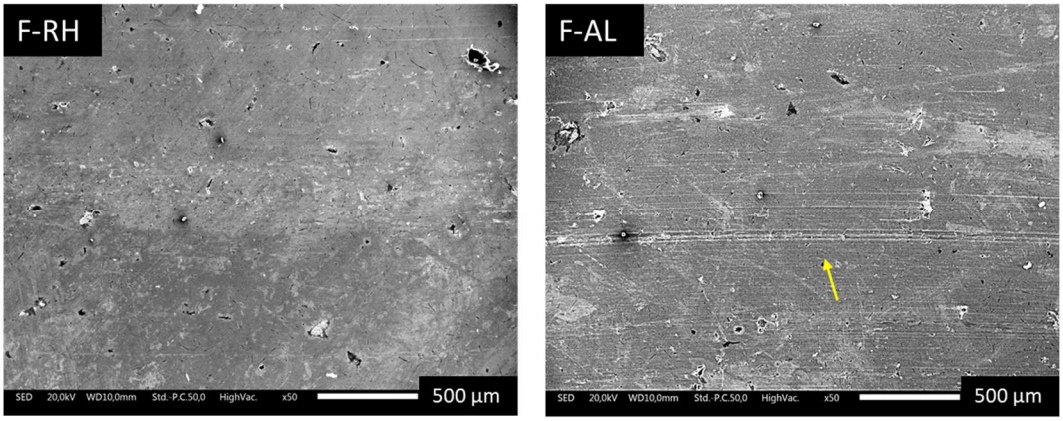

Figure 9.7: SEM micrographs showing the disc wear traces after sliding against F-RH and F-AL. The yellow arrow indicates some abrasive scratches [129].

The cross-sectional microstructure of the worn pins is given in Figure 9.8. A very thin secondary plateaus is noticed in all cases. However, in agreement with the planar observations (Fig. 9.5), the F-RHT features better quality secondary plateaus compared to the other two materials. From the micrographs shown in Figure 9.5, the F-RH seems to form better secondary plateaus than F-AL. However, as results from the cross-sectional observations, it turns out that F-RH secondary plateaus are very thin, and F-AL formed thicker ones.

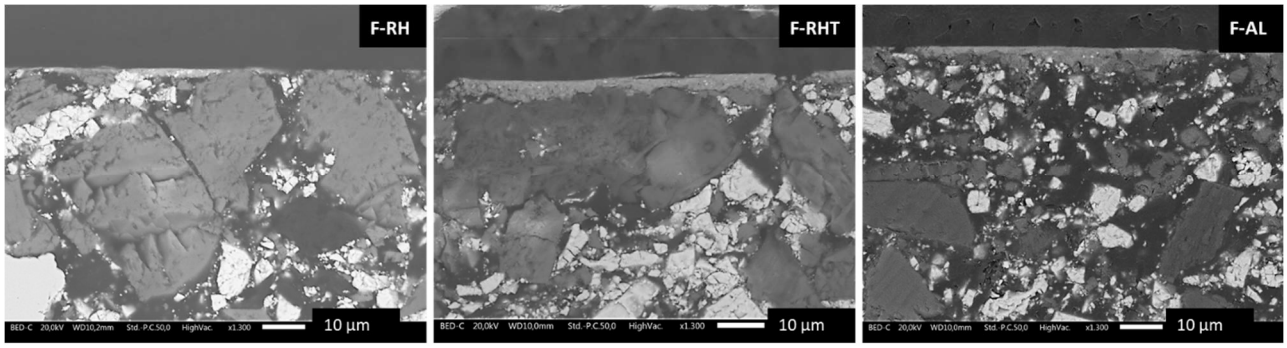

Figure 9.8: SEM micrographs of pin's cross-section for all friction materials.

The elemental composition of cross-section secondary plateaus for F-RH, F-RHT and F-AL are listed in Table 9.3. In comparison to the elemental composition of measured on the surface of the secondary plateaus (Table 9.2), it is noticed a higher iron content, and a correspondingly lower oxygen content, in the cross-section of the secondary plateaus for materials F-RH and F-AL. Same behavior was observed in the previous chapter and suggests that oxygen gradient is mainly due to the oxidation of metallic iron present close to the wear surface by the surrounding environment and tribological test conditions. In F-

RHT the picture is different; the iron content is comparatively lower than for the top view of the secondary plateaus. The higher amount of Ba, Ca and O on F-RHT compared to the other two materials, and correspondently lower amount of Fe, indicates that the internal portion of the secondary plateaus is formed to a larger extent of debris of barite and other ingredients of the friction material.

Table 9.3: Elemental composition of secondary plateaus of F-RH, F-RHT and F-AL analyzed on the cross-section.

Element (wt.%)	**F-RH**	**F-RHT**	**F-AL**
Fe	42.6 ±0.6	22.8 ±2.3	51.6 ±1.7
Mg	1.4 ±0.1	2.4 ±1.2	1.9 ±0.8
Al	-	-	3.4 ±0.7
Si	0.8 ±0.3	2.7 ±0.7	-
S	2.8 ±0.3	4.9 ±1.0	2.9 ±0.8
Ca	8.2 ±0.6	11.4 ±2.0	4.1 ±1.3
Ba	18.9 ±1.0	26.7 ±2.6	13.0 ±0.9
O	25.4 ±1.1	29.3 ±3.4	23.3 ±1.1

Figures 9.9 to 9.11 show the cross-sections and the corresponding EDXS maps of the worn pins at the end of the tests for all materials. Considering the sliding direction, the secondary plateaus are generally formed in front of the steel fibers (primary plateaus). The fibers act as barriers where wear debris pile up and get compacted by the combined action of pressure and frictional heating. This is the case of material F-RH, as seen in Fig. 9.9 and confirmed by Fig. 9.6. Comparatively large alumina particles, and occasionally barite, were also found to play a similar role, as primary plateaus in case of F-AL (see Fig. 9.11). However, in case of material F-RHT, the picture is different since several secondary plateaus do not form near the primary plateaus (indicated by red circle in Fig. 9.5). The inspection of the cross sections revealed that most of the secondary plateaus were formed on the top of treated RH particles (see Fig. 9.10). Particles of treated RH supporting the secondary plateaus were found in several other points during the inspection of the cross-

section of F-RHT. On the other hand, in case of F-RH, no particle of untreated RH was observed playing the same role.

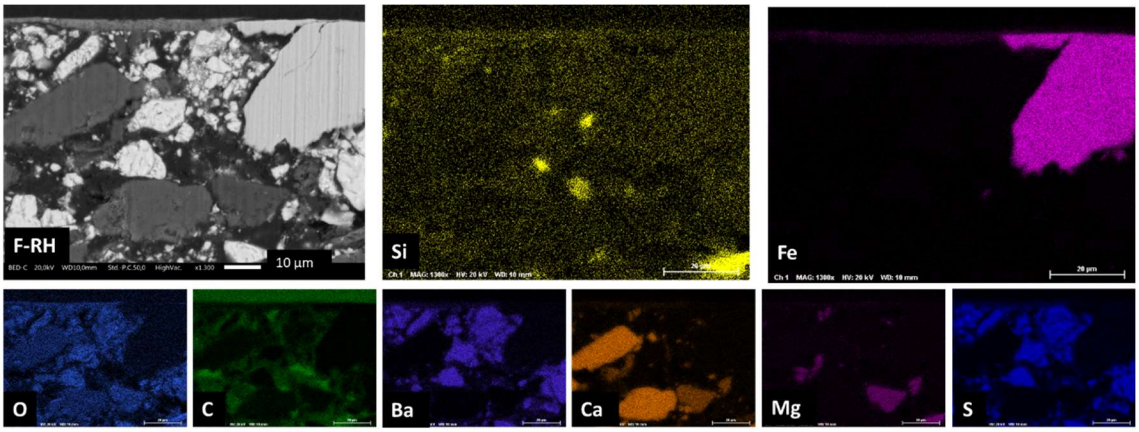

Figure 9.9: SEM micrograph and corresponding EDXS elemental maps of the cross-section of an F-RH pin [129].

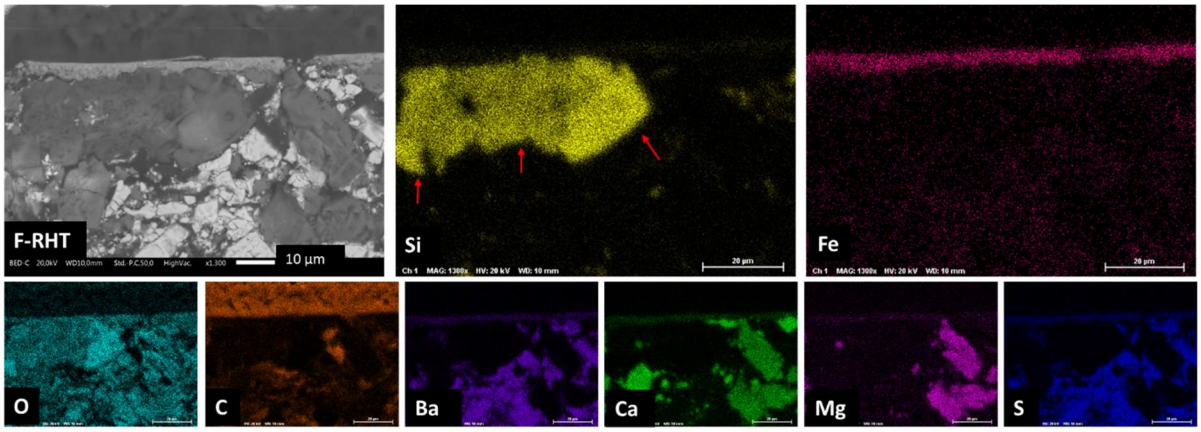

Figure 9.10: SEM micrograph and corresponding EDXS elemental maps of the cross-section of an F-RHT pin. The red arrows in the Si map indicate the treated RH particle with the secondary plateaus on the top of it [129].

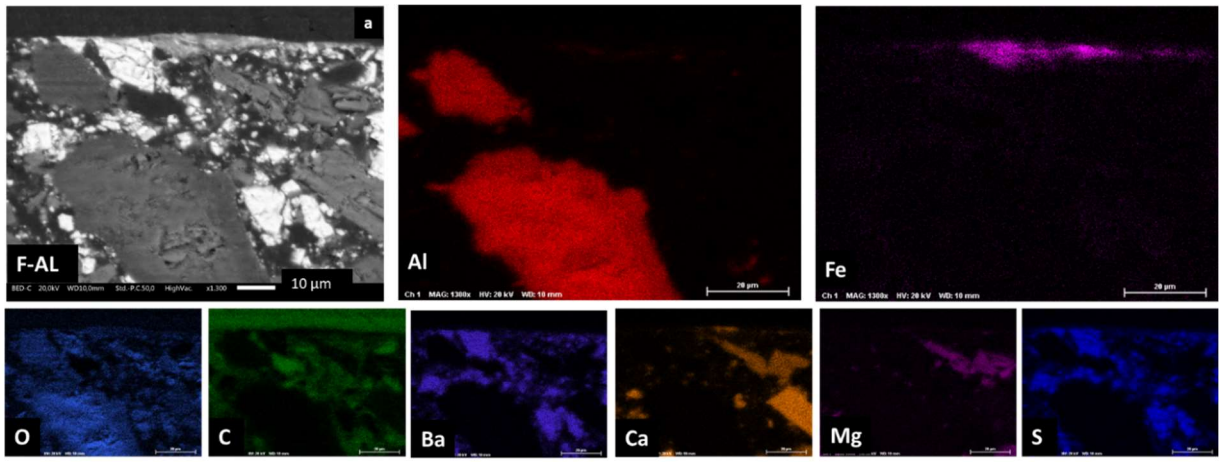

Figure 9.11: SEM micrograph (a) and corresponding EDXS elemental maps of the cross-section of an F-AL pin [129].

Figure 9.12 shows the SEM micrograph and its corresponding EDXS map of Si on the worn surface top view of F-RHT. It is noticed that the secondary plateaus without the usual iron fibers as primary plateaus observed in Fig 9.5 (highlighted by the red circle) are in fact supported by particles of treated RH (see red arrows).

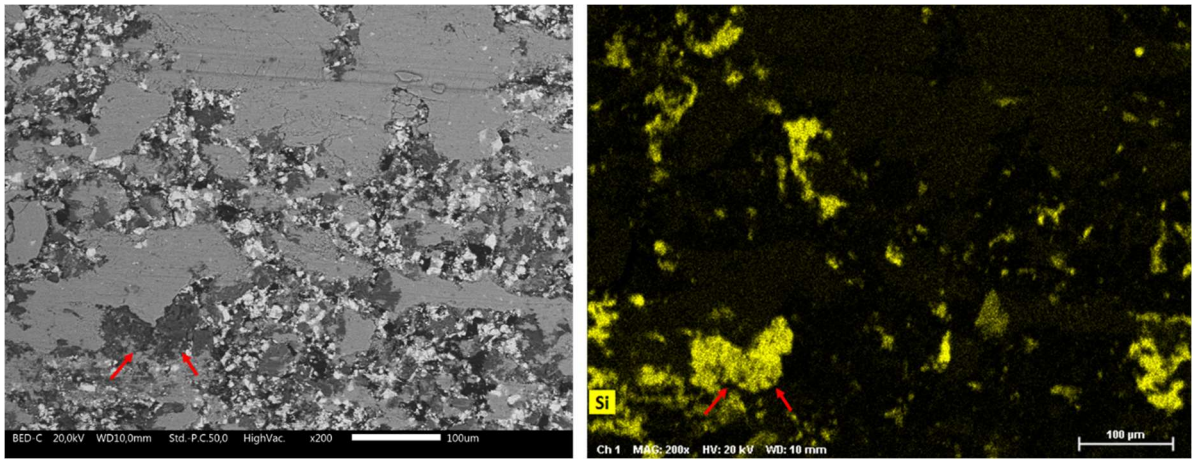

Figure 9.12: SEM micrograph and its corresponding EDXS map of Si on the worn surface top view of F-RHT. The red arrows indicate the particle of RH supporting the secondary plateaus.

The particle of heat-treated rice husk (RHT), shown already in Figure 6.2(d), are shown for an easy discussion in Figure 9.13. A porous structure can be appreciated. Recent studies [30,31] have reported that porous compounds, containing nest-like structures (e.g., mineral fibers), favor the formation of secondary plateaus without the need of primary plateaus. This is explained by the ability of these nests to trap and accumulate small particles, thus behaving as a sort of reservoir of particles, which are thereby compacted by sliding and pressure, and relevant temperature raise.

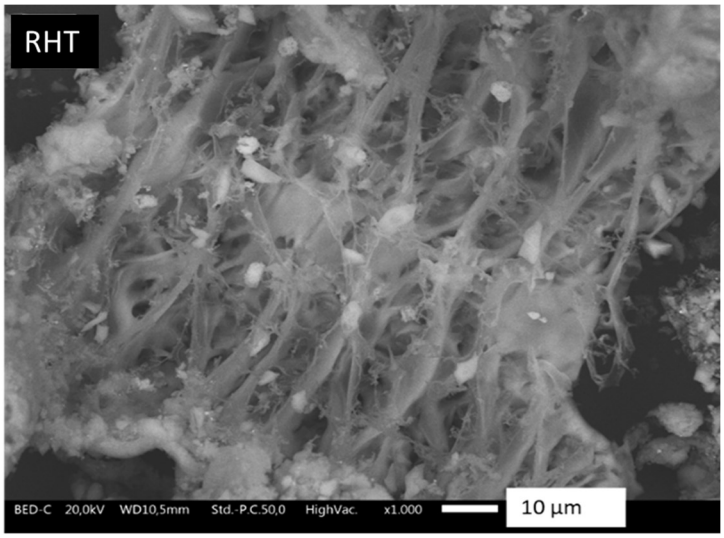

Figure 9.13: SEM micrograph of a particle of treated rice husk (RHT) [129].

9.4 Characterization of the PM emissions

Figure 9.14 and 9.15 shows the SEM micrographs of airborne PM emissions for F-RH, F-RHT and F-AL, collected by the impactor and sizing from 2.5–10 and 2.5–1 µm, respectively. It is observed that the morphology of the airborne particles for all materials seems quite similar, showing predominantly coarse flake-shaped debris.

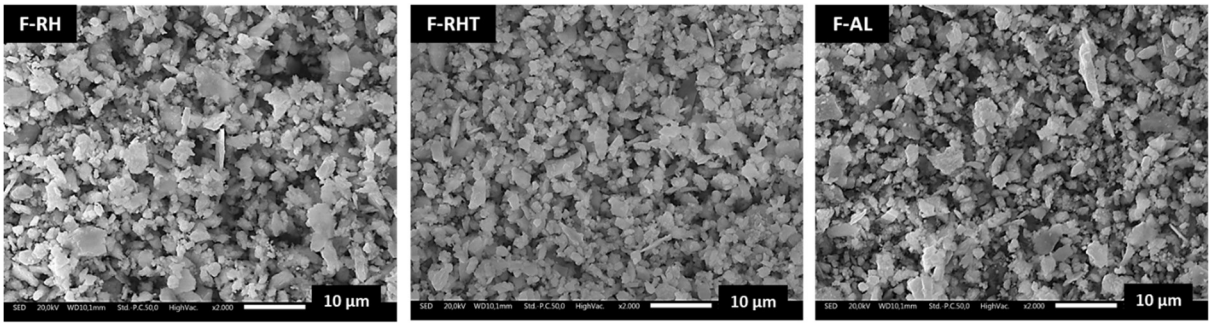

Figure 9.14: SEM micrograph of the airborne particles with aerodynamic diameter range of 10 - 2.5 µm for F-RH, F-RHT and F-AL.

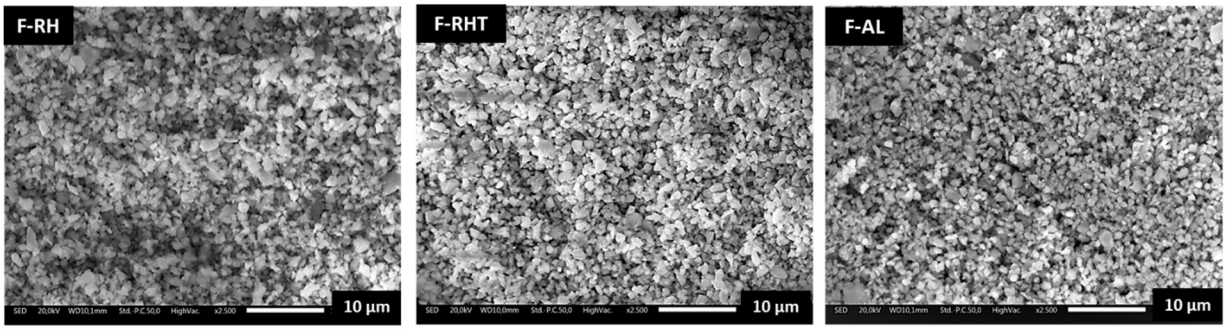

Figure 9.15: SEM micrograph of the airborne particles with aerodynamic diameter range of 2.5 - 1 µm for F-RH, F-RHT and F-AL [129].

The elemental composition of the airborne particles, sizing 10 - 2.5 µm and 2.5 - 1 µm, are shown in Table 9.4 and 9.5, respectively. The results are mean values from three distinct full frame analysis in low magnification for each material.

Table 9.4: Elemental composition of airborne particles with size from 10 to 2.5 µm for F-RH, F-RHT and F-AL materials.

Element (wt.%)	**F-RH**	**F-RHT**	**F-AL**
Fe	37.4 ±0.1	27.7 ±0.6	37.3 ±0.4
Mg	1.9 ±0.1	2.3 ±0.1	1.5 ±0.0
Al	-	-	3.3 ±0.1
Si	1.4 ±0.1	2.9 ±0.1	-
S	4.3 ±0.3	5.2 ±1.0	3.8 ±0.1
Ca	6.7 ±0.0	8.1 ±0.1	5.4 ±0.1
Ba	16.0 ±1.6	19.6 ±0.0	15.1 ±0.3
O	32.3 ±2.0	34.4 ±0.6	33.9 ±0.1

Table 9.5: Elemental composition of airborne particles with size from 2.5 to 1 μm for F-RH, F-RHT and F-AL materials.

Element (wt.%)	F-RH	F-RHT	F-AL
Fe	32.6 ±0.1	25.6 ±0.2	37.5 ±0.1
Mg	1.9 ±0.1	2.2 ±0.0	1.4 ±0.1
Al	-	-	3.5 ±0.3
Si	1.8 ±0.1	3.1 ±0.6	-
S	4.1 ±0.0	4.9 ±0.1	4.0 ±0.4
Ca	6.3 ±0.1	7.8 ±0.2	5.1 ±0.1
Ba	15.7 ±0.4	19.3 ±0.3	15.1 ±0.5
O	37.7 ±0.5	37.3 ±0.1	33.3 ±1.1

To allow a better comparison, Figure 9.16 shows an overview graph of the compositions of the virgin friction material, of the secondary plateaus (for both the cross-section and the surface analyses), and of the collected airborne particles in different sizes. It is seen that in all cases, the composition of the airborne particles is by all means compatible with that of the secondary plateaus surface, showing that most of the airborne particles originate from the disruption of these regions formed on the pin surface during PoD tests. To back this idea is the flake-like morphology of the collected particles (Figg. 9.14, 9.15).

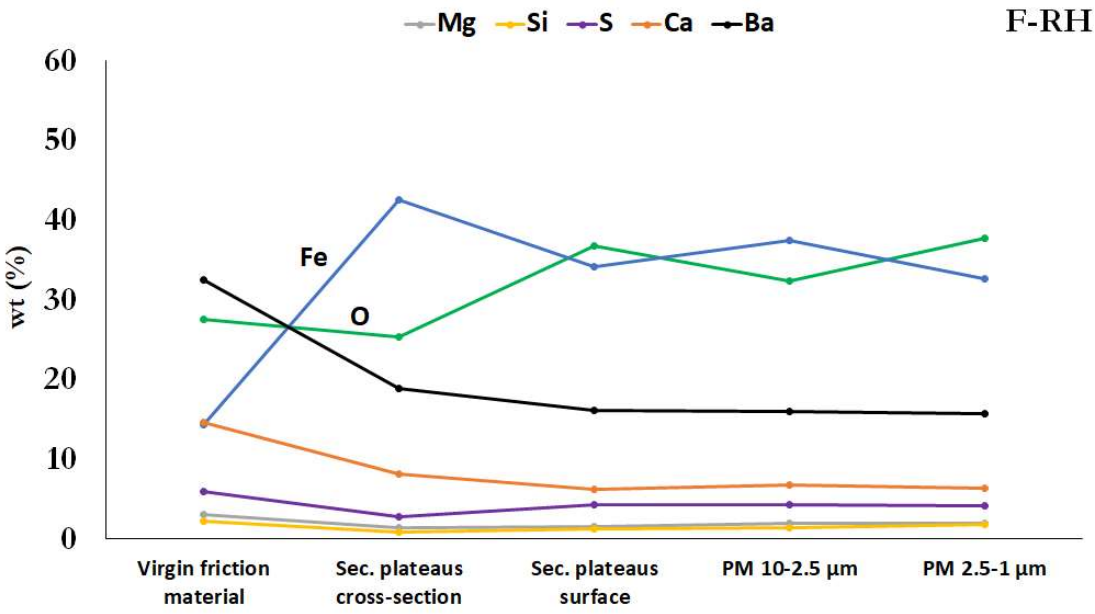
F-RH
Mg
Si
S
Ca
Ba
wt (%)
60
50
40
30
20
10
0
Fe
O
Virgin friction material
Sec. plateaus cross-section
Sec. plateaus surface
PM 10-2.5 µm
PM 2.5-1 µm

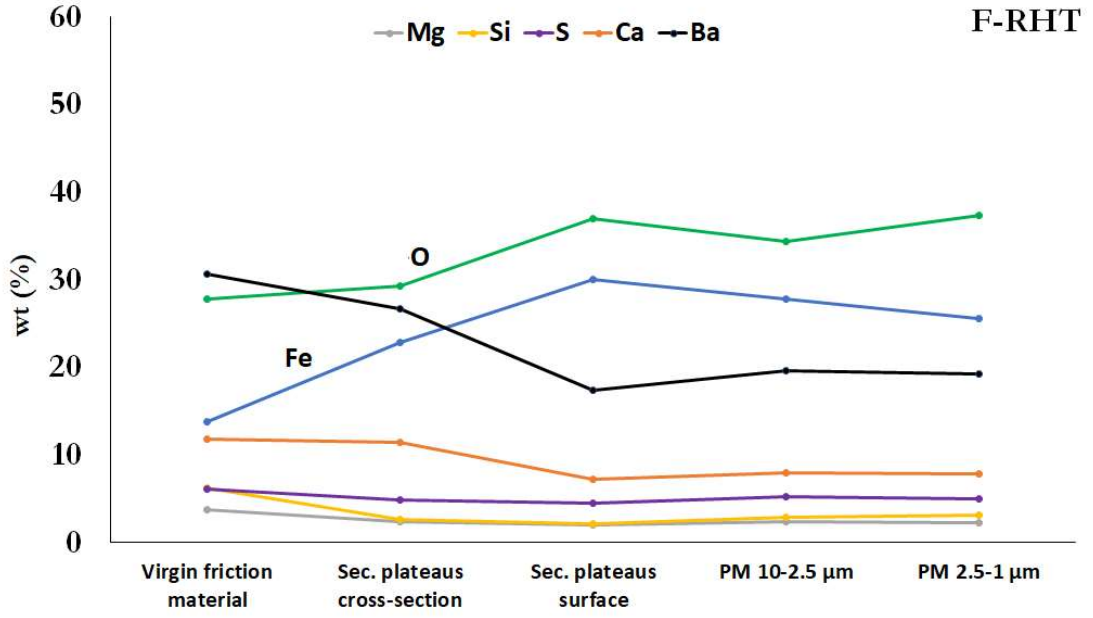
F-RHT
Mg
Si
S
Ca
Ba
wt (%)
60
50
40
30
20
10
0
O
Fe
Virgin friction material
Sec. plateaus cross-section
Sec. plateaus surface
PM 10-2.5 µm
PM 2.5-1 µm

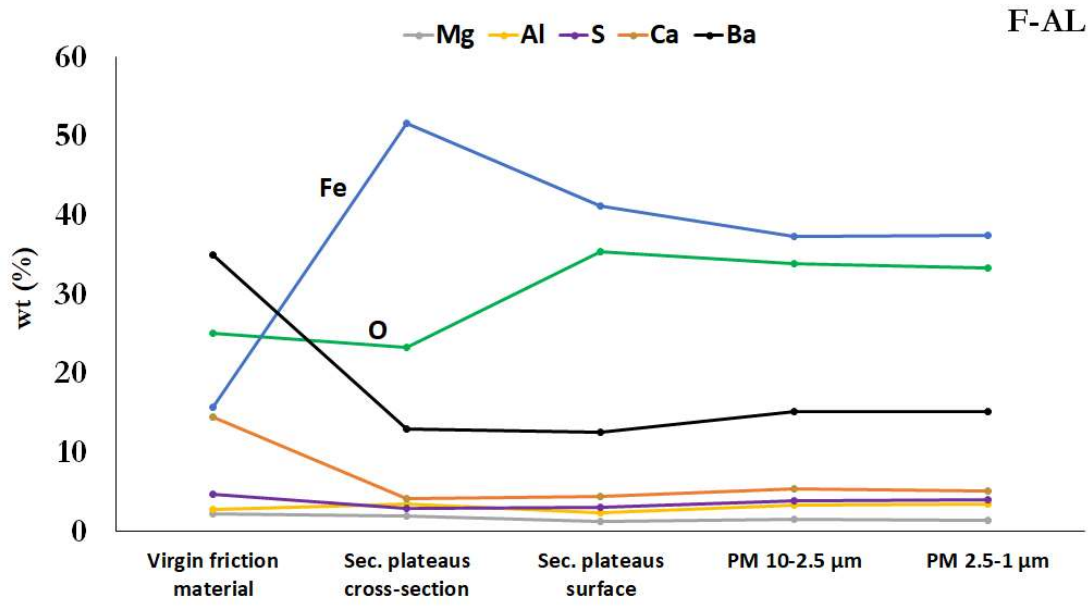

Figure 9.16: Comparison of the compositional amount for the virgin friction material, secondary plateaus (Sec plateaus) and emitted particulate matter (PM) for each one of the friction materials [129].

9.5 Final comments

In comparison with F-AL, both friction materials containing rice husk have shown promising properties: F-RH featured a comparable friction coefficient, and a lower wear rate and airborne PM emission. F-RHT showed a higher friction coefficient, comparable wear rate and better quality of the friction layer on worn surfaces, featuring a high relative fraction of secondary plateaus without primary plateaus. The larger areas of secondary plateaus formed on F-RHT without primary plateaus is due to the structure of the heat-treated rice husk, which acts as a sort of reservoir of wear debris, supporting all those particles on the top of it. All these remarks rank rice husk as an interesting natural ingredient for brake pad materials, which should be more intensively explored, particularly as concerns its abrasive role.

The similar elemental composition of secondary plateaus and PM emissions, as well as the morphology of the particles indicate that the tribo-oxidative wear is the main mechanism of particles generation. The larger amount of emissions and the corresponding higher covered area displayed by the secondary plateaus in case of F-RHT support this statement.

Chapter 10

Final discussion

This thesis aimed at investigating the coarse and fine PM brake emissions, corresponding to particles from 10 to 1µm, originated during PoD test from the relevant tribological contact, occurring below the critical temperature, i.e., the decomposition temperature of the organic matrix of the friction material. The tests parameters applied correspond to mild sliding conditions resembling those faced in real braking. Such conditions are characteristic of driving in urban areas, where the expose to traffic PM is concentrated.

The main objective of this thesis was the study of the PM formation mechanism. To achieve this goal, three investigations were conducted, as specified in Figure 10.1.

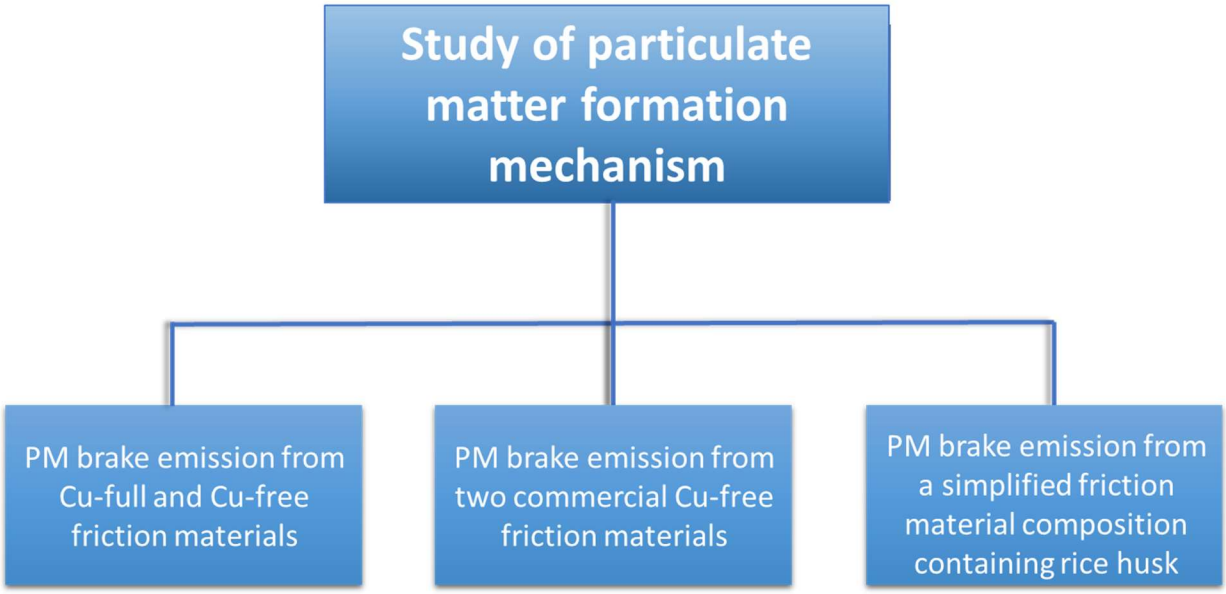

Figure 10.1: Scheme of the experimental part of this thesis.

As discussed in Section 2.2, different wear mechanisms can be present in a tribological system. By the investigations conducted in this thesis, using commercial and non-commercial low-metallic friction materials against cast iron disc, it was possible to identify the origin of these kind of particles emission: triboxidative wear was found as the main mechanism. It happens by the disruption of the friction layer (primary and secondary plateaus) continuously formed on the mating surfaces during the sliding contact. The evidence supporting this conclusion are:

- The very similar elemental composition between the secondary plateaus and emissions detected in all three investigations,
- The flake-like shaped morphology feature by most of particles, indicating its origin from mechanical process,
- The flat surface displayed by many particles, indicating they came from contact region, i.e., the contact plateaus,
- The sliding marks identified in a single particle, confirming it came from contact region,
- The corresponding behavior between the friction coefficient and the emissions; both are affected by the friction layer formed on mating surfaces.

It was also observed that particles produced by abrasive wear of the disc can be directly emitted to the environment. This generation mechanism seems to be more active for friction materials containing a relative higher content of abrasives in its formulation.

Single ingredients from regions not coverage by the friction layer may also leave for the environment. However, the single ingredients typically have larger size, thus they would immediately fall on the ground. In addition, the direct emission of coarse fragments of the original ingredients is not that frequent.

Based on these conclusions, some strategies are proposed for the reduction of the PM brake emissions:

- **Proper content of abrasives:** the abrasives are primordial ingredients of the friction materials, playing an important role in increasing the friction coefficient and supplying iron from the disc to the well-formation of the friction layers. However, its content must be optimized since the particles generate by its action may are directly emitted to the environment.
- **Proper adhesion of the secondary plateaus on the bulk material:** poor adhesion between secondary plateaus and bulk material can lead a high disruption rate of the secondary plateaus, and consequently, higher emissions. The content of ingredients with low surface energy, such as graphite, must be optimized.
- **Proper iron-oxides content on secondary plateaus**: as discussed in Section 4.1**,** the formation of surface oxides layers on the secondary plateaus promotes a wear protective action. However, an excessive content iron-oxide particles in the secondary plateaus increases the adhesive forces at the

contact interface, increasing the friction coefficient and associated increasing in probability of the emissions from the disruption of the friction layer.

References

[1] Straffelini, *Friction and Wear Methodologies for Design and Control*, Switzerland: Springer Verlag, 2015.

[2] K. L. Johnson, *Contact Mechanics*, Cambridge University Press, Cambridge, 1985.

[3] E. Rabinowicz, *The Nature of the Static and Kinetic Coefficients of Friction. J*ournal of Applied Physics 22, no. 11, 1373–1379, 1951.

[4] I. M. Hutchings, *Tribology*, ed. by Edwald Arnold, London, 1992.

[5] P.J. Blau, *Friction Science and Technology*, Marcel Dekker Inc., New York, 1996.

[6] M. Avlonitis and K. Kalaitzidou, *Estimating the real contact area between sliding surfaces by means of a modified ofc model*, Archives of Civil and Mechanical Engineering, vol. 15, no. 2, 355–360, 2015.

[7] M. Nosonovsky and B. Bhushan, *Multiscale friction mechanisms and hierarchical surfaces in nano- and bio-tribology*, Mater. Sci. Eng. R Reports. 58,162–193, 2007.

[8] K.H. Zum Gahr, *Microstructure and Wear of Materials*, 1st ed., Tribology Series, Elsevier, Institute of Materials Technology, University of Siqen, 1987.

[9] M. Khruschov, *Principles of abrasive wear*, Wear 28 69–88,1974.

[10] A. Akimasa, W. Barkmeier, R. Erickson, K. Nojiri, T. Takamizawa, M. Latta, M. Miazaki, N. Fischer, *Wear of resin composites: Current insights into underlying mechanisms, evaluation methods and influential factors*, Japanese Dental Science Review, vol. 54, 76–87, 2017.

[11] P.C. Verma, *Automotive Brake Materials: Characterization of Wear Products and Relevant Mechanisms at High Temperature,* Doctoral thesis, 2016.

[12] F.E. Kennedy, *Thermal and thermomechanical effects in dry sliding,* Wear vol. 100, 453–476, 1984.

[13] M.F. Ashby, J. Abulawi, H.S. Kong, *Temperature Maps for Frictional Heating in Dry Sliding*, Tribology Transactions, 34, 577–587,1991.

[14] J. Bijwe, P.V. Gurunath, *Friction and wear studies on brake-pad materials based on newly developed resin*, Wear 263, 1212–1219, 2007.

[15] A.E. Anderson, *Friction and wear of automotive brakes*, ASM Handbook 18, 569–577 1992.

[16] P.C. Verma, R. Ciudin, A. Bonfanti, P. Aswath, G. Straffelini and S. Gialanella. *Role of the friction layer in the high-temperature pin-on-disc study of a brake material.* Wear vol. 346-347, 56–65, 2016.

[17] L.Y. Barros, J.C. Poletto, D. Buneder, P.D. Neis, N.F. Ferreira, R.P. Pavlak and L.T. Matozo. *Effect of pressure in the transition between moderate and severe wear regimes in brake friction materials,* Wear vol. 438-439, 203112, 2019.

[18] L. Maines and G. Straffelini, *The relationship between wear of semi-metallic friction materials and pearlitic cast iron in dry sliding,* Wear vol. 307, 75–80, 2013.

[19] R. Renz, G. Seifert and W. Krenkel, *Integration of CMC Brake Disks in Automotive Brake Systems*, International Journal of Applied Ceramic Technology, vol. 9, 712–724, 2012.

[20] D. Chan, G.W. Stachowiak, *Review of automotive brake friction materials,* Proceedings of the Institution of Mechanical Engineers. Part D J. Automob. Eng. 218, 953–966, 2004.

[21] M. Arman, S. Singhal, P. Chopra, M. Sarkar, *A review on material and wear analysis of automotive Break Pad*, Materials Today Proceedings, vol. 5, 28305–28312, 2018.

[22] C. A. Aza, *Composites in Automotive Applications: Review on brake pads and discs*, University of Bistrol, 2014.

[23] P. Filip, L. Kovarik and M.A. Wright, *Automotive Brake Lining Characterization*, SAE Technical Paper 973024, 1997.

[24] W. Österle, C. Deutsch, T. Gradt, G. Orts-Gil, T. Schneider, A.I. Dmitriev, *Tribological Screening Tests for the Selection of Raw Materials for Automotive Brake Pad Formulations*, Tribology International vol. 73, 148–155, 2014.

[25] R.C. Dante, *Handbook of Friction Materials and their Applications*, Elsevier 1st edition, 2015.

[26] A.P.G. Nogueira, M. Leonardi, G. Straffelini and S. Gialanella, *Sliding Behavior and Particle Emission of Cu-free Friction Materials with Different Contents of Phenolic Resin*, Tribology Transactions,1–10, 2020.

[27] V.V. Kumar and S.S. Kumaran, *Friction material composite: types of brake friction material formulations and effects of various ingredients on brake performance–a review*, Materials Research Express vol. 6, 2019.

[28] M. Alemani, *Particle emissions from car brakes: the influence of contact conditions on the pad-rotor interface*, doctoral thesis, 2017.

[29] K.L. Sundarkrishnaa, *Friction Material Composites*, 2nd ed., Springer International Publishing, 2015.

[30] L. Wei, Y.S. Choy and C.S. Cheung, *A study of brake contact pairs under different friction conditions with respect to characteristics of brake pad surfaces.* Tribology International vol. 138, 99–110, 2019.

[31] U.S. Hong, S.L. Jung, K.H. Cho, M.H. Cho, S.J. Kim and H. Jang, *Wear mechanism of multiphase friction materials with different phenolic resin matrices*, Wear. Vol. 266, 739–744, 2009.

[32] L. Pilato, *Phenolic resins: 100 Years and still going strong*, Reactive Functional Polymers vol. 73, 270–277, 2013.

[33] M.H. Cho, S.J. Kim, D. Kim and H. Jang, *Effects of ingredients on tribological characteristics of a brake lining: an experimental case study*, Wear vol. 258,1682–1687, 2005.

[34] P.V. Gurunath, J. Bijwe, *Friction and wear studies on brake-pad materials based on newly developed resin*, Wear vol. 263, 1212–1219, 2007.

[35] D. Ratna, *Handbook of Thermoset Resins*, Elsevier ,2009.

[36] M. V. Alonso, M. Oliet, J.C. Domínguez, E. Rojo and F. Rodríguez, *Thermal degradation of lignin–phenol–formaldehyde and phenol–formaldehyde resol resins*, Journal of Thermo Analysis and Calorimetry, vol. 105, 349–356, 2011.

[37] U.S. Hong, S.L. Jung, K.H. Cho, M.H. Cho, S.J. Kim, H. Jang, *Wear mechanism of multiphase friction materials with different phenolic resin matrices*, Wear vol. 266, 739–744, 2009.

[38] J. Bijwe, N. Nidhi, B.K. Majumdar and B.K. Satapathy, *Influence of modified phenolic resins on the fade and recovery behavior of friction materials*, Wear vol. 259, 1068–1078, 2005.

[39] S.J. Kim, H. Jang, *Friction and wear of friction materials containing two different phenolic resins reinforced with aramid pulp*, Tribology International vol. 33, 477–484, 2000.

[40] J.H. Park, J. Chung, H.R. Kim, *Friction characteristics of brake pads with aramid fiber and acrylic fiber*, Industrial Lubrification and Tribology vol. 62, 91–98, 2010.

[41] M. Amirjan, *Microstructure, wear and friction behavior of nanocomposite materials with natural ingredients*, Tribology International, vol. 131,184–190, 2019.

[42] S. Venkatesh, K. Murugapoopathiraja, *Scoping Review of Brake Friction Material for Automotive*, Materials Today Proceedings vol. 16, 927–933, 2019.

[43] P. Cai, T. Wang, Q. Wang, *Effect of several solid lubricants on the mechanical and tribological properties of phenolic resin-based composites*, Polymer Composites vol. 36, 2203–2211, 2015.

[44] S.S. Kim, H.J. Hwang, M.W. Shin, H. Jang, *Friction and vibration of automotive brake pads containing different abrasive particles*, Wear vol. 271, 1194–1202, 2011.

[45] X. Xiao, Y. Yin, J. Bao, L. Lu, X. Feng, *Review on the friction and wear of brake materials*, Advances in Mechanical Engineering vol. 8, 1 –10, 2016.

[46] M. Eriksson, S. Jacobson, *Tribological surfaces of organic brake pads,* Tribology International vol. 33, 817–827, 2000.

[47] L. Barros, J. Poletto, P. Neis, N.F. Ferreira and C. Pereira, *Influence of copper on automotive brake performance*, Wear vol. 426-427, 741–749, 2019.

[48] M. Kumar, J. Bijwe, *Non-asbestos organic (NAO) friction composites: role of copper; its shape and amount*, Wear vol. 270, 269–280, 2011.

[49] P.C. Verma, L. Menapace, A. Bonfanti, R. Ciudin, S. Gialanella and G. Straffelini, *Braking pad-disc system: wear mechanisms and formation of wear fragments*, Wear vol. 322-323,1–8, 2015.

[50] U. Olofsson, Y. Lyu, A.H. Åström, J. Wahlström, S. Dizdar, A.P.G. Nogueira and S. Gialanella, *Laser Cladding Treatment for Refurbishing Disc Brake Rotors: Environmental and Tribological Analysis,* Tribology Letters vol. 69:57, 1–11, 2011.

[51] M. Gasser, M. Riediker, L. Mueller, A. Perrenoud, F. Blank, P. Gehr and B. Rothen-Rutishauser, *Toxic effects of brake wear particles on epithelial lung cells in vitro*, Particle and Fiber Toxicology vol. 6:30, 1–13, 2009.

[52] A.K. Lund, J. Lucero, S. Lucas, M.C. Madden, J.D. McDonald, J.-C. Seagrave, T.L. Knuckles, M.J. Campen, *Vehicular Emissions Induce Vascular MMP-9 Expression and Activity Associated With Endothelin-1–Mediated Pathways*, Arterioscler Thromb Vasc Biol. Vol. 29, 511–517, 2009.

[53] C. Barlow, L.I. Bendell, C. Duckham, D. Faugeroux and V. Koo, *Three-Dimensional Profiling Reveals Trace Metal Depositional Patterns in Sediments of Urban Aquatic Environments: A Case Study in Vancouver, British Columbia, Canada,* Water, Air, Soil Pollution vol. 225 2014.

[54] M. Leonardi, *Development of novel eco-friendly friction materials for disc brake systems,* doctoral thesis, 2020.

[55] C. Menapace, M. Leonardi, V. Matějka, S. Gialanella, and G. Straffelini, G, *Dry Sliding Behavior and Friction Layer in Copper-Free Barite Containing Friction Materials*, Wear vol. 398–399,191–200, 2018.

[56] M. Leonardi, M. Alemani, G. Straffelini and S. Gialanella, *A pin-on-disc study on the dry sliding behavior of a Cu-free friction material containing different types of natural graphite,* Wear vol. 442-443, 1–10, 2020.

[57] Y. Lyu, M. Leonardi, J. Wahlström, S. Gialanella and Ulf Olofsson, *Friction, wear and airborne particle emission from Cu-free brake materials,* Tribology International vol.141, 1–7, 2020.

[58] L.Y. Barros, J.C. Poletto, P.D. Neis, N.F. Ferreira, C.H.S. Pereira, *Influence of copper on automotive brake performance*, Wear vol. 426-427, 741–749, 2019.

[59] W. Österle, I. Dörfel, C. Prietzel, H. Roocha, A.-L. Cristol-Bulthé, G. Degallaix, Y. Desplanques, *A comprehensive microscopic study of third body formation at the interface*

between a brake pad and brake disc during the final stage of a pin-on-disc test, Wear 267, 781–788, 2009.

[60] A. Wirth, D. Eggleston, R. Withaker, *A fundamental tribochemical study of the third body layer formed during automotive friction braking*, Wear 179, 75–81, 1994.

[61] P. C. Verma, R. Ciudin, A. Bonfanti, P. Aswath, G. Straffelini and S. Gialanella, *Role of the friction layer in the high-temperature pin-on-disc study of a brake material,* Wear 346-347, 56–65, 2016.

[62] N.P. Suh and H.-C. Sin, *The Genesis of Friction*, Wear, 69, 91–114, 1981.

[63] E.R. Leheup and R.E. Pendlebury, *Unlubricated reciprocating wear of stainless steel with an interfacial air flow*, Wear 142, 351–372, 1991.

[64] A. Iwabuchi, K. Hori and H. Kubosawa, *The effect of oxides particles supplied at the interface before sliding on the server-mild wear transition*, Wear 128, 123–137, 1988.

[65] J. Jiang, F.H. Stott and M.M. Stack, *The role of triboparticulates in dry sliding wear,* Tribological International 31, issue 5, 245–256, 1998.

[66] M. Eriksson and S. Jacobson, *Tribological surfaces of organic brake pads,* Tribology International 33, 817–827, 2000.

[67] M. Alemani, S. Gialanella, G. Straffelini, R. Ciudin, U. Olofsson, G. Perricone, I. Metinoz, *Dry sliding of a low steel friction material against cast iron at different loads: characterization of the friction layer and wear debris*, Wear 376-377, 1450–1459, 2017.

[68] M.H. Cho, K.H. Cho, S.J. Kim, D.H. Kim and H. Janga, *The role of transfer layers on friction characteristics in the sliding interface between friction materials against gray iron brake disks,* Tribology Letters vol. 20, No. 2, 101–108, 2005.

[69] P. C. Verma, L. Menapace, A. Bonfanti, R. Ciudin, S. Gialanella, and G. Straffelini, *Braking pad-disc system: Wear mechanisms and formation of wear fragments*, Wear vol. 322-323, 251–258, 2015.

[70] J. Wahlström, *A study of airborne wear particles from automotive disc brakes*. PhD thesis, KTH Royal Institute of Technology, 2011.

[71] B. Venkataraman and G. Sundararajan, *Correlation between the characteristics of the mechanically mixed layer and wear behaviour of aluminum, Al-7075 alloy and Al-MMCs,* Wear 245, 22–38, 2000.

[72] G Straffelini and S Gialanella. Airborne particle matter from brake systems: An assessment for the relevant tribological formation mechanisms, Wear 478-479, 1–16, 2021.

[73] M. Leonardi, C. Menapace, V. Matějka, S. Gialanella, and G. Straffelini, *Pin-on-disc investigation on copper-free friction materials dry sliding against cast iron*, Tribology International vol. 119, 73–81, 2018.

[74] P.D. Neis, N.F. Ferreira, G. Fekete, L.T. Matozo, D. Masotti. *Towards a better understanding of the structures existing on the surface of brake pads*. Tribology International 105, 135–147, 2017.

[75] J. Park, B. Joo, H. Seo, W. Song, J.J. Lee, W. K. Lee, Ho Jang, *Analysis of wear induced particle emissions from brake pads during the worldwide harmonized light vehicles test procedure (WLTP*), Wear 466-467, 1–12, 2021.

[76] A. Cohen, et al. *Estimates and 25-year trends of the global burden of disease attributable to ambient air pollution: an analysis of data from the Global Burden of Diseases Study 2015*, The Lancet, vol. 389/10082,1907–1918, 2017.

[77] S.A. Awe, *Developing Material Requirements for Automotive Brake Disc,* Modern Concepts in Material Science, 1–4, 2019.

[78] N. Bukowiecki, R. Gehrig, P. Lienemann, M. Hill, R. Figi*, PM10 emission factors of abrasion particles from road traffic,* Swiss Fed. Dep. Environ. Transp. Energy Commun*.,* 1–23, 2009.

[79] F. Amato, *Quantifying Road dust resuspension in urban environment by Multilinear Engine: A comparison with PMF2*, Atmospheric Environment, vol 43/17, 2770-2780, 2009.

[80] R.M. Harrison, A.M. Jones, J. Gietl, J. Yin, D. C. Green, *Estimation of the contributions of brake dust, tire wear, and resuspension to non-exhaust traffic particles derived from atmospheric measurements*, Environmental science & technology, vol. 46, 6523–6529, 2012.

[81] P.G. Sanders, N. Xu, T.M. Dalka, M.M. Maricq, *Airborne brake wear debris: size distributions, composition, and a comparison of dynamometer and vehicle tests,* Environmental Science & Technology, vol. 37, 4060–4069, 2003.

[82] Air Quality Expert Group, *Non-Exhaust Emissions from Road Traffic,* 1-93, 2019.

[83] J.M. Samet, F. Dominici, F.C. Curriero, I. Coursac, S.L. Zeger, *Fine particulate air pollution and mortality in 20 US cities*, 1987–1994, New England Journal of Medicine, vol. 343,1742–1749, 2000.

[84] C.A. Pope III, R.T. Burnett, M.J. Thun, E.E. Calle, D. Krewski, K. Ito, G.D. Thurston, *Lung cancer, cardiopulmonary mortality, and long-term exposure to fine particulate air pollution*, Jama, vol. 287, no. 9,1132–1141, 2002.

[85] A. Helland, P. Wick, A. Koehler, K. Schmid, C. Som, *Reviewing the environmental and human health knowledge base of carbon nanotubes,* Environmental Health Perspectives, 115(8),1125–1131, 2007.

[86] M. Gasser, M. Riediker, L. Mueller, A. Perrenoud, F. Blank, P. Gehr, B. Rothen-Rutishauser, *Toxic effects of brake wear particles on epithelial lung cells in vitro.* Particle and Fiber Toxicology, 6:30, 2009.

[87] D. Vincent, *Airborne particulate matter and their health effects,* Encyclopédie de l'environnement, 1–11, 2019.

[88] G. Oberdörster, A. Maynard, K. Donaldson, V. Castranova, J. Fitzpatrick, K. Ausman, J. Carter, B. Karn, W. Kreyling, D. Lai, S. Olin, N. Monteiro-Riviere, D. Warheit, H. Yang. *Principles for characterizing the potential human health effects from exposure to nanomaterials: elements of a screening strategy.* Part. Fibre Toxicol. 2(8), 1–35, 2005.

[89] M. Riediker, R.B Devlin, T.R. Griggs, M.C. Herbst, P.A. Bromberg, R.W. Williams, W.E. Cascio, *Cardiovascular effects in patrol officers are associated with fine particulate matter from brake wear and engine emissions*. Particle and Fibre Toxicology, 1:2, 2004.

[90] B. Ostro, W. Feng, R. Broadwin, S. Green, M. Lipsett, *The Effects of Components of Fine Particulate Air Pollution on Mortality in California: Results from CALFINE,* Environ Health Perspect., 115(1): 13–19, 2007.

[91] LowBraSys Project. Available at http://www.lowbrasys.eu/en.

[92] M. Mosleh, P.J. Blau, D. Dumitrescu, *Characteristics and morphology of wear particles from laboratory testing of disk brake materials*, Wear 256, 1128–1134, 2004.

[93] J. Wahlström, L. Olander, U. Olofsson, *Size, shape, and elemental composition of airborne wear particles from disc brake materials*, Tribology Letters, vol. 38, 15–24, 2010.

[94] U. Olofsson, L. Olander, A. Jansson, *Towards a model for the number of airborne particles generated from a sliding contact*, Wear, vol. 267, 2252–256, 2009.

[95] O. Nosko, U. Olofsson, *Quantification of ultrafine airborne particulate matter generated by the wear of car brake materials,* Wear 374-375, 92–96, 2017.

[96] A. Iijima, K. Sato, K. Yano, H. Tago, M. Kato, H. Kimura, N. Furuta, *Particle size and composition distribution analysis of automotive brake abrasion dust for the evaluation of antimony sources of airborne particulate matter*, Atmos. Environ. 41, 4908–4919, 2007.

[97] J. Kukutschová, P. Moravec, V. Tomásek, V. Matějka, J. Smolík, J. Schwarz, J. Seidlerová, K. Safárová, P. Filip, *On airborne nano/micro-sized wear particles released from low-metallic automotive brakes*, Environ. Pollut. 159, 2011.

[98] J. Park, B. Joo, H. Seo, W. Song, J.J. Lee, W.K. Lee, H. Jong, *Analysis of Wear Induced Particle Emissions from Brake Pads during the Worldwide Harmonized Light Vehicles Test Procedure (WLTP),* Wear 466-467, 1–12, 2021.

[99] A. Liati, D. Schreiber, D. Lugovyy, S. Gramstat, P.D. Eggenschwiler, *Airborne particulate matter emissions from vehicle brakes in micro- and nano-scales: Morphology and chemistry by electron microscopy*, Atmospheric Envir. vol. 212, 281–289, 2019.

[100] O. Nosko, U. Olofsson, *Effective density of airborne wear particles from car brake materials*, Journal of Aerosol Science, vol. 107, 94–106, 2017.

[101] O. Nosko, R. Borraji-Pelaez, P. Hedström. U. Olofsson, *Porosity and shape of airborne wear microparticles generated by sliding contact between a low-metallic friction material and a cast iron*, Journal of Aerosol Science, vol. 113, 130–140, 2017.

[102] P. Peikertová, J. Kukutschová, I. Vávra, V. Matějka, O. Životský, M. Vaculík, P.W.Lee, P.Filip, *Water suspended nanosized particles released from nonairborne brake wear debris,* Atmospheric Envir. vol. 212, 281–289, 2019.

[103] S. Suzuki, R. Yamashima, H. Nakagawa, *Establishment of brake wear emission analysis techniques,* Dresden 21–23 May 2019 Proc. Eurobrake Fisita, 2019.

[104] C. Menapace, A. Mancini, M. Federici, G Straffelini, S. Gialanella, *Characterization of airborne wear debris produced by brake pads pressed against HVOF-coated discs,* Friction 8(2), 421–432, 2020.

[105] OECD, *Non-exhaust Particulate Emissions from Road Transport: An Ignored Environmental Policy Challenge*, OECD Publishing, Paris, 2020.

[106] A. Simons, Road transport: new life cycle inventories for fossil-fuelled passenger cars and non-exhaust emissions in ecoinvent v3, The Intern. Journal of Life Cycle Assessment, vol 21/9, 1299–1313, 2016.

[107] B.D. Garg, S.H. Cadle, P.A. Mulawa, P.J. Groblicki, C. Laroo, G.A. Parr, *Brake wear particulate matter emissions*, Environmental Science and Technology, vol. 34/21, 4463–4469, 2000.

[108] A. Luekewille, I. Bertok, M. Amann, J. Cofala, F. Gyarfas, C. Heyes, N. Karvosenoja, Z. Klimont, *A Framework to estimate the Potential Costs for the Control of Fine Particulate Emissions in Europe*, International Institute for Applied Systems Analysis, Interim Report IR-01-023, 1–119, 2001.

[109] M. Alemani, U. Olofsson, G. Perricone, A. Söderberg, J. Wahlström, A. Ciotti, A study on the load level influence on particulate matter emissions from the sliding contact between a low steel friction material and cast iron, Eurobrake 2015, Dresden, 2015.

[110] J. Wahlström, U. Olofsson, and L. Olander, A pin-on-disc study of automotive disc brake materials focusing on airborne wear particles, Journal of tribology vol. 46, 195–204, 2010.

[111] A. Mamakos, M. Arndt, D. Hesse, K. Augsburg, *Physical Characterization of Brake-Wear Particles in a PM10*, Atmosphere, vol. 639, 1–19, 2019.

[112] H.-G. Namgung, J.-B. Kim, S.-H. Woo, S. Park, M. Kim, M.-S. Kim, G.-N. Bae, D. Park, and S.-B. Kwon, *Generation of nanoparticles from friction between railway brake disks and pads*, Environmental Science & Technology, vol. 50, 3453–3461, 2016.

[113] U. Olofsson, L. Olander, A. Jansson, *A study of airborne wear particles generated from a sliding contact*, Journal of Tribology, vol. 131, 1–4, 2009.

[114] M. Alemani, J. Wahlström, and U. Olofsson, *On the influence of car brake system parameters on particulate matter emissions*, Wear, vol. 396-397, 67–74, 2018.

[115] S. Gramstat, T. Mertens, R. Waninger, D. Lugovyy, *Impacts on Brake Particle Emission Testing*, Atmosphere vol. 11, 1–16, 2020.

[116] G. Perricone, M. Alemani, I. Mutinöz, V. Matějka, J. Wahlström, U. Olofsson, *Towards the ranking of airborne particle emissions from car brakes – a system approach*, Proceedings of the Institution of Mechanical Engineers, Part D: Journal of Automobile Engineering, vol. 231/6, 781–797, 2016.

[117] V. Matějka, I. Mutinöz, J. Wahlström, M. Alemani, G. Perricone, *On the running-in of brake pads and discs for dyno bench tests,* Tribology International, vol. 115, 424–431, 2017.

[118] D. Hesse, C. Hamatschek, K. Augsburg, T. Weigelt, A. Prahst, S. Gramstat, *Testing of Alternative Disc Brakes and Friction Materials Regarding Brake Wear Particle Emissions and Temperature Behavior*, Atmosphere, vol. 436, 1–23, 2021.

[119] K.M. Omatola, A.D. Onojah. *Elemental analysis of rice husk ash using x-ray fluorescence technique.* International journal of physical sciences 4: 189–193, 2009.

[120] S. Sugita. *On the Economical Production of Large Quantities of Highly Reactive Rice Husk Ash*. International Symposium on Innovative World of Concrete, Rotterdan 371, 1993.

[121] B. I. Rasoul. *Effect of incineration temperatures to time on the rice husk ash (RHA) silica structure.* PhD thesis, 2018.

[122] A.C.P. Rodrigues, W. Österle, T. Gradt, C.R.F. Azevedo, *Impact of copper nanoparticles on tribofilm formation determined by pin-on-disc tests with powder supply: Addition of artificial third body consisting of Fe_3O_4, Cu and graphite,* Tribology International 110, 103–112, 2017.

[123] J. Wahlström, V. Matějka, Y. Lyu, A. Söderberg, *Contact Pressure and Sliding Velocity Maps of the Friction, Wear and Emission from a Low-Metallic/Cast-Iron Disc Brake Contact Pair*, Tribology in Industry 39, 460–470, 2017.

[124] L. Lutterotti, H. Pillière, C. Fontugne, P. Boullay, D. Chateigner. *Full-profile search–match by the Rietveld method*. Journal of Applied Crystallografic. 52: 587-598, 2019.

[125] A.P.G. Nogueira, P. Bagolan, M. Leonardi, S. Gialanella, G. Straffelini. *The role of scorching treatment on the wear and emission of friction materials with and without copper.* Wear 460-461: 203480, 2020.

[126] W. Osterlë, C. Prietzel, H. Kloß, A.I. Dmitriev, *On the role of copper in brake friction materials*, Tribology International 43 (12), 2317–2326, 2010.

[127] A.P.G. Nogueira, D. Carlevaris, C. Menapace, G. Straffelini. *Tribological and emission behavior of novel friction materials*. Atmosphere 11:1–16, 2020.

[128] ECOPADS project. Available at https://eitrawmaterials.eu/project/ecopads/.

[129] A.P. G. Nogueira, G.S. Gehlen, P.D. Neis, N.F. Ferreira, S. Gialanella, G. Straffelini, *Rice husk as a natural ingredient for brake friction material: A pin-on-disc investigation*, Wear 494-495, 1–10, 2022.

List of Publications

- **Tribological and emission behaviour of novel friction materials.** A.P.G. Nogueira, D. Carlevaris, C. Menapace and G. Straffelini. Atmosphere vol. 11, 1-16 – 2020.

- **The role of scorching treatment on the wear and emission behavior of friction materials with and without copper.** A.P.G. Nogueira, P. Bagolan, M. Leonardi, S. Gialanella and G. Straffelini. Wear vol. 460-461 – 2020.

- **Laser Cladding Treatment for Refurbishing Disc Brake Rotors: Environmental and Tribological Analysis.** U. Olofsson, Y. Lyu, A. Hedlund, J. Wahlström, S. Dizdar, A.P.G. Nogueira and S. Gialanella. Tribology Letters vol. 69, 1-11 – 2020.

- **Sliding Behavior and Particle Emissions of Cu- Free Friction Materials with Different Contents of Phenolic Resin.** A.P.G. Nogueira, M. Leonardi, G. Straffelini and S. Gialanella. Tribology Transactions vol. 63, 770-779 - 2020.

- **Friction, wear and particles emission during the bedding stage of a Cu-free friction material. S.** Candeo, A.P.G. Nogueira, M. Leonardi and G. Straffelini. Wear vol. 486–487, 1-12 – 2021.

- **Effect of nanostructure on phase transformations during heat treatment of 2024 aluminium alloy.** K.B. Demetrio, A.P.G. Nogueira, C. Menapace, T. Bendo and A. Molinari. Journal of Materials Research and Technology – 2021.

- **Rice husk as a natural ingredient for brake friction material: a Pin-on-Disc investigation.** A.P.G. Nogueira, G.S. Gehlen, P.D. Neis, N.F. Ferreira, S. Gialanella and G. Straffelini. Submitted to Wear vol. 494-495, 2022.

Participation to Congresses, Schools and Workshops

- **Investigation of the mechanism for generating brake emissions in Cu-full and Cu-free materials.**
  A.P.G. Nogueira, M. Leonardi and G. Straffelini. 15th SAE BRASIL International Colloquium of Brakes and Motion Control & Engineering Exhibition. 2021.

- **SEM and TEM Characterization of Particulate Matter from Disc-Brake Wear**.
  A. Sinha, A.P.G. Nogueira, G. Ischia and G. Gialanella. 8th International Biennial Conference on Ultrafine Grained and Nanostructured Materials. 2021.

- **Investigation of tribological behavior and airborne emissions during the bedding stage**.
  A.P.G. Nogueira, S. Candeo, M. Leonardi and G. Straffelini. Eurobrake 2021. 2021.

- **Collecting and characterization of ultrafine particles from brake emissions.**
  A.P.G. Nogueira and S. Gialanella. UFGNSM Conference, 2019.